



UNIVERSITÄT ROSTOCK

# High-pressure equations of state and phase diagrams of molecular H-C-N-O compounds

Kumulative Dissertation  
zur Erlangung des akademischen Grades  
doctor rerum naturalium (Dr. rer. nat.)  
der Mathematisch-Naturwissenschaftlichen Fakultät  
der Universität Rostock

vorgelegt von  
**Mandy Bethkenhagen,**  
geboren am 28.09.1986 in Rostock

Rostock, 28.10.2016

## **Gutachter**

Prof. Dr. Ronald Redmer  
Institut für Physik, Universität Rostock

Dr. Andreas Hermann  
School of Physics and Astronomy, The University of Edinburgh

Einreichung: 28. Oktober 2016  
Verteidigung: 20. Januar 2017

Adresse: Universität Rostock  
Institut für Physik  
18051 Rostock  
Tel: +49 381 498-6916  
Fax: +49 381 498-6912  
Internet: <http://www.physik.uni-rostock.de>

E-Mail des Autors: [mandy.bethkenhagen@uni-rostock.de](mailto:mandy.bethkenhagen@uni-rostock.de)



---

## Abstract

The thermodynamic description of molecular systems composed of water ( $\text{H}_2\text{O}$ ), ammonia ( $\text{NH}_3$ ), and methane ( $\text{CH}_4$ ) at high pressure is the subject of the present cumulative thesis. The focus lies on the calculation of equations of state, phase diagrams, and their characterization by employing the quantum-statistical method density functional theory molecular dynamics (DFT-MD).

Complementary to the extensive high-pressure water data existing in literature, we first investigate the thermodynamic properties of ammonia and methane. The resulting equations of state are verified by comparing them to experimental Hugoniot curves. From the simulations of methane, we obtain strong signs of demixing into diamond and hydrogen. Moreover, the properties of the binary and ternary mixtures of the three molecules are investigated. In particular superionic water-ammonia mixtures are proposed for the first time using evolutionary structure searching. Additionally, the linear mixing approximation for ammonia, methane, and water is validated and the diffusive properties of different mixtures are discussed. The obtained simulation results serve as input for modeling the interior structure of giant planets. Especially the pressure-temperature range up to 1 TPa and 20000 K is investigated. These conditions are relevant for Uranus, which is prototypical for the huge class of ice-rich exoplanets.

---

## Kurze Zusammenfassung

Die thermodynamische Beschreibung komplexer Gemische bestehend aus Wasser ( $\text{H}_2\text{O}$ ), Ammoniak ( $\text{NH}_3$ ) und Methan ( $\text{CH}_4$ ) unter hohem Druck ist Gegenstand der vorliegenden kumulativen Dissertation. Dabei liegt der Fokus auf der Berechnung von Zustandsgleichungen, Phasendiagrammen und deren Charakterisierung mittels der quantenstatistischen Methode der Dichtefunktionaltheorie-Molekulardynamik (DFT-MD).

Ergänzend zu den bereits umfangreich in der Literatur vorhandenen Hochdruck-Wasserdaten, werden zunächst die thermodynamischen Eigenschaften von Ammoniak und Methan untersucht und die resultierenden Zustandsgleichungen mit experimentellen Hugoniot-Kurven verifiziert. Dabei ergeben die Simulationen für Methan erste starke Hinweise auf die seit langem diskutierte Entmischung in Diamant und Wasserstoff. Weiterhin werden die Eigenschaften der binären und ausgesuchter ternärer Mischungen der drei Moleküle untersucht. Insbesondere finden wir erstmals superionische Wasser-Ammoniak-Gemische, die mit Hilfe von evolutionary structure searching vorhergesagt werden. Darüber hinaus wird die Näherung der linearen Mischung für Ammoniak, Methan und Wasser validiert und die Diffusionseigenschaften verschiedener Mischungen diskutiert. Die erhaltenen Simulationsergebnisse dienen als Eingabeparameter für die Modellierung des inneren Aufbaus großer Planeten. Dabei wurde insbesondere der für Uranus relevante Druck-Temperatur-Bereich bis 1 TPa und 20000 K untersucht, da dieser Planet prototypisch für die große Klasse von eisreichen Exoplaneten ist.

# Contents

<b>1. Introduction</b>	<b>1</b>
1.1. Phase diagrams . . . . .	2
1.1.1. Water, ammonia, and methane . . . . .	2
1.1.2. Binary and ternary mixtures . . . . .	5
1.2. Molecular compounds in our Solar System and beyond . . . . .	6
1.2.1. Interior structure models of giant planets . . . . .	6
1.2.2. Equations of state (EOS) as input for planetary modeling . . . . .	8
1.3. Aim and outline of this thesis . . . . .	9
<b>2. Density functional theory molecular dynamics (DFT-MD)</b>	<b>11</b>
2.1. Born-Oppenheimer approximation . . . . .	12
2.2. Density functional theory (DFT) . . . . .	12
2.2.1. Kohn-Sham formalism for finite temperatures . . . . .	13
2.2.2. Approximations for the exchange-correlation functional . . . . .	15
2.3. Molecular dynamics (MD) . . . . .	16
2.4. DFT-MD simulations with VASP . . . . .	17
<b>3. Computational methods and simulation details</b>	<b>19</b>
3.1. Equations of state (EOS) and Hugoniot curve . . . . .	19
3.2. Structural and transport properties . . . . .	21
3.2.1. Pair distribution functions . . . . .	21
3.2.2. Bonding autocorrelation functions (BACF) . . . . .	21
3.2.3. Diffusion coefficients and mean square displacements . . . . .	22
3.3. Crystal Structure Prediction (CSP) . . . . .	22
3.3.1. Evolutionary structure search with XtalOpt . . . . .	23
3.3.2. Quasi-harmonic approximation employing Phonopy . . . . .	24
<b>4. Outline of the obtained results</b>	<b>27</b>
4.1. Ammonia . . . . .	27
4.2. Methane . . . . .	29
4.3. Binary mixtures . . . . .	32
4.4. Ternary mixtures . . . . .	35
4.5. Implications for the interior structure of Uranus . . . . .	36
4.6. Summary and outlook . . . . .	38
<b>5. Publications</b>	<b>41</b>
5.1. Equation of state and phase diagram of ammonia at high pressures from ab initio simulations . . . . .	42

5.2. Superionic phases of the 1:1 water-ammonia mixture . . . . .	43
5.3. Bonding and structure in dense multi-component molecular mixtures . .	44
5.4. Uranus evolution models with simple thermal boundary layers . . . . .	45
5.5. The linear mixing approximation for ices and its application to Uranus .	46
<b>A. Equations of state for binary mixtures</b>	<b>I</b>
<b>Bibliography</b>	<b>III</b>
<b>Curriculum vitae</b>	<b>XIX</b>
<b>Danksagung/Acknowledgement</b>	<b>XXIII</b>

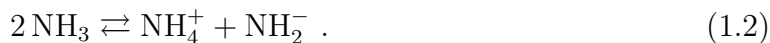
# 1. Introduction

In 2014, the spacecraft Rosetta arrived at the comet 67P/Churyumov-Gerasimenko, and many people witnessed the landing of Philae, the first man-made object to land on a comet. Since then, Rosetta has collected many valuable data, including the finding of the simplest amino acid, glycine, accompanied by methylamine and ethylamine in the coma of the comet [1]. It is organic compounds like these that provide the basis of life as we know it. Major building blocks of proteins and deoxyribonucleic acid (DNA), the carrier of genetic information, are amino acids and nitrogenous bases [2]. The rings and chains, which are assembled to these large biological compounds, are built up by the elements hydrogen (H), carbon (C), nitrogen (N), and oxygen (O). These elements are counted among the seven most abundant ones in our Solar System, which is significantly enriched in heavy elements compared to the composition of the Milky Way [3]. Our Sun is orbited by four inner rocky planets as well as four outer giant planets accompanied by several smaller bodies. They comprise hitherto 178 planetary satellites, five dwarf planets, and numerous asteroids [4]. Many of those objects contain remarkable amounts of the so-called planetary ices [5; 6], i.e., methane ( $\text{CH}_4$ ), ammonia ( $\text{NH}_3$ ), and water ( $\text{H}_2\text{O}$ ), which are, along with their mixtures, the linchpin of this work.

In everyday life we encounter these molecules in a variety of forms. Water is essential for all known forms of life and as such makes up between 50% and 75% of the human body, depending on the individual [7]. It covers 70% of Earth's surface, with its greatest portion to be found as liquid in the oceans. Moreover, large amounts of water are stored in polar ice and in the atmosphere. Water vapour is one of the most important greenhouse gases, which originates primarily from natural sources. The anthropogenous greenhouse effect is fueled by carbon dioxide and methane, which are predominantly released from industrial processes and livestock farming [8]. Apart from its presence in Earth's atmosphere, methane represents the main component of natural gas, which makes it an important energy source. The third molecule, ammonia, is utilized as a refrigerant, and is the most important precursor for fertilizers, which are typically ammonium salts [9].

Chemically, water, ammonia, and methane are isoelectronic molecules and many properties are determined by the number of lone electron pairs as well as the arrangement of the atoms within each molecule leading to a slight, however significant, difference in bond angle. For example, in the methane molecule the four hydrogen atoms are arranged at the edges of a perfect tetrahedron surrounding the carbon atom with a HCH bond angle of  $109.5^\circ$ . Hence, all charges are balanced and the resulting methane molecule is non-polar. The HNH angle amounts to  $107.3^\circ$  and the HOH angle to  $104.5^\circ$  and both molecules possess unbound electrons. Therefore, water and ammonia have strong dipole moments of 1.85 D and 1.47 D [10], respectively. This becomes evident as they show

autoprotolysis:



The charge in water as well as ammonia is transported by proton hopping, which is described as Grotthuss mechanism [11]. Due to this similar behavior, water and ammonia mix very well. Since the polar nature of the water molecule is very different from methane, any water-methane mixture is governed by hydrophobic hydration. Much attention has been drawn to methane clathrate structures, composed of water cages hosting methane as guest molecules inside [12–14]. They are to a great extent stabilized by van-der-Waals forces. These clathrates are very abundant at the bottom of the oceans as they form solely under pressure and methane is released as soon as the clathrates are brought to atmospheric pressures.

As the pressure is increased, new and potentially important effects such as stoichiometries unlike those we are familiar with at ambient conditions can be found [15–17]. Research in this area was boosted when first experiments were designed that were capable of reaching those high-pressure conditions. Their foundation was laid in the early 20th century by Bridgman [18], who designed a giant press, which allowed the compression of samples up to 10 GPa. With this technique, which he was awarded the Nobel Prize for in 1946, he pioneered in investigating the high-pressure phase diagram of water [19]. The apparatus worked on the same principles as modern diamond anvil cells (DACs) [20] and today, pressures up to 1 TPa can be achieved using a double-stage DAC [21]. Laser heating of DACs allows the study of the warm dense matter regime, which comprises strongly-correlated matter in the eV range with densities typical for condensed matter. This corresponds to the conditions suspected in the interior of giant planets. In this thesis we aim at investigating warm dense H-C-N-O compounds, which are relevant for planetary modeling, using DFT-MD simulations.

### 1.1. Phase diagrams

In this section, the phase diagrams of water, ammonia, and methane are introduced based on the available data in literature with special emphasis on the thermodynamic conditions covered by experiments. The number of compounds which can be formed by mixing these three molecules is tremendous. Therefore, we restrict this discussion to the phase diagrams of exemplary binary and ternary mixtures of relevance to the planetary objects considered in this work. The hydrogen concentration in these mixtures is chosen according to the stoichiometry of water, ammonia, and methane. Discussions on mixtures with increased hydrogen content such as  $\text{H}_2\text{O}-\text{H}_2$  and  $\text{CH}_4-\text{H}_2$  can be found elsewhere [22–24].

#### 1.1.1. Water, ammonia, and methane

The phase diagrams of water [25–27], ammonia [28–34], and methane [35–37] are illustrated in Fig. 1.1. The shown temperature-pressure conditions range up to 1000 K and

cover between  $10^{-6}$  GPa and  $10^2$  GPa corresponding to the thermodynamic conditions that can be achieved routinely in laboratory experiments using x-ray diffraction, Raman scattering and neutron diffraction.

By comparing the phase diagrams, it becomes evident that the melting line as well as the critical point decrease significantly in temperature with decreasing molecular mass. Water starts to melt from the hexagonal ice Ih at standard conditions (273.15 K, 1 bar =  $10^{-4}$  GPa). Upon melting, the density increases and reaches a maximum at 277 K [38], which is one of the well-characterized anomalies of water. Apart from the liquid and gaseous phase, the phase diagram shown in Fig. 1.1a contains a variety of solid phases. Currently, there are at least 15 known crystalline ice phases [14], three amorphous ice phases [39] and several high-pressure results from crystal structure prediction [40–43] discussed in literature. Interestingly, all crystalline phases adjoining the melting line, i.e., ice Ih, III, V, VI and VII, are characterized by disordered hydrogen bonds. At the same time, the low-temperature ice phases possess ordered hydrogen bonds [14; 44]. Additionally, some ice phases are metastable and can be solely obtained by following specific experimental pathways. For example, ice IV and XII are produced via isobaric heating of high-density amorphous (HDA) ice [45].

At even higher pressures and temperatures than considered in this figure, water is predicted to be present in the superionic phase. This phase is characterized by a lattice of oxygen ions with mobile hydrogen ions. This exotic state was described in various studies [46–49]; some of them even discuss multiple superionic water phases [50–52]. A recent theoretical study predicted a novel superionic-superionic phase transition within the superionic bcc phase [53].

Fig. 1.1b shows the phase diagram of ammonia as determined by experiments. It contains five solid phases [32; 54], where I is cubic, while II and III are rotationally disordered hcp and fcc phases, respectively. The phases IV and V have an orthorhombic lattice. Crystal structure prediction studies discuss further lattice symmetries [55–57], especially with ionic  $\text{NH}_4^+/\text{NH}_2^-$  configurations. This is also supported by experimental data by Palasyuk *et al.* [58]. Moreover, a superionic phase (denoted by SI) is shown in Fig. 1.1b, which has either an fcc or a pseudo-hcp lattice according to the experiments and simulations by Ninet *et al.* [33]. Although this experiment finds strong indications of the superionic phase, it should be noted that there is still no conclusive direct measurement of the superionic phase, neither for ammonia nor water, up to now. Further stoichiometries of other NH compounds at high pressures are discussed by Goncharov *et al.* [59].

At standard conditions, methane is found as a colorless gas similar to ammonia. However, its phase diagram exhibits considerable differences compared to those of water and ammonia as it does not contain a superionic phase and it is by far less structurally characterized. There are at least nine discussed solid phases for methane [35; 60; 61] at low temperatures as shown in Fig. 1.1c including again a rotationally disordered fcc phase, which is denoted by phase I. The phases III and IV have a tetragonal unit cell, while phases V and VI exhibit an hcp structure. Methane A and B have a more complex structure and are still heavily debated. Phase A is found above 5.4 GPa at room temperature and it can be understood as a strongly distorted version of the close packed phase I. [61], while phase B remains not completely resolved [37]. HP denotes three high pressure phases, which possess a cubic unit cell [60; 62].

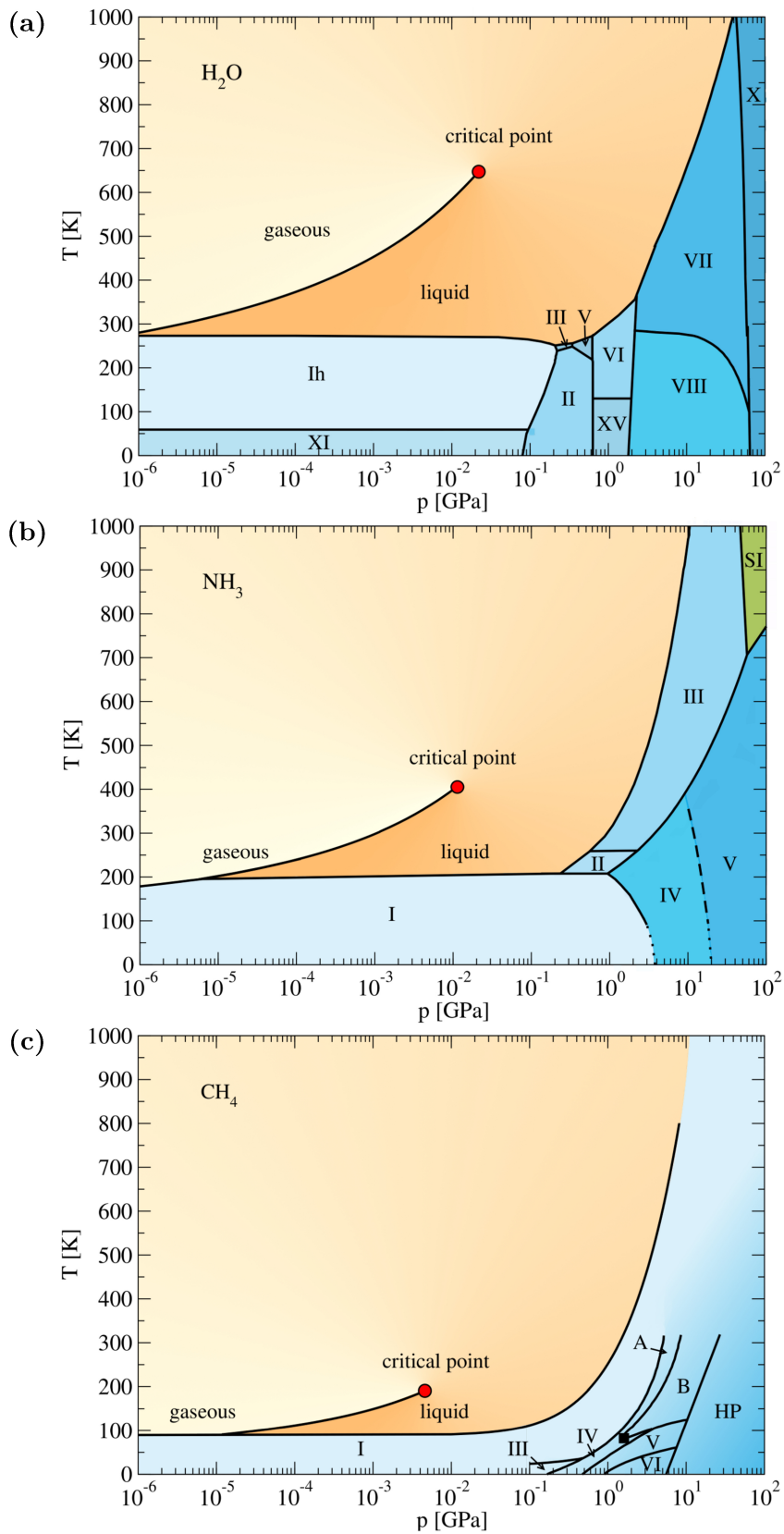
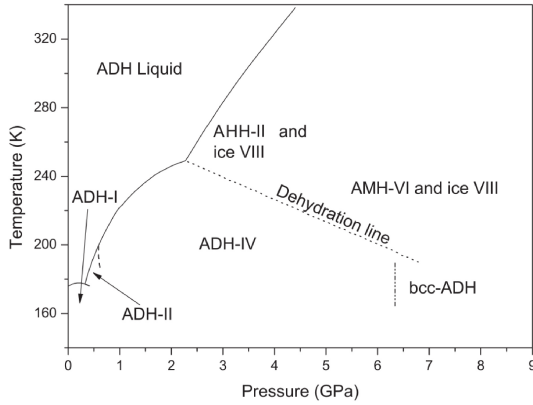


**Fig. 1.1.:** Phase diagrams of water [25–27] (a), ammonia [28–34] (b), and methane [35–37] (c) based on the available experimental data (see text for details).

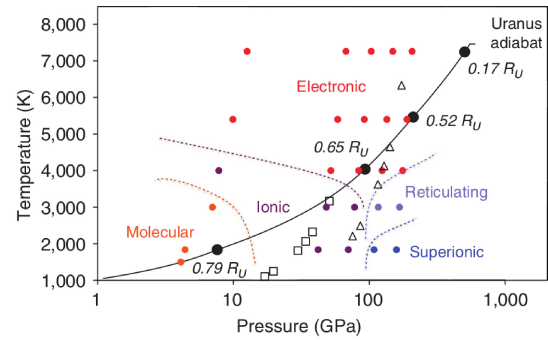


### 1.1.2. Binary and ternary mixtures

The phase diagrams of the binary mixtures are best characterized for small pressures ranging up to 10 GPa. For example, the methane clathrates discussed in the introductory section are known to have three different structures at ambient pressures, whereas there are several more discussed at higher pressures [13; 63; 64]. In this section we want to emphasize the binary water-ammonia mixture, whose high-pressure properties are studied in this work. Water and ammonia do not form such clathrate structures, since both molecules are characterized by strong dipole moments. Water-ammonia mixtures are known to favor one out of three compositions: 1:1 ammonia monohydrate (AMH), 1:2 ammonia dihydrate (ADH), 2:1 ammonia hemihydrate (AHH) [65]. For each composition various solid phases exist, which have been investigated experimentally [14] as well as by random structure searching [66; 67]. An exemplary phase diagram is shown in Fig. 1.2a,



(a) ammonia hydrates



(b) synthetic Uranus

**Fig. 1.2.:** Phase diagrams of ammonia hydrate [65] (a) and a ternary mixture (b), which consists of water, ammonia as well as isopropanol. The latter is characterized by a H-C-N-O composition of 28:4:1:7 and is usually referred to as “synthetic Uranus” [68].

which illustrates the dehydration of the observed water-ammonia structures. As the pressure increases, structures bearing less water are favored ranging from ADH over AMH to AHH.

To our knowledge, all published phase diagrams for the hydrates of ammonia and methane are limited to ambient temperatures. Solely for the ternary mixture a phase diagram exists which covers the warm dense matter region [68]. It is shown in Fig. 1.2b and was derived from a joint effort of DFT-MD simulations and shock compression experiments. Apart from an ordinary molecular phase and an ionic phase, they find a reticulating phase characterized by a carbon network as well as a conducting electronic fluid phase. Furthermore, that study suggests that even the ternary mixture may adopt a superionic phase.

## 1.2. Molecular compounds in our Solar System and beyond

Every terrestrial neighbor of Earth shows evidence of hosting water, at least for some time in their history [44]. Today, there is no water left on Mercury [69] and Venus [70], whereas solid water is still detected at the south pole cap of Mars [71]. Recently, the NASA missions Dawn and New Horizons, exploring the asteroid belt and trans-Neptunian objects, respectively, reported signs of (sub-)surface water on the dwarf-planets Ceres [72] and Pluto [73].

The most considerable portion of the planetary ices are supposed to reside in the interior of the giant planets Jupiter, Saturn, Uranus, and Neptune [5]. The latter two have mean densities of  $1.3 \text{ g/cm}^3$  and  $1.6 \text{ g/cm}^3$  similar to slightly compressed water, indicating they are mainly composed of planetary ices. Furthermore, their atmospheres are significantly enriched in carbon ( $\text{C/H} \sim 80\text{x solar}$ ) suggesting a large fraction of methane. Indeed, their bluish color results from methane absorption in their atmospheres. On the other hand, Jupiter and Saturn are predominately built up by hydrogen and helium. Hence, Jupiter and Saturn are often referred to as gas giant planets, while Uranus and Neptune are classified as ice giant planets.

Moreover, the moons of the giant planets attract a lot of attention, since they contain water, ammonia, and methane as well and exhibit some remarkable features, e.g., sub-surface water and water-ammonia oceans [74]. Among them are the Galilean satellites Europa, Callisto, and Ganymede, which will be investigated by ESA's future mission JUICE (JUper ICy moon Explorer) [75]. The spacecraft is scheduled to launch in 2022 and one of its goals is to measure the thickness of Europa's water ocean. Moreover, Titan and Enceladus orbiting Saturn are discussed to host ammonia hydrates and methane clathrates, which initiated a strong interest in those mixtures for pressures up to 10 GPa [14; 76].

Beyond our Solar System, a vast number of further planetary systems exist as detected by, for instance, the Kepler and CoRoT missions. Lots of these objects are believed to contain water, e.g., GJ 436b, Kepler-22b, Kepler-452b, and GJ 1214b. Those types of planets are especially sought after, since there might be a connection between water oceans and habitability of exoplanets [77]. Thereby, two classes are of great interest, i.e., Neptune-like and Earth-like planets [78]. In particular the exoplanets are discussed with respect to the phase diagram of water [79; 80] and their resulting magnetic field properties [81]. However, for most exoplanets very few properties are measured. Therefore, the basis for understanding those exoplanets is the modeling of our better constrained Solar System planets.

### 1.2.1. Interior structure models of giant planets

Standard planetary interior models are usually constructed from two convective, adiabatic layers, representing outer and inner mantle, as well as an isothermal planetary core. In an iterative scheme each layer is varied until all available observational constraints, such as effective temperature, mean composition, luminosity, and the gravitational mo-

ments, are reproduced by the model. The evolution from formation of the planet to present day can be calculated for such a model, where it is required to yield the age of the Solar System of roughly 4.6 billion years. Details on the procedure of constructing planetary models can be found in literature along with an overview on the results for the giant planets [6; 82–84].

In general, Jupiter can be very well described by applying the standard modeling procedure described above [85]. Furthermore, the planet’s magnetic field as well as the observed zonal flows can be very well recovered from dynamo simulations [86]. Although Saturn is very similar to Jupiter, the planet’s interior structure model requires additional processes such as inhomogeneous evolution due to hydrogen-helium demixing [87] to yield the observed luminosity [88; 89]. Moreover, dynamo models have difficulties in explaining the strong dipolarity of Saturn’s magnetic field and its alignment with the axis of rotation [90].

Uranus and Neptune appear even more puzzling. In Fig. 1.3 a prototypical model for an ice giant planet is shown to illustrate the general questions raised when Uranus and Neptune are discussed. While Neptune’s interior structure can be adequately modeled us-

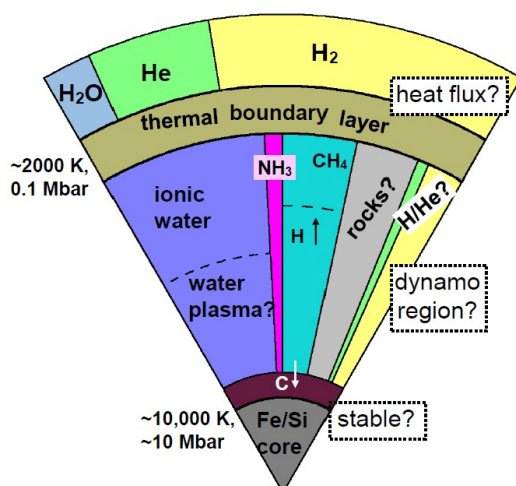


**Fig. 1.3.:** Sophisticated interior structure model of a prototypical ice giant planet summarizing the materials and uncertainties discussed in literature (courtesy of Nettelmann). Besides the three ordinary layers, a thermal boundary layer in between outer and inner mantle as well as a carbon layer on top of the core are suggested to be present in Uranus’ interior.

ing the standard approach, the equivalent Uranus model fails to reproduce the planet’s remarkably low luminosity [91]. Furthermore, their non-axisymmetrical, highly non-dipolar magnetic fields are strongly debated with respect to the interior structure of the planets [92–94]. Especially the superionic phases, which are predicted to occur in water and ammonia [46], are of great interest in this context, since they might result in a stably stratified layer inside the planetary mantle region. Additionally, the demixing of methane into hydrogen and diamond [95] is discussed with respect to the size of the planetary cores, which the models usually find to be very small. Hence, the physical and chemical properties of matter within this ice layer are of great interest and accurate high-pressure equations of state are necessary to describe the planetary interiors properly.

### 1.2.2. Equations of state (EOS) as input for planetary modeling

The equations of state are a crucial input for planetary models that usually consist of different materials, whose abundance may even vary with depth. Therefore, the linear mixing approximation is applied, which assumes that the volume of a mixture at constant pressure  $p$  and temperature  $T$  is sufficiently described by adding up the volumes of the individual  $N_c$  components [96; 97]. The density  $\varrho$  and internal energy  $U$  of the mixture are obtained from the following relations [84]:

$$\frac{1}{\varrho(p, T)} = \sum_{i=1}^{N_c} \frac{x_i}{\varrho_i(p, T)} , \quad (1.3)$$

$$U(p, T) = \sum_{i=1}^{N_c} x_i U_i(p, T) . \quad (1.4)$$

The mass fraction  $x_i$  in the above equations is defined as the ratio of the mass of the  $i$ th component,  $m_i$ , and the total mass  $M$ :

$$x_i = \frac{m_i}{M} . \quad (1.5)$$

One is left with the choice of appropriate EOS for the individual materials that cover the required pressure and temperature conditions, which are illustrated in Fig. 1.4 for the solar giant planets [85; 88; 94] and Titan as representative for ice-bearing moons [74].

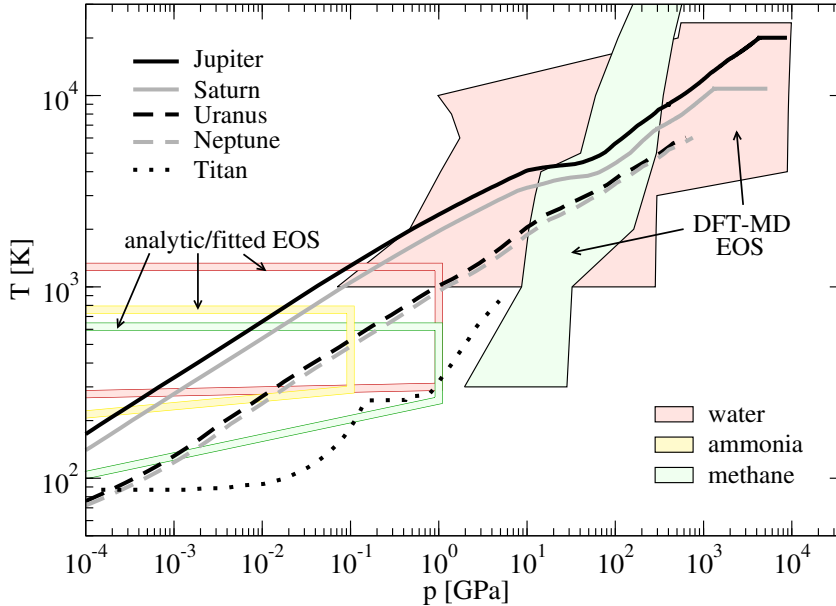


**Fig. 1.4.:** Planetary profiles for the ice-bearing objects Jupiter [85], Saturn [88], Uranus [94], Neptune [94] and Saturn’s moon Titan [74] along with a representative selection of EOS available in literature prior to this work. Very extensive analytic/fitted EOS, indicated by colored frames, exist for water (rose) [98], methane (light green) [99] and ammonia (yellow) [100], while DFT-MD data were only available for water (rose shaded area) [47] and methane (light green shaded area) [101].

For the entire range shown, several equations of state for hydrogen and helium are available such as the EOS by Saumon, Chabrier, and van Horn [102] as well as the Rostock EOS (REOS) combining DFT-MD data with chemical models [103]. However, the existing data are much sparser for the planetary ices. Fig. 1.4 illustrates the EOS data for those materials that have been available prior to this work. At pressures below 1 GPa, equations of state exist for water [98], ammonia [100; 104; 105], and methane [99]. They are referred to as analytic/fitted EOS, since they were constructed using experimental data and typically provide a thermodynamic potential.

For high-pressure water a DFT-MD EOS [47] exists, which compares much better to experiments [106] compared to other available EOS data such as the SESAME table (7150) [107]. Note, all SESAME EOS are based on a combination of several analytic methods and experimental data [108]. Combining either of both high-pressure EOS with the analytic/fitted EOS [98], yields an EOS which covers entirely the conditions predicted for all solar giant planets. Prior to this work, the available methane DFT-MD data [101] as well as the respective SESAME tables (5500, 5501, and 5502) [108] did not cover the entire required temperature-pressure range. For ammonia, no EOS at high pressures existed at all, for instance, the SESAME table (5520) [108] is limited up to 760 K and 1 GPa. For mixtures several low-pressure EOS [109; 110] exist, but there are almost no high-pressure data [14].

### 1.3. Aim and outline of this thesis

The present thesis is concerned with the understanding of molecular H-C-N-O compounds under warm dense matter conditions typical for the interior of giant planets as discussed in this introductory chapter. The focus will be set onto three main aspects, starting with the characterization of the phase diagrams of the pure molecular compounds ammonia and methane. In particular, the superionic phase of ammonia as well as the demixing of methane into hydrogen and diamond are of great interest here. The second goal is to answer the question whether superionic mixtures exist, which is studied exemplary for the 1:1 water-ammonia mixture. Finally, the main goal is to provide reliable EOS as input for planetary applications. Compositional effects are investigated and the validity of the linear mixing approximation is checked.

The following chapter 2 introduces the theoretical concept of density functional theory molecular dynamics (DFT-MD) simulations, which are the methodical foundation of this thesis. Starting from the quantum many-particle problem, which is tackled by treating the electrons and atomic nuclei separately, the basic ideas of DFT and MD are discussed. Building on this framework, the technical details of the plane-wave code VASP, i.e., the DFT-MD implementation used in this work, are presented.

Subsequently, additional computational methods including essential technical details of data analysis are discussed in chapter 3. In particular, details on the evaluation of the obtained DFT-MD data are given. This comprises the construction of equations of state and phase diagrams including the calculation of structural properties such as pair distribution functions, bonding autocorrelation functions and diffusion coefficients. Furthermore, crystal structure prediction (CSP) is introduced with special emphasis on evolutionary

structure searching. In this work we use the code XtalOpt, which is employed at 0 K to construct decent structures as input for the finite-temperature calculations.

In chapter 4 the main results of this work are outlined, which are contained in the publications in chapter 5. Note, that the discussion of the methane results is extensive, since these results are not entirely covered in the papers.

In addition, supporting information is given in appendix A, including a full set of EOS data for the binary 1:1 mixtures.

## 2. Density functional theory molecular dynamics (DFT-MD)

The main task in quantum physics and chemistry is to solve the Schrödinger equation,

$$i\hbar \frac{\partial}{\partial t} \Psi(\{\mathbf{q}_k, \sigma_k\}; t) = \hat{H} \Psi(\{\mathbf{q}_k, \sigma_k\}; t) , \quad (2.1)$$

describing the time evolution of the  $N$ -particle state for any non-relativistic many-particle system. The state is characterized by the wave function  $\Psi$ , which is a high-dimensional object, since it depends on the spin  $\sigma_k$  and the three dimensional space information  $\mathbf{q}_k$  of each particle  $k$  for all points in time  $t$ . The reduced Planck constant is represented by  $\hbar$ . As we consider no additional external fields, the Hamiltonian  $\hat{H}$  can be generally expressed as

$$\hat{H} = \hat{T}_e + \hat{T}_n + \hat{V}_{ee} + \hat{V}_{en} + \hat{V}_{nn} , \quad (2.2)$$

where  $\hat{T}_e$  and  $\hat{T}_n$  are the kinetic energy operators for the electrons and nuclei, respectively. The operators  $\hat{V}_{ee}$ ,  $\hat{V}_{en}$  and  $\hat{V}_{nn}$  account for the electron-electron, electron-nuclei and nuclei-nuclei interactions. Given a system's Hamiltonian  $\hat{H}$ , eq. (2.1) can be applied to an isolated atom as well as to complex many-particle systems such as molecules, surfaces and crystals. Here, we want to investigate a system containing  $N_n$  atomic nuclei and  $N_e$  electrons governed by each particle's kinetic and interaction energy via the Coulomb potential:

$$\begin{aligned} \hat{H} = & \sum_{i=1}^{N_e} \frac{\hat{\mathbf{p}}_i^2}{2m_e} + \sum_{a=1}^{N_n} \frac{\hat{\mathbf{P}}_a^2}{2M_a} \\ & + \sum_{i=1}^{N_e} \sum_{j>i}^{N_e} \frac{e^2}{4\pi\epsilon_0|\hat{\mathbf{r}}_i - \hat{\mathbf{r}}_j|} + \sum_{a=1}^{N_n} \sum_{b>a}^{N_n} \frac{Z_a Z_b e^2}{4\pi\epsilon_0|\hat{\mathbf{R}}_a - \hat{\mathbf{R}}_b|} - \sum_{i=1}^{N_e} \sum_{a=1}^{N_n} \frac{Z_a e^2}{4\pi\epsilon_0|\hat{\mathbf{r}}_i - \hat{\mathbf{R}}_a|} . \end{aligned} \quad (2.3)$$

In this formulation, each electron, carrying the elementary charge  $e$  and mass  $m_e$ , is represented by the operators for momentum  $\hat{\mathbf{p}}_i$  and position  $\hat{\mathbf{r}}_i$ . In the same way momentum  $\hat{\mathbf{P}}_a$  and position  $\hat{\mathbf{R}}_a$  are defined for a nucleus with mass  $M_a$  and charge number  $Z_a$ . In the following all operators will be expressed in position representation. Finally,  $\epsilon_0$  is the vacuum permittivity.

The above equations fully determine the evolution of the many-particle system, but analytic solutions without any approximations are limited to very few cases such as the hydrogen atom. Moreover, any numerical implementation suffers from the long-range character of the Coulomb interaction and the high dimensionality of the wave function, making it impossible to even store this object. Therefore, many flavors of approximations

and simulation techniques have been developed throughout the last decades. One particularly successful and effective simulation method is density functional theory (DFT) coupled with molecular dynamics (MD) which was suggested by Car and Parrinello [111] for the first time. The DFT-MD approach applied herein, which is similar to the Car-Parrinello MD, is described in the following.

## 2.1. Born-Oppenheimer approximation

As a first step to facilitate the many-particle problem, the electronic system is decoupled from the nuclei via the Born-Oppenheimer approximation [112]. It is based on the assumption that both particle species move on different time scales due to their substantial mass difference. The light electrons follow instantaneously any displacement of the much heavier nuclei. Hence, the total wave function of an adiabatic state  $m$  can be rewritten as product of the electronic  $\Phi_m$  and the nuclear wave function  $\chi_m$ :

$$\Psi(\{\mathbf{q}_k, \sigma_k\}; t) = \Psi(\{\mathbf{r}_i, \{\mathbf{R}_a\}\}; t) = \chi_m(\{\mathbf{R}_a\}; t) \Phi_m(\{\mathbf{R}_a\}, \{\mathbf{r}_i\}) . \quad (2.4)$$

The spin is neglected in this notation, since this work solely considers spin-degenerate states. Inserting the above expression into eq. (2.1) we obtain a reduced stationary Schrödinger equation for the electrons,

$$(\hat{T}_e + \hat{V}_{ee} + \hat{V}_{en})\Phi_m(\{\mathbf{R}_a\}, \{\mathbf{r}_i\}) = E_m(\{\mathbf{R}_a\})\Phi_m(\{\mathbf{R}_a\}, \{\mathbf{r}_i\}) , \quad (2.5)$$

with the eigenvalue  $E_m$ , which depends parametrically on the set of nuclear coordinates  $\{\mathbf{R}_a\}$ . The entire dynamics of the system is recovered by the atomic nuclei obeying the relation

$$i\hbar \frac{\partial}{\partial t} \chi_m(\{\mathbf{R}_a\}; t) = [\hat{T}_n + \hat{V}_{nn} + E_m(\{\mathbf{R}_a\})]\chi_m(\{\mathbf{R}_a\}; t) . \quad (2.6)$$

The above equations pave the way to treat the two subsystems separately, but coupled via the Born-Oppenheimer energy surface  $E_m(\{\mathbf{R}_a\})$ . In the following the main ideas for solving eq. (2.5) via density functional theory (DFT) and the classical analogue of eq. (2.6) with molecular dynamics (MD) simulations are given briefly. For further reading on DFT, the interested reader is referred to review articles [113–117] as well as the books by Kohanoff [118] and Martin [119]. More details on the numerical concepts of MD can be found in the books by Frenkel and Smit [120], Marx and Hutter [121], Rapaport [122] and Tuckerman [123].

## 2.2. Density functional theory (DFT)

For a long time much attention has been paid to the efficient approximation of the wave function in eq. (2.5) maintaining its correct symmetry, such as in Hartree-Fock theory incorporating Slater determinants [117]. With growing computational power much more accurate wave function based methods like Møller-Plesset perturbation theory, configuration interaction and coupled clusters have become available [124]. However, these



approaches are still computationally demanding, so that their applicability is limited. Opposed to these quantum chemistry methods, there have been major efforts in many-particle physics to reformulate the problem avoiding the wave function. These methods comprise the Green's function techniques, density matrix theory and the by far most successful density functional theory. The latter method is employed in this work, since it has proven to be very efficient for material applications, while being sufficiently accurate at the same time.

The fundamental quantity in DFT is the electron density  $n(\mathbf{r})$ , which can be expressed as one-particle distribution function,

$$n(\mathbf{r}) = N_e \int \cdots \int d^3r_2 \dots d^3r_{N_e} |\Phi_m(\{\mathbf{r}_i\})|^2, \quad (2.7)$$

normalized to the number of electrons  $N_e$ :

$$\int d^3r n(\mathbf{r}) = N_e. \quad (2.8)$$

Replacing the high-dimensional wave function  $\Phi_m(\{\mathbf{r}_i\})$  by the three-dimensional electron density containing solely the necessary information reduces the numerical effort substantially. Its basic idea has already been present in the treatment of the homogeneous electron gas proposed by Thomas, Fermi and Dirac [125–127]. The foundation of DFT in today's formulation was laid by Hohenberg and Kohn [128], who introduced the following two-part theorem for the ground state [128]:

1. The external potential  $\hat{V}_{en}$  is (except for a constant) a unique functional of the electron density  $n(\mathbf{r})$ . Since, in turn,  $\hat{V}_{en}$  determines the Hamiltonian,  $\hat{H}_e = \hat{T}_e + \hat{V}_{ee} + \hat{V}_{en}$ , the many-particle ground state is a unique functional of  $n(\mathbf{r})$ .
2. The Hohenberg-Kohn functional,  $J_{HK}[\tilde{n}(\mathbf{r})] = T_e[\tilde{n}(\mathbf{r})] + E_{ee}[\tilde{n}(\mathbf{r})]$ , yields the ground state energy, if and only if the electron density  $\tilde{n}(\mathbf{r})$  is the true electron density  $n(\mathbf{r})$ .

The above Hohenberg-Kohn theorem shows mathematically the feasibility of the electron density approach [128]. In the next section the Kohn-Sham formalism is discussed, which makes it possible to apply this method.

### 2.2.1. Kohn-Sham formalism for finite temperatures

Originally, DFT was developed as a ground state theory, but shortly after Hohenberg and Kohn had published their idea, Mermin developed an extension to finite temperatures [129]. As a consequence, the quantity that has to be minimized is the free energy,

$$F[n(\mathbf{r})] = E_m[n(\mathbf{r})] - TS[n(\mathbf{r})], \quad (2.9)$$

rather than the previously discussed ground state energy  $E_m[n(\mathbf{r})]$ . In this expression  $S[n(\mathbf{r})]$  represents the entropy, while  $T$  is the electronic temperature, which is equal to the ionic temperature throughout this work.

The main idea of the Kohn-Sham formalism is to rewrite eq. (2.9) by using a reference

system of non-interacting electrons [130]. Denoting the reference system by index  $R$ , its kinetic energy is written as

$$T_R[n(\mathbf{r})] = -\frac{\hbar^2}{2m_e} \sum_{i=1}^{\infty} f_i \int d^3r \phi_i(\mathbf{r}) \nabla_i^2 \phi_i(\mathbf{r}) , \quad (2.10)$$

and the entropy of the non-interacting reference system has the analytic form

$$S_R[n(\mathbf{r})] = -k_B \sum_{i=1}^{\infty} [f_i \ln(f_i) + (1 - f_i) \ln(1 - f_i)] . \quad (2.11)$$

In this formulation  $f_i$  indicates the fractional occupation number, which can be expressed via the Fermi-Dirac distribution:

$$f_i = f(\varepsilon_i) = \frac{1}{e^{(\varepsilon_i - \mu_e)/k_B T} + 1} . \quad (2.12)$$

In this equation  $k_B$  represents the Boltzmann constant,  $\mu_e$  is the chemical potential and  $\varepsilon_i$  describes the eigen energy of the respective Kohn-Sham orbitals  $\phi_i(\mathbf{r})$ . These one-particle orbitals are the elements of the Slater determinant, which is used to describe the total wave function of the non-interacting reference system [118]. Using the reference system, the free energy is expressed as

$$F[n(\mathbf{r})] = T_R[n(\mathbf{r})] + E_H[n(\mathbf{r})] + E_{en}[n(\mathbf{r})] - TS_R[n(\mathbf{r})] + F_{xc}[n(\mathbf{r})] . \quad (2.13)$$

This free energy formulation solely contains exactly known terms, except for the exchange-correlation term [129; 130],

$$F_{xc}[n(\mathbf{r})] = T_e[n(\mathbf{r})] - T_R[n(\mathbf{r})] + E_{ee}[n(\mathbf{r})] - E_H[n(\mathbf{r})] - TS[n(\mathbf{r})] + TS_R[n(\mathbf{r})] , \quad (2.14)$$

which encapsulates all unknown quantities [130]. For example, the difference  $E_{ee} - E_H$  describes the electron-electron interaction beyond the well-known Hartree energy term,

$$E_H[n(\mathbf{r})] = \frac{1}{2} \frac{e^2}{4\pi\epsilon_0} \int \int d^3r d^3r' \frac{n(\mathbf{r})n(\mathbf{r}')}{|\mathbf{r} - \mathbf{r}'|} . \quad (2.15)$$

Furthermore, the external energy can be calculated in the following way:

$$E_{en}[n(\mathbf{r})] = - \sum_{a=1}^{N_n} \frac{Z_a e^2}{4\pi\epsilon_0} \int d^3r \frac{n(\mathbf{r})}{|\mathbf{r} - \mathbf{R}_a|} . \quad (2.16)$$

All of the above equations enter a self-consistent cycle consisting of the three following Kohn-Sham equations [118; 130] encompassing the electron density,

$$n(\mathbf{r}) = \sum_{i=1}^{\infty} f_i |\phi_i(\mathbf{r})|^2 , \quad (2.17)$$

the effective potential,

$$v_{eff}(\mathbf{r}) = \frac{e^2}{4\pi\epsilon_0} \int d^3r' \frac{n(\mathbf{r}')}{|\mathbf{r} - \mathbf{r}'|} - \sum_{a=1}^{N_n} \frac{Z_a e^2}{4\pi\epsilon_0} \frac{1}{|\mathbf{r} - \mathbf{R}_a|} + \frac{\delta}{\delta n(\mathbf{r}')} F_{xc}[n(\mathbf{r})] , \quad (2.18)$$

and finally, the effective one-particle Schrödinger equation

$$\left[ -\frac{\hbar^2}{2m_e} \Delta + v_{eff}(\mathbf{r}) \right] \phi_i(\mathbf{r}) = \varepsilon_i \phi_i(\mathbf{r}) . \quad (2.19)$$

This formalism is not entirely free from wave functions, since the Kohn-Sham orbitals are essential for the described self-consistent treatment. An alternative approach is provided by orbital-free DFT, which is very successfully applied for very high temperatures [131–133]. However, it is not (yet) practicable in the warm dense matter regime investigated in this work.

### 2.2.2. Approximations for the exchange-correlation functional

In principle, DFT is exact and the only task left is to find an expression for the exchange-correlation functional  $F_{xc}[n(\mathbf{r})]$ . It turns out that this is by no means trivial, since one heavily relies on approximations, which have a direct impact on the quality of the simulation results. Therefore, the exchange-correlation functional should be chosen with great care depending on the studied system.

Generally, there is a broad range of existing approximations with different levels of accuracy. They form a hierarchy that is often represented by the rungs of a ladder [134]. The lowest tier is the local density approximation (LDA), which describes the inhomogenous electron gas locally as homogenous [130]. This treatment is usually applied to systems with locally weakly varying electron density. This class also provides the only feasible finite-temperature functionals to date [135]. More sophisticated finite-temperature exchange-correlation functionals are lacking in literature and therefore, the common, very profound approximation is made that the free energy functional is sufficiently described by the ground state energy functional  $E_{xc}[n(\mathbf{r})]$  [118].

Besides the electron density itself, generalized gradient approximation functionals take into account the gradient of the electron density:

$$E_{xc}^{GGA}[n(\mathbf{r})] = \int d^3r n(\mathbf{r}) \varepsilon_{xc}^{GGA}[n(\mathbf{r}), \nabla n(\mathbf{r})] . \quad (2.20)$$

In this work, we use the exchange-correlation functional proposed by Perdew, Burke and Ernzerhof (PBE) [136], which is a good compromise between accuracy and computational cost. This functional gives better lattice constants [137], binding energies and thermodynamic properties such as the enthalpy [138] compared to LDA. However, PBE is known to yield too small band gaps due to the self-interaction error [118], which usually is corrected for by using hybrid functionals such as the HSE [139]. These functionals are computationally very demanding. Hence, their employment is limited to physical properties such as electronic transport properties [140], which are not part of this work. Additionally, PBE does not include non-local van-der-Waals forces, which are in a growing number of

functionals included nowadays [141; 142]. However, all of those van-der-Waals functionals are empirical to a certain extent. Therefore, our calculations are entirely performed using the PBE functional, which is free of empirical parameters and was constructed to fulfill as many physical constraints as possible. Moreover, if desired, it is possible to correct EOS data for any functional induced error in a post-processing scheme [143].

### 2.3. Molecular dynamics (MD)

The framework outlined in the previous section allows the computation of the electronic properties for a given static configuration of the nuclei. The dynamics of the total system are fully mapped onto the nuclei, which are treated via classical molecular dynamics. The particles are arranged in a simulation box of volume  $V$ , which is periodically repeated in all directions to minimize surface effects. This simulation method was introduced by Alder and Wainwright [144; 145] and provides direct access to the particle trajectories, which are described by Newton's equations of motion [118; 146],

$$M_a \ddot{\mathbf{R}}_a = \underbrace{-\nabla_a E_{nn}(\{\mathbf{R}_a\})}_{\mathbf{F}_{a,nn}} \underbrace{-\nabla_a E_m(\{\mathbf{R}_a\})}_{\mathbf{F}_{a,en}} \underbrace{-M_a \dot{\mathbf{R}}_a \frac{\dot{s}}{s}}_{\mathbf{F}_{a,bath}} = \mathbf{F}_a(\{\mathbf{R}_a\}) , \quad (2.21)$$

representing the classical analogue of eq. (2.6) for a canonical ensemble.

In the above equation, the total force  $\mathbf{F}_a(\{\mathbf{R}_a\})$  comprises three parts.  $\mathbf{F}_{a,nn}$  is the force resulting from the Coulomb interaction between the nuclei, while the force  $\mathbf{F}_{a,en}$  originates from the interaction of the nuclei with the electrons. Due to the coupling with a heat bath to realize the canonical ensemble, there is an additional force for the ion motion,  $\mathbf{F}_{a,bath}$ . Here, the heat bath is described by using the Nosé thermostat [146; 147]. In this formalism, an additional dynamic quantity  $s = s(t)$  is introduced, resulting in the Hamilton function of the heat bath [146]:

$$H_{bath} = \frac{1}{2} Q \left( \frac{\dot{s}}{s} \right)^2 + 3(N_n - 1) k_B T \ln s , \quad (2.22)$$

with the Boltzmann constant  $k_B$ . The additionally introduced degree of freedom  $s$  satisfies the following equation of motion [146]:

$$Q \ddot{s} = s \sum_{a=1}^{N_n} M_a \dot{\mathbf{R}}_a^2 - 3(N_n - 1) k_B T s + Q \frac{\dot{s}^2}{s} . \quad (2.23)$$

From this expression, the force  $\mathbf{F}_{a,bath}$  is determined, entering eq. (2.21).

The introduced heat bath periodically adds or extracts energy to/from the system maintaining the time-averaged kinetic energy of the nuclei [147]

$$\langle T_n \rangle = \frac{3}{2} (N_n - 1) k_B T . \quad (2.24)$$

This enables us to choose the temperature as an independent simulation parameter along with the number of particles  $N_n$  and the volume  $V$  of the simulation cell. The energy

coupling is controlled via the characteristic frequency of the thermostat,

$$\omega_T = \sqrt{\frac{6(N_n - 1)k_B T}{Q}}, \quad (2.25)$$

which is determined by the frictional mass parameter  $Q$  [146; 147].

The forces  $\mathbf{F}_{a,nn}$  and  $\mathbf{F}_{a,bath}$  in eq. (2.21) are obtained directly from the molecular dynamics, in contrast to  $\mathbf{F}_{a,en}$ . This term is derived from the DFT calculation as gradient of the Born-Oppenheimer energy surface  $E_m(\{\mathbf{R}_a\})$  using the Hellmann-Feynman theorem [148; 149]. Thereby, it is sufficient to write the energy instead of the free energy, since the entropy term cancels out [146; 150; 151].

Nowadays up to trillions of particles are generally feasible in a MD simulation utilizing massive parallel computers, e.g., a recent study reported a simulation with  $4.125 \cdot 10^{12}$  particles [152]. Nevertheless, in a typical classical MD simulation up to  $10^6$  particles are handled, while the addition of the quantum treatment of the electrons discussed here reduces the number of feasible particles even further to 100 - 1000.

## 2.4. DFT-MD simulations with VASP

Throughout this work, the DFT-MD implementation in the Vienna Ab initio Simulation Package (VASP) [153–156] is employed to describe the considered H-C-N-O systems in the warm dense matter regime. The workflow of this code is illustrated in Fig. 2.1. For

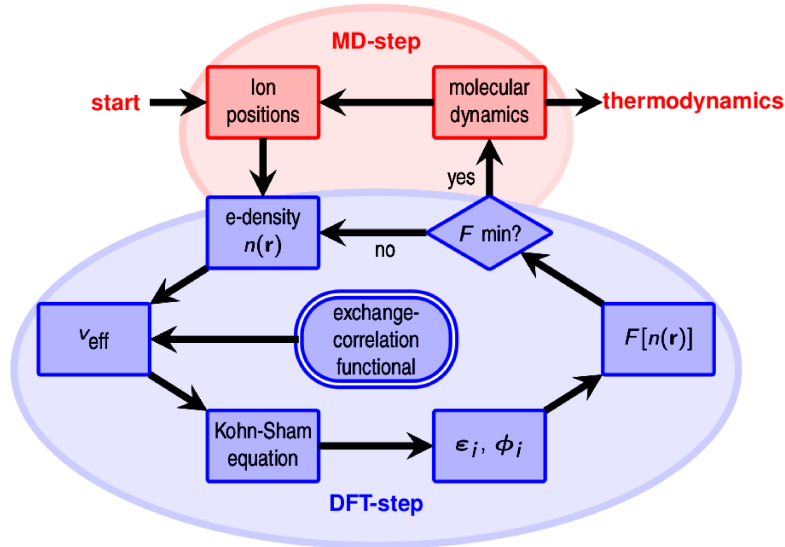


**Fig. 2.1.:** Schematic workflow of a DFT-MD simulation as implemented in the VASP code [156]. The illustration is taken from the Ph.D. thesis of Lorenzen [157].

a given starting configuration of the nuclei, the electron density is initially guessed and the free energy is calculated from the effective one-particle Schrödinger equation derived by Kohn and Sham as outlined in the previous section. This is repeated until the free energy reaches its minimum, so that the derived Hellmann-Feynman forces can enter

the  $N_n$  Newtonian equations of motion eq. (2.21) for the atomic nuclei. Finally, the thermodynamic properties are calculated at the time step and the nuclei positions are updated by integrating the Newtonian equations via a Verlet algorithm [146]. In the following, we present the most important technical details, the reader may be referred to the Ph.D. thesis by Kietzmann [158] for additional information.

First of all, VASP is working in real and momentum space to optimize efficiency as the potential energy has a diagonal representation in real space while the kinetic energy is of diagonal form in reciprocal space. The Brillouin zone is sampled using special  $\mathbf{k}$  points. Throughout this work, the Baldereschi Mean Value Point [159] has been used extensively. In some cases more than one  $\mathbf{k}$  point was needed to ensure convergence. Thereby, the scheme by Monkhorst and Pack has been applied [160].

Moreover, there exist two different major methodologies for the expansion of the basis set in modern DFT codes. One can either use local orbital basis sets as implemented in SIESTA [161] and FHI-aims [162] or employ a plane-wave basis set. The latter is used by VASP, as well as by Quantum Espresso [163], Abinit [164] and CASTEP [165]. The expansion of the Kohn-Sham orbitals is expressed by Bloch functions [118]:

$$\phi_i(\mathbf{r}) = \phi_{\mathbf{k}\mu}(\mathbf{r}) = \frac{1}{\sqrt{V}} u_{\mathbf{k}\mu}(\mathbf{r}) e^{i\mathbf{k}\cdot\mathbf{r}} = \frac{1}{\sqrt{V}} \sum_{\mathbf{G}} C_{\mathbf{k}\mu}(\mathbf{G}) e^{i(\mathbf{k}+\mathbf{G})\cdot\mathbf{r}} , \quad (2.26)$$

where  $u_{\mathbf{k}\mu}$  is the Bloch factor for a given  $\mathbf{k}$  point and band index  $\mu$ . The summation in the above equation is aborted as soon as the wave number  $\mathbf{G}$  results in a kinetic energy that exceeds the pre-defined energy cutoff,

$$E_{cut} > \frac{\hbar^2}{2m_e} |\mathbf{k} + \mathbf{G}|^2 . \quad (2.27)$$

Rewriting the Kohn-Sham equation with the plane-wave formalism, the following form is obtained for the reciprocal space [118]:

$$\sum_{\mathbf{G}'} \left[ \frac{\hbar^2}{2m_e} |\mathbf{k} + \mathbf{G}|^2 \delta_{\mathbf{G},\mathbf{G}'} + \hat{v}_{eff}(\mathbf{G} - \mathbf{G}') \right] C_{\mathbf{k}\mu}(\mathbf{G}') = \varepsilon_{\mathbf{k}\mu} C_{\mathbf{k}\mu}(\mathbf{G}) . \quad (2.28)$$

Additionally, VASP uses projector-augmented wave (PAW) pseudopotentials [166], so that it is possible to treat only relevant electrons, e.g., valence electrons, explicitly in the simulation. At the same time, the core electrons are embedded in the core potential, allowing us to cut off any oscillation of the wave function close to the core. Due to the frozen core electrons, we will often use the term ion instead of nucleus in the following. Finally, it should be noted that prior to generating the actual calculation results present in this thesis, extensive convergence tests with respect to particle number,  $\mathbf{k}$  point sets, energy cutoff, used pseudopotential, timestep and simulation duration have been performed. Additionally, the results have been checked against experimental data and other simulation results whenever it was possible.

# 3. Computational methods and simulation details

After outlining the general method for treating the many-particle problem and its implementation in VASP in the previous chapter, we present the most important details on the data analysis as well as some further computational tools.

## 3.1. Equations of state (EOS) and Hugoniot curve

The thermal  $p(\varrho, T)$  and caloric  $U(\varrho, T)$  equations of state are constructed from a series of DFT-MD simulations carried out for various densities and temperatures. For each simulation the pressure  $p$  and internal energy  $U$  are calculated after equilibration of the system by evaluating the following expressions:

$$p = \frac{N_n \varrho k_B T}{m} + \langle p_{nn} \rangle + \langle p_e \rangle, \quad (3.1)$$

$$U = \frac{3}{2} N_n k_B T + \langle E_{nn} \rangle + \langle F[n(\mathbf{r})] + TS_R[n(\mathbf{r})] \rangle. \quad (3.2)$$

The first term in both equations refers to the ideal contribution of the ions, the second term is their interaction contribution, while the last term describes the total contribution from the electronic system. The expression for  $U$  is directly obtained by combining eq. (2.21) and eq. (2.13). For the pressure, the interaction part for the ions is calculated via the virial theorem [122; 167], while the total pressure for the electronic system is derived from the analogous quantum mechanical virial theorem [119; 168; 169]. The brackets  $\langle \rangle$  indicate a time average.

Note that from here on we will use the intensive quantity specific internal energy  $u$ , which is defined as internal energy divided by the total system's mass. Due to the classical treatment of the ions via the Newtonian equations of motion, we are not able to capture the zero-point motion energy. Therefore, a quantum correction term ( $u_{qc}(\varrho, T)$ ) based on the quasi-harmonic approximation is added to the DFT result  $u(\varrho, T)$  in a post-processing scheme, yielding the corrected specific internal energy

$$u^*(\varrho, T) = u(\varrho, T) + u_{qc}(\varrho, T). \quad (3.3)$$

The correction term is obtained by performing a spectrum-weighted frequency integration that adds the quantum statistical energy of a harmonic oscillator and subtracts the respective classical energy for each frequency interval  $d\nu$  [170]:

$$u_{qc}(\varrho, T) = \frac{3N_n}{m} \int_0^\infty d\nu S(\nu, \varrho, T) \left[ h\nu \left( \frac{1}{2} + \frac{1}{e^{(h\nu/k_B T)} - 1} \right) - k_B T \right]. \quad (3.4)$$

### 3. Computational methods and simulation details

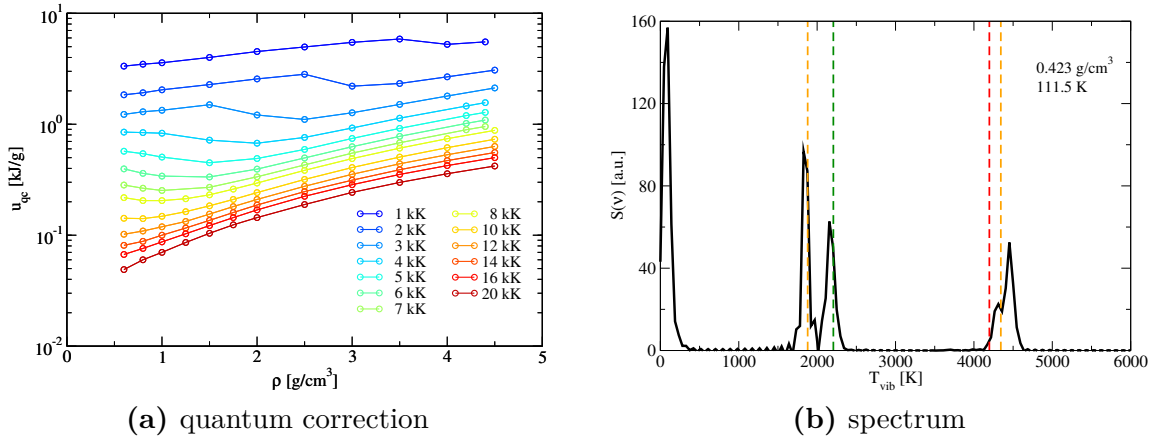


**Fig. 3.1.:** Quantum correction of the caloric EOS  $u_{qc}$  (a) and exemplary vibrational spectrum (b) of methane. The dashed lines in figure (b) are experimentally determined vibrational frequencies, where the color indicates non-degenerate (red), two-fold (green) and three-fold degenerate (orange) vibrations of the CH<sub>4</sub> molecule.

The vibrational spectrum  $S(\nu, \rho, T)$  can be calculated using either experimentally determined vibrational frequencies or by computing it directly from the DFT-MD data evaluating the velocity autocorrelation function  $\langle \mathbf{V}_a(t) \cdot \mathbf{V}_a(0) \rangle$ . Both approaches have been successfully applied to water [171] and ammonia [172]. The complementary quantum correction of methane is plotted in Fig. 3.1 along with an exemplary vibrational spectrum at 111.5 K and 0.423 g/cm<sup>3</sup>. The calculated methane spectrum is in good agreement with the experimental vibrational frequencies, similar to our findings for ammonia [172]. Interestingly, the quantum correction has a very pronounced kink for temperatures up to 3000 K, which coincides with a change in the diffusive properties as will be discussed in section 4.2. Furthermore, it should be noted that there exists at least one alternative approach to account for the quantum correction of the caloric EOS, which yields similar results [173].

The EOS obtained from the DFT-MD calculations can be verified by comparison to experimental data, which are usually either obtained from static DAC experiments or dynamic compression experiments. Typical states that are easily accessible by dynamic compression experiments are described with the Hugoniot curve [174]:

$$u_1 - u_0 = \frac{1}{2}(p_1 + p_0) \left( \frac{1}{\rho_0} - \frac{1}{\rho_1} \right). \quad (3.5)$$

The above equation relates specific internal energy, pressure, and density of the initially prepared state, indicated by index 0, with the state present after the material has been shocked, which is indicated by index 1. The Hugoniot curve has been studied several times for water, ammonia, methane and the so-called synthetic Uranus mixture by gas gun experiments [68; 175–179]. In case of water exist many further experimental Hugoniot data [106; 180–183].



## 3.2. Structural and transport properties

Changes in slope of the thermal and caloric EOS as well as prominent features in the resulting Hugoniot curve may indicate phase transitions, which are most commonly accompanied by structural rearrangements of the electrons and ions. In this work, the resulting structural properties in the form of pair distribution functions and bonding autocorrelation functions are analyzed for each studied phase. Along with the diffusion coefficients and mean square displacements, this analysis is the basis to construct the phase diagrams for the considered H-C-N-O systems.

### 3.2.1. Pair distribution functions

The pair distribution function is a measure for the probability to find a particle of species  $\alpha$  at a distance  $r$  from a particle of species  $\beta$ . This quantity can be generally expressed as two-particle distribution function, which is reduced to the following form utilizing its radial symmetry [167]:

$$g(r) = g_{\alpha\beta}(r) = \frac{V}{4\pi r^2 N_\alpha (N_\beta - \delta_{\alpha\beta})} \left\langle \sum_{i=1}^{N_\alpha} \sum_{j=1}^{N_\beta} \delta(r - r_{ij}) \right\rangle. \quad (3.6)$$

In this notation  $N_\alpha$  and  $N_\beta$  describe the number of particles for the respective species, while the distance between two particles  $i$  and  $j$  is denoted by  $r_{ij}$ . In the presence of only one particle type, i.e.  $\alpha = \beta$ , the additional constraint  $j > i$  needs to be considered in the summation. Moreover,  $\delta_{\alpha\beta}$  is the Kronecker delta, whereas  $\delta(r - r_{ij})$  represents the Dirac delta function.

The pair distribution function is a real space quantity, which is normalized to the volume  $V$ . It is indirectly accessible by scattering experiments, since it can be obtained as fourier transform of the structure factor, which is probed in  $k$  space. However, to our knowledge there are no studies of the high-pressure H-C-N-O compounds considered in this work.

### 3.2.2. Bonding autocorrelation functions (BACF)

Pair distribution functions provide useful indications of properties such as dissociation degree of a given molecular system. While the DFT-MD simulations are built upon the physical picture describing interacting electrons and atomic nuclei, we are interested in characterizing our H-C-N-O systems in terms of chemical bonding. Therefore, we introduce the bonding autocorrelation function (BACF) [68; 184],

$$\beta(t) = \frac{\langle B(t)B(0) \rangle}{\langle B(0)^2 \rangle}. \quad (3.7)$$

For an existing bond, the binary object  $B(t)$  equals one, whereas it is set to zero when the bond does not exist. The brackets indicate an ensemble average and the function is normalized to one for the starting point at  $t = 0$ . The cutoff what to call a bond is somewhat arbitrary, here we choose the first minimum of the pair distribution function as criterion. The lifetime of the bond is then determined by a fitting procedure described in [184].

### 3.2.3. Diffusion coefficients and mean square displacements

Diffusion coefficients describe the mobility of particles according to their thermal energy, which is referred to as Brownian motion. In an isotropic system the self-diffusion coefficient  $D_\alpha$  of particle species  $\alpha$  can be calculated via the Green-Kubo formula [167]

$$D_\alpha = \frac{1}{3N_\alpha} \lim_{t \rightarrow \infty} \int_0^t d\tau \sum_{a=1}^{N_\alpha} \langle \mathbf{V}_a(\tau) \cdot \mathbf{V}_a(0) \rangle , \quad (3.8)$$

using again the velocity autocorrelation function. This method yields slightly better results with typical errors of about 10% compared to a formally equivalent formulation using the mean square displacements,

$$\langle (\Delta \mathbf{R}_a)^2 \rangle = \sum_{a=1}^{N_\alpha} \langle [\mathbf{R}_a(t) - \mathbf{R}_a(0)]^2 \rangle . \quad (3.9)$$

However, the mean square displacements itself proved to be very insightful in determining, whether a crystal lattice is stable throughout a simulation. Therefore, this quantity has been used to detect solid phases along with the pair distribution functions [172; 185].

## 3.3. Crystal Structure Prediction (CSP)

For most of our simulations in the warm dense matter regime, it is sufficient to start the simulation from a cubic lattice such as fcc or bcc. However, for the superionic phase of the mixture, we realized that the system is not correctly described using a cubic crystal structure for the ions. This became evident in our analysis of the structural properties, discussed in the previous section, as well as in the EOS data, which are shown in Fig. A.1.

In this section we briefly summarize the basic idea and different approaches of crystal structure prediction. This is a fast-growing research area, accelerated by increasing computational power and the availability of diffraction experiments with DACs reaching routinely the Mbar pressure range [20]. Therefore, it is suggested to study the recent review articles by Wang and Ma [186] as well as Zurek and Grochala [187] for a more detailed overview and numerical details.

The aim of every crystal structure prediction method is the same: finding the global minimum of the multi-dimension potential-energy surface (PES) in an efficient way. The special difficulty here lies in the fact that there are many local minima and ensuring that the global minimum has been found is challenging.

There exist different approaches, which can be divided into two general classes, biased and unbiased searches [186]. Biased structure searches exploit databases of known structures, which makes the crystal prediction very efficient. However, these methods are not capable of generating truly new structures. The most successful unbiased methods comprise random sampling as implemented in AIRSS [188], genetic and evolutionary algorithms, which are the heart of XtalOpt [189] and USPEX [190] as well as particle swarm optimization algorithms used in CALYPSO [191]. Moreover, there are several

other methods, which are designed to overcome energy barriers including simulated annealing, basin hopping, minima hopping, and metadynamics [186]. Nevertheless, those approaches are partially biased as they rely on initially guessed input structures.

In the following the basics of the evolutionary structure searching code XtalOpt, used in this work, are introduced. Subsequently, it is outlined how the equations of state are obtained for the predicted 0 K crystal structures in order to identify the favored thermodynamic phases.

### 3.3.1. Evolutionary structure search with XtalOpt

In this work we use the evolutionary approach implemented in the open source code XtalOpt [189], which is built into Avogadro [192]. It contains a wrapper for various DFT codes including VASP, which we use here, and has been applied successfully to water by another group prior to this work [42].

Crystal structure prediction based on evolutionary algorithms such as XtalOpt [189] can be understood as an analogue to the biological principles its name is derived from. Each considered candidate structure of a single iteration of the code is referred to as an individual of a generation. The enthalpy is computed for each individual within one generation and can be optimized by a customary chosen iterative scheme. In our CSP runs, we performed three VASP runs for every considered structure. In a first run the enthalpy was calculated for fixed atomic positions and fixed lattice vectors, then the atoms were allowed to move in a second run and finally in a third run, the atomic positions as well as the lattices vectors were allowed to change. Other schemes involving two or four optimization steps were tested, however the threefold scheme yielded the best results.

A new generation is obtained by modifying the individuals of the current generation via procreation. Thereby, a new structure (offspring) can be formed from either one or two parent structures. If solely one parent is involved this process is called mutation opposed to the process involving two parents, which is referred to as breeding. Both procreation types are illustrated in Fig. 3.2. XtalOpt provides six different operators to construct new offsprings [189]. Breeding is performed via the crossover operation, which cuts two parents and assembles them to a new offspring. There are five operators left for the mutation. In Fig. 3.2 the permutation is shown exemplary, which exchanges the positions of two arbitrary atoms of the parent structure.

XtalOpt allows to choose the amount for mutation and breeding to be included in the searching process. Further input parameters are the starting pool size and the number of structures taken from one generation to the next. Also the volume, lengths of axis vectors, and angles between them can be set. Furthermore, structures can be seeded throughout the searching process to accelerate the procedure, however, this might bias the CSP. Duplicate structures are identified throughout the XtalOpt run and are systematically removed [193].

Due to the variety of input parameters, it is challenging to ensure convergence of the XtalOpt run. Typically, we ran at least five generations with a pool size of 50 structures. We performed several XtalOpt runs for different system sizes up to 16 molecules in the box and varied the input parameters outlined above.

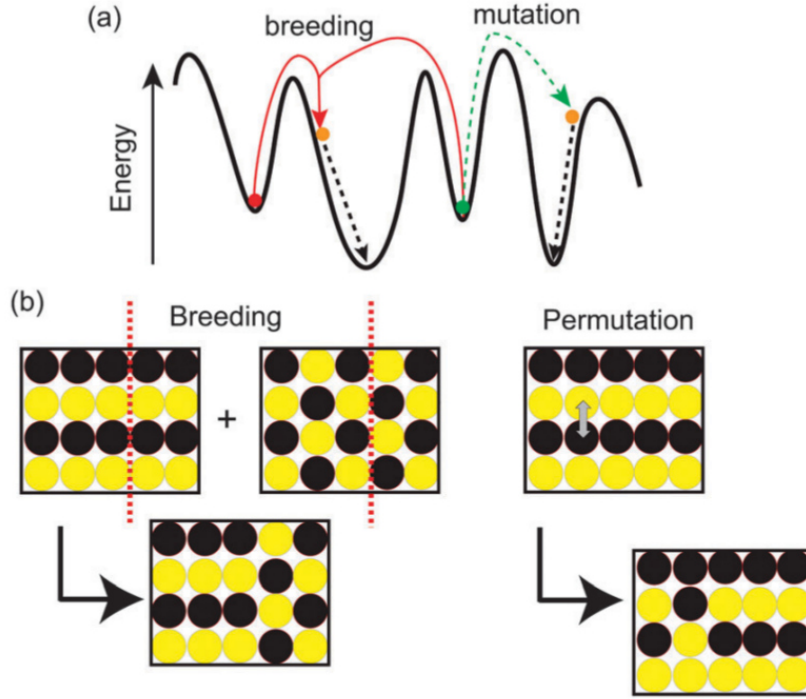


**Fig. 3.2.:** Illustration of the basic idea of evolutionary structure prediction taken from Zurek and Grochala [187]. Figure (a) shows the evolution of two initial structures (green and red circles) on the potential energy surface (PES). The initial structures and their modifications, which result in the orange circles on the PES, are illustrated in figure (b).

### 3.3.2. Quasi-harmonic approximation employing Phonopy

The crystal structure prediction is usually carried out at selected pressures. From these results, cold curves ( $T = 0$  K) are determined using static VASP simulations to cover the entire desired pressure range. Since these calculations do not include any dynamics, our post-processing scheme to obtain the quantum-correction presented in section 3.1 is not applicable. Therefore, we perform additional phonon calculations with Phonopy [194] to compute the zero-point motion energy, which is added to the thermodynamic properties obtained with VASP. Evaluating the respective results within the quasi-harmonic approximation [195; 196] leads to the equations of state for the solid phases with the predicted crystal structures and allows us to calculate phase transitions between them. In order to obtain the free energy of the phonons, the potential describing the interaction between the nuclei is expanded in a Taylor series centered at the equilibrium positions of the nuclei  $\{\mathbf{R}_a^0\}$ :

$$V_{nn}(\{\mathbf{R}_a\}) = V_{nn}(\{\mathbf{R}_a^0\}) + \underbrace{\sum_{a,\theta} \frac{\partial V}{\partial R_{a,\theta}} \Big|_{\{\mathbf{R}_a^0\}}}_{=0} x_a^\theta + \frac{1}{2} \sum_{a,b,\theta,\lambda} \underbrace{\frac{\partial^2 V}{\partial R_{a,\theta} \partial R_{b,\lambda}} \Big|_{\{\mathbf{R}_a^0\}}}_{A_{a,b}^{\theta,\lambda}} x_a^\theta x_b^\lambda + \dots \quad (3.10)$$

for finite displacements  $x_a^\theta$  with  $\theta = 1, 2, 3$ . Within the quasi-harmonic approximation the above expansion of the potential higher-order terms than quadratic term are neglected.

For each displacement an equation of motion can be formulated,

$$M_a \ddot{x}_a^\theta = - \sum_{b \neq a, \lambda} A_{a,b}^{\theta, \lambda} x_b^\lambda, \quad (3.11)$$

where  $A_{a,b}^{\theta, \lambda}$  is the matrix containing the force constants of the atomic nuclei. The displacements are expanded into a plane-wave basis

$$x_a^\theta = \frac{\tilde{x}_a^\theta}{\sqrt{M_a}} e^{-i\omega_\kappa t}. \quad (3.12)$$

The above expression is inserted into eq. (3.11), which leads to an eigenvalue equation with the eigenvalues  $(\omega_\kappa)^2$  [196]. The resulting phonon frequencies  $\omega_\kappa$  are inserted into the following formula for the specific free energy [197]

$$f_{ph}(T) = \sum_{\kappa} \left[ \frac{1}{2} \hbar \omega_\kappa + k_B T \ln(1 - e^{-\frac{\hbar \omega_\kappa}{k_B T}}) \right]. \quad (3.13)$$

The obtained specific free energy contains no explicit dependence on the volume. Therefore, the computation of the phonons has to be carried out for several points along the coldcurve, so that  $f(T, v)$  can be constructed. From this expression the specific entropy of the phonons,

$$s_{ph} = - \left( \frac{\partial f_{ph}}{\partial T} \right)_V, \quad (3.14)$$

as well as the specific internal energy of the phonons,  $u_{ph} = f_{ph} + T s_{ph}$ , are derived. The pressure is given by

$$p = \varrho^2 \frac{\partial}{\partial \varrho} (f + f_{ph}). \quad (3.15)$$

The specific Gibbs free energy can be calculated in the following way:

$$g(p, T) = u + u_{ph} - Ts - T s_{ph} + pv, \quad (3.16)$$

where  $Ts$  is the specific entropic contribution of the electrons and  $v$  is the total system volume divided by its total mass. The phase boundaries between the different considered solids, identified from the crystal structure prediction, are obtained by comparing the specific Gibbs free energies. The solid structure with the minimal specific Gibbs free energy is the thermodynamic stable phase.



## 4. Outline of the obtained results

Ammonia, methane, as well as binary and ternary mixtures including water have been investigated by employing the computational tools described in the previous two chapters. Most of the results outlined in the present chapter have already appeared in peer-reviewed journals. The corresponding publications are referred to as papers I [172], II [185], III [184], and IV [198] and can be found in chapter 5 along with one additional manuscript, paper V [199], which is in preparation.

Note that pure water is disregarded here, since its thermodynamic high-pressure properties have been subject to numerous experimental and theoretical studies. The reader may be referred to the Ph.D. thesis by French [27] and the references therein.

### 4.1. Ammonia

In a pioneering study Cavazzoni *et al.* [46] investigated the high-pressure phase diagrams of water and ammonia on a coarse grid using Car-Parrinello molecular dynamics. They predicted great similarities of those two materials including a novel phase, which is the superionic phase. This phase is characterized by a large proton conductivity due to highly mobile hydrogen ions diffusing through a lattice of nitrogen and oxygen ions, respectively. These findings motivated us to start our initial investigation of molecular compounds with the thermodynamic and structural properties of ammonia, which are compiled in paper I [172].

One of the two main results for  $\text{NH}_3$  is the phase diagram, which is shown in Fig. 4.1. It has been calculated up to 330 GPa and comprises four different phases as well as a transient region dominated by the diatomic molecules  $\text{N}_2$  and  $\text{H}_2$ . At comparatively small pressures and temperatures up to 1000 K a rotationally disordered phase is predicted, which is characterized by an fcc lattice formed by freely rotating  $\text{NH}_3$  molecules. As the pressure is increased, this solid phase transitions into a superionic phase, allowing the hydrogen atoms to become mobile as the NH bonds break. Upon heating the solid phase on the other hand, we find an ordinary molecular fluid, which starts to dissociate gradually above 3000 K. The corresponding pair distribution functions exhibit strong signs of diatomic nitrogen and hydrogen molecules at 4000 K and 5000 K, which in turn dissociate as temperature and pressure rise. Details on the characterization of the individual phases including structure analysis and diffusion coefficients can be found in paper I [172].

Our phase diagram agrees qualitatively well with that of Cavazzoni *et al.* [46], although the comparison is a little challenging due to different definitions of the phases. For example, they predict a metallic fluid due to band gap closure at 300 GPa and 5500 K, whereas we find the band gap to close already at 3000 K induced by thermal effects, which would

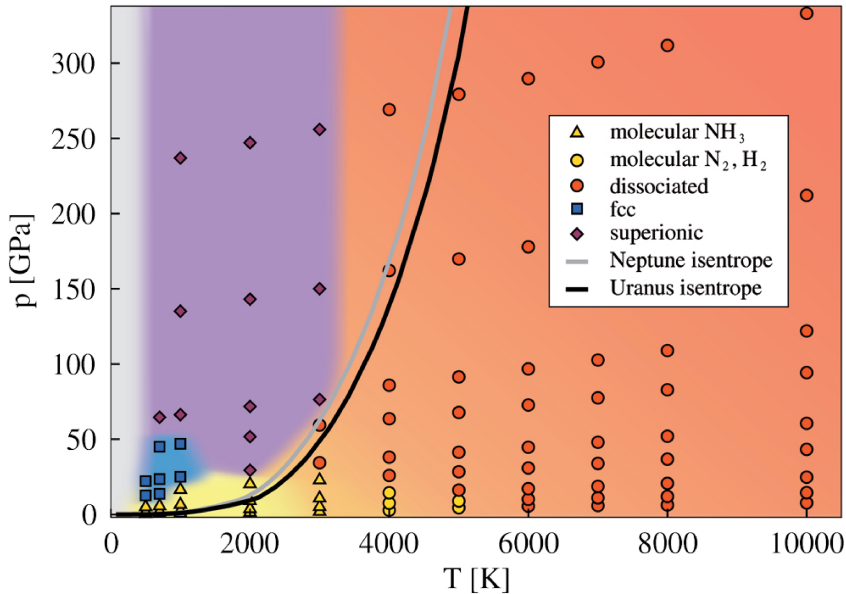


**Fig. 4.1.:** High-pressure phase diagram of ammonia determined via DFT-MD simulations in this work [172]. Each symbol in this plot represents an equilibrated simulation run. The isentropes of Uranus and Neptune are taken from Redmer *et al.* [94] and contain solely water as representative for planetary ices.

result in an electronically conducting fluid. On the other hand the predicted regions of the superionic phase agree very well, despite the different underlying nitrogen lattices. Cavazzoni *et al.* [46] predict an hcp lattice, while our simulations assume an fcc lattice. Our ammonia phase diagram has furthermore been compared to static diamond anvil cell experiments obtained by two different groups [33; 200]. The experimental data along with some accompanying simulations performed by Ninet *et al.* [33] strongly indicate a superionic phase above 700 K and 57 GPa, while Ojwang *et al.* [200] probed a similar region, but found no evidence of a superionic phase. Our calculations are in accordance with the conclusions drawn by Ninet *et al.* [33] and suggest that the data by Ojwang *et al.* [200] might need to be reinterpreted.

Our second major result for ammonia consists of the EOS, which has been computed for the entire pressure-temperature conditions inside Uranus and Neptune for the first time. Paper I [172] contains the EOS up to 330 GPa and 10000 K in tabulated form including the zero-point motion energy correction for the internal energy introduced in section 3.1. Recently, we extended the EOS up to 1000 GPa and 20000 K in order to cover the thermodynamic range relevant for adiabatic Uranus and Neptune models as well as a new class of Uranus models. Those contain a thermal boundary layer resulting into a significantly hotter planetary interior compared to previous models [198].

Prior to this work, there solely existed low-pressure EOS data up to 1 GPa for  $\text{NH}_3$  in literature as discussed in section 1.2.2. Therefore, we are restricted to comparing the Hugoniot curve, which is calculated from our EOS using eq. (3.5), to available shock compression data [175; 178; 179]. The Hugoniot curves calculated from our simulation data applying different approaches for the zero-point motion energy are generally in good



agreement with those experiments. However, none of our calculated Hugoniot curves reproduces the two temperature points determined by Radousky *et al.* [178]. Albeit it should be noted that including the quantum correction leads to a remarkable improvement in that regard. Li *et al.* [201] published a Hugoniot curve from DFT simulations that agrees slightly better with the experimentally determined temperatures, though they used significantly weaker convergence criteria compared to our work. Hence, the temperature along the Hugoniot curve remains a matter of investigation.

## 4.2. Methane

The icy deep interior of Neptune-like giant planets is believed to contain significant amounts of methane in addition to water and ammonia. Under the pressure-temperature conditions in giant planets  $\text{CH}_4$  molecules are suspected to decompose, and perhaps even to demix into diamond and hydrogen. In that scenario the heavier diamond might sink down to the core, while the light hydrogen ions would stay in the mantle [82; 202] as illustrated in Fig. 1.3 in section 1.3. This effect, which is also intensively debated for more complex hydrocarbons, has been subject to various experimental [95; 203–206] and theoretical studies [207–209].

Our investigations on methane are pursued in close collaboration with Hamel and Qi from the Lawrence Livermore National Laboratory, who have performed initial DFT-MD simulations up to 7000 K to calculate the EOS. On this data basis the preliminary phase diagram shown in Fig. 4.2 has been computed under the lead of Hamel. In particular, the entropy has been calculated via coupling-constant integration [211] using force-matching [212; 213] to construct effective potentials from the DFT-MD calculations. The results discussed in the following are not published yet, but some of them are planned to appear in paper V [199] contained in section 5.5.

This methane phase diagram contains new predictions for the lower and upper bounds of the melting line as well for the phase boundaries of demixing and the dissociation of  $\text{CH}_4$ . We find that the demixing line appears as a natural extension of the melting line toward higher pressures. While the demixing line is nearly independent of temperature, the melting line decreases strongly with temperature. Both lines appear to meet in the proximity of the dissociation region, which we find to decrease with temperature toward higher pressures. However, this is a preliminary picture. The calculations by Gao *et al.* [208] and the DAC experiments by Hirai *et al.* [95] suggest a more complex behavior. Gao *et al.* [208] combined structure prediction calculations at 0 K with the quasi-harmonic approximation to determine the most stable crystal structures. Thereby, they found molecular methane to be stable only below 100 GPa. A further increase of pressure leads to a progressive decomposition of  $\text{CH}_4$  into higher-order hydrocarbons coexisting with solid hydrogen. According to their study diamond does not form until a pressure of 300 GPa is reached and the phase separated hydrogen atoms adopt a liquid state. A similar behavior has been found in the experiments by Hirai *et al.* [95]. In future work the process of polymerization along with demixing needs to be studied in more detail.

Moreover, our predicted melting region has a slightly steeper slope than found experi-

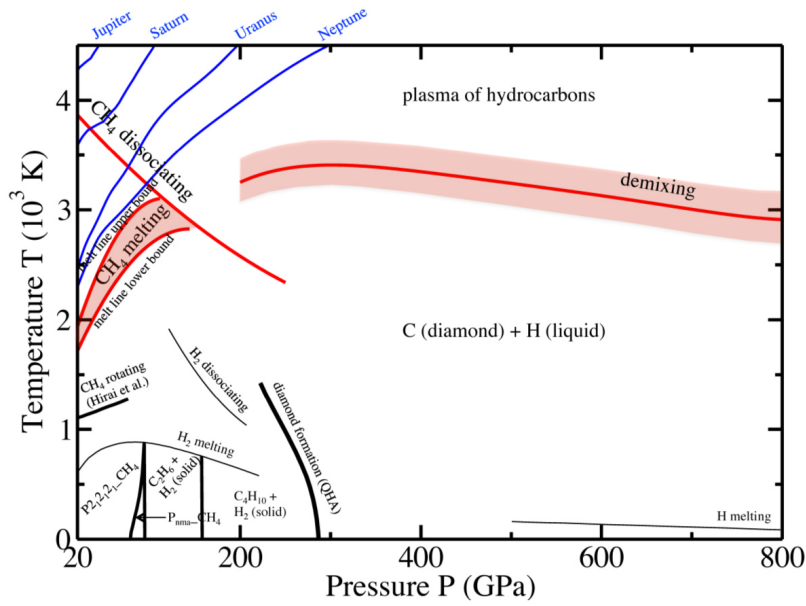


**Fig. 4.2.:** Preliminary high-pressure phase diagram of methane with special emphasis on the demixing region (courtesy of Hamel). The red lines indicate our predictions for the demixing region, the dissociation and the melting region of methane based on the initial EOS up to 7000 K calculated by Hamel and Qi. The black lines show the solid phases predicted by Gao *et al.* [208], the  $\text{CH}_4$  melting line determined by Hirai *et al.* [95] and relevant hydrogen phase boundaries taken from Chen *et al.* [210]. The blue lines indicate the isentropes of the respective giant planets [85; 88; 91].

mentally [95; 206] and its location is shifted by 1000 K upwards compared to Hirai *et al.* [95]. This deviation is believed to be partially caused by our assumption of a bcc lattice as well as the uncertainties in the melting temperature determination in the experiment and our simulations.

In this work, the EOS initially calculated by Hamel and Qi has been revisited and substantially extended to cover the pressure-temperature range relevant for all published Uranus models. The resulting thermal and the caloric equation of state of methane is shown up to 1.5 TPa and 20000 K in Fig. 4.3. The significant change in slope, characterizing the thermal as well as the caloric EOS, results from the dissociation process. Both plots also contain the EOS calculated by Sherman *et al.* [101], which overall agrees with our results within 2% in pressure except for some points in the melting region. There we find a deviation of up to 4% due to a slightly different prediction for the location of the melting region, which proved to be very sensitive to the simulation path due to chemical reactions. For the difference in internal energy between both EOS, we find values up to 1.0 kJ/g, which again can be traced back to the hysteresis effects found. Also, Sherman *et al.* [101] used a lower particle number as well as a lower energy cutoff compared to our simulations, so that the deviations might partially result from the different choice of simulation parameters.

The quality of the obtained EOS has been checked by comparison to the Hugoniot curve measured in gas gun experiments [178; 214]. The computed Hugoniot curves are shown

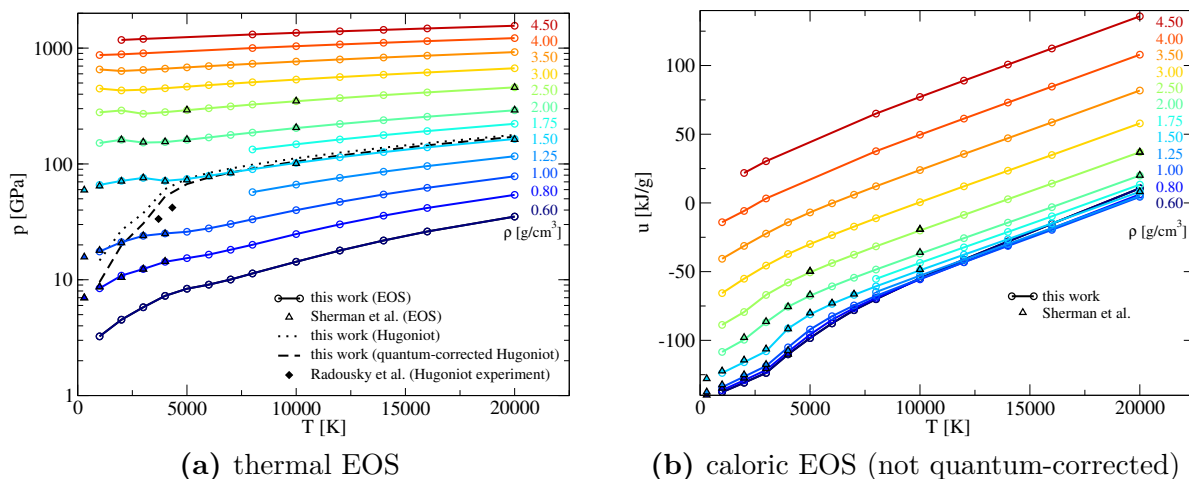


**Fig. 4.3.:** This work’s EOS of methane (solid lines with circles) along isochores in comparison to the EOS data by Sherman *et al.* [101] (triangles). Moreover, (a) shows the computed Hugoniot curve with (dashed black line) and without quantum correction (dotted black line) in comparison to the experimental results by Radousky *et al.* [178] (black diamonds).

with and without quantum correction of the internal energy in Fig. 4.3. As for ammonia, we underestimate the temperature for a given pressure in comparison to the data by Radousky *et al.* [178] indicating a systematic deviation between theory and experiment. Additionally, the diffusion coefficients for carbon and hydrogen have been calculated for the entire pressure-temperature range of the EOS. The results are plotted along isotherms in Fig. 4.4. Note that diffusion coefficients for solids are not contained in this plot, since atoms are tightly bound in a crystal lattice and possess typically very small diffusion coefficients, which lie beyond the resolution of our simulations.

In general, the diffusion coefficients of both species increase with temperature and decrease with pressure as has been found before for ammonia [172] and water [27]. However, there are some prominent features resulting most likely from phase transitions. Below 4000 K we find the diffusion coefficients to vanish in certain pressure ranges. The diffusion coefficients of hydrogen and carbon behave similarly at 3000 K. However, we find finite hydrogen diffusion coefficients for 1000 K and 2000 K at low pressures as well as at pressure above 800 GPa and 400 GPa, respectively. This behavior results from the underlying thermodynamic phases. For those temperatures, we find a molecular fluid at low pressures, which transitions into a solid as the pressure is increased. This is indicated by the vanishing diffusion coefficients of both H and C. For the highest considered pressures we find strong indications of demixing and formation of a carbon network with diffusive hydrogen ions at 1000 K and 2000 K. At 3000 K polymers are starting to form, which is indicated by the small diffusion coefficients of carbon as well as additional analysis of the pair distribution functions. Further studies of these phases are crucial for a profound understanding of the demixing in methane. For example, one should investigate different starting lattices of the simulations, since the chosen box symmetry as well as the particle number limit the direct demixing process in the box. So far, our calculated diffusion coefficients support our preliminary  $\text{CH}_4$  phase diagram.

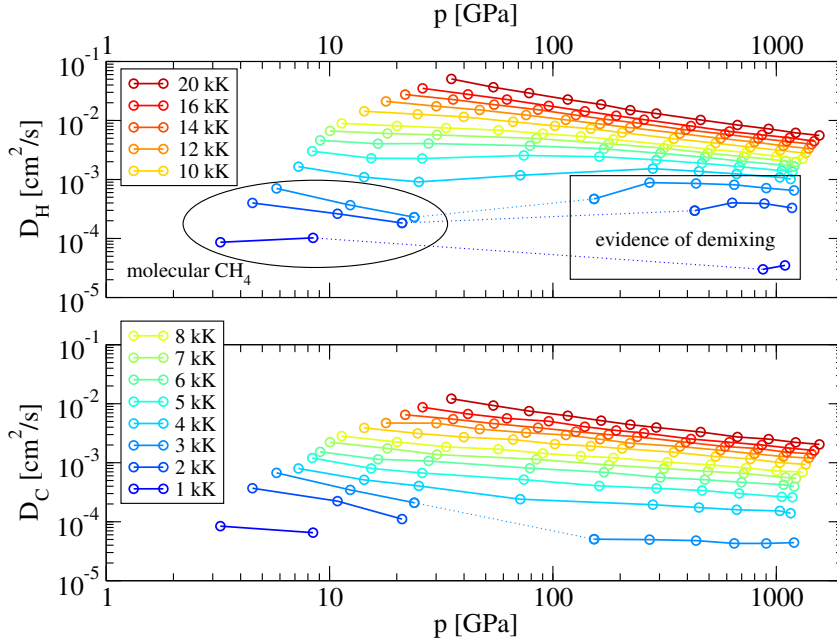


**Fig. 4.4.:** Diffusion coefficients of hydrogen (upper panel) and carbon (lower panel) over pressure along different isotherms between 1000 K and 20000 K.

### 4.3. Binary mixtures

The outlined results for ammonia and methane in conjunction with the thermodynamic data on water available in literature [47; 52] provide the basis for a systematic investigation of their binary and ternary mixtures. In this section the results on binary 1:1 mixtures are outlined, which are contained in paper II [185] and paper V [199]. Our first mixture study has been devoted to the water-ammonia mixture addressing the question whether there exist superionic mixtures. The consequent results have been published in Paper II [185].

To date, there is no generally accepted experimental proof of the existence of superionic phases at planetary conditions, although strong indications have been found for water [49] and ammonia [33]. The resolution of the underlying lattice of the heavy ions proved to be very challenging in those experiments making it necessary to use accompanying simulations to analyze the measured data. Commonly, cubic crystal structures are proposed for the underlying superionic lattice of water [50–52] and ammonia [33; 172]. Thereby, the fcc lattice has been discussed for H<sub>2</sub>O as well as NH<sub>3</sub>. Hence, an fcc lattice was chosen as starting structure in our simulations to investigate the phase diagram. These calculations yielded indeed hints for a superionic phase, but the underlying N-O lattice proved to be amorphous. This problem could be resolved by applying crystal structure prediction carried out with XtalOpt [189]. In appendix A, a comparison between the EOS based on the fcc structure and the one based on the structures from crystal structure prediction (CSP) is shown, see Fig. A.1.

CSP had been shown to be successful for pure water [40; 41; 43] and ammonia [55–57]. First simulations of water-ammonia mixtures at low pressures seemed promising and

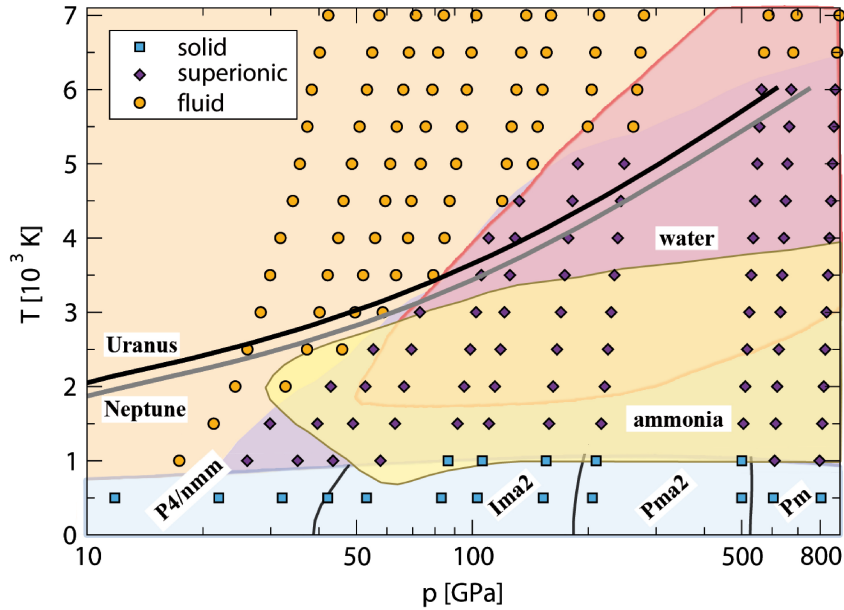


**Fig. 4.5.:** Phase diagram of the 1:1 water-ammonia mixture calculated in this work [185]. Each symbol represents a DFT-MD simulation. The region with the violet diamonds indicates the superionic 1:1 water-ammonia mixture, while superionic water [47] is illustrated in pink and superionic ammonia is yellow [172].

predicted a solid with space group  $P4/nmm$  to be favorable up to 12 GPa [66; 67]. This result was confirmed, and 3 further solid phases with space groups  $Ima2$ ,  $Pma2$ , and  $Pm$  were found up to 800 GPa. The respective cold curves including the zero-point motion energy were computed from phonon calculations employing Phonopy [194]. Heating up our predicted solid phases revealed superionic behavior between 1000 K and 6000 K. The resulting superionic water-ammonia phase covers roughly the same pressure-temperature range as the intersection of superionic water [47; 52] and superionic ammonia [172] as can be seen in Fig. 4.5. Furthermore, the diffusion coefficients have been calculated for this mixture, indicating that the diffusion coefficients of the individual species are well described by the respective values predicted for water [27] and ammonia [172].

Apart from the 1:1 water-ammonia phase diagram, we also studied the validity of the linear mixing approximation for the binary 1:1 EOS up to 20000 K and 1 TPa. The results are prepared for publication and are contained in the paper V in section 5.5. The thermal and caloric EOS for the three 1:1 mixtures of water, ammonia, and methane have been calculated and are shown in appendix A. The resulting data were interpolated using Akima splines for the pressure and linearly interpolated with respect to the temperature. The density and specific internal energy of the linear mixture have been calculated according to eq. (1.3) and eq. (1.4). The resulting deviations are shown in Fig. 4.6. Overall, we find the linear mixing model to agree very well with the real binary mixture data for the density, whereas we find moderate deviations for the internal energies. The largest density deviation of up to 4% was found for the water-methane mixture, while the specific internal energy deviates for some pressure-temperature conditions up to 4 kJ/g throughout all considered binary mixtures. Interestingly, the strongest internal

#### 4. Outline of the obtained results

energy deviations can be related to the pressure-temperature conditions at which superionic phases are predicted to occur. In case of the water-ammonia mixtures, we find a positive energy deviation for the conditions typical for superionic ammonia [172], while the deviation turns out to be slightly negative for superionic water [47]. In case of the other two binary mixtures, the superionic phases of ammonia and water induce again the biggest deviation between the energies of the linear and the real mixture. However, the observed indications of the demixing of methane might contribute as well below 4000 K. For the density deviations the picture is less clear. The maxima and minima in  $\Delta\rho$  can not be directly related to specific phases; they might even result from our interpolation using Akima splines. These third order polynoms can lead to an oscillatory behavior, when the underlying data are sparse and/or posses significant statistical fluctuations. This is supported by the fact that our data basis for water-ammonia is significantly larger compared to the other two mixtures, which show the strongest oscillations. Further interpolation and fitting procedures need to be investigated. However, we regard the discussed density deviation of up to 4% as upper limit.

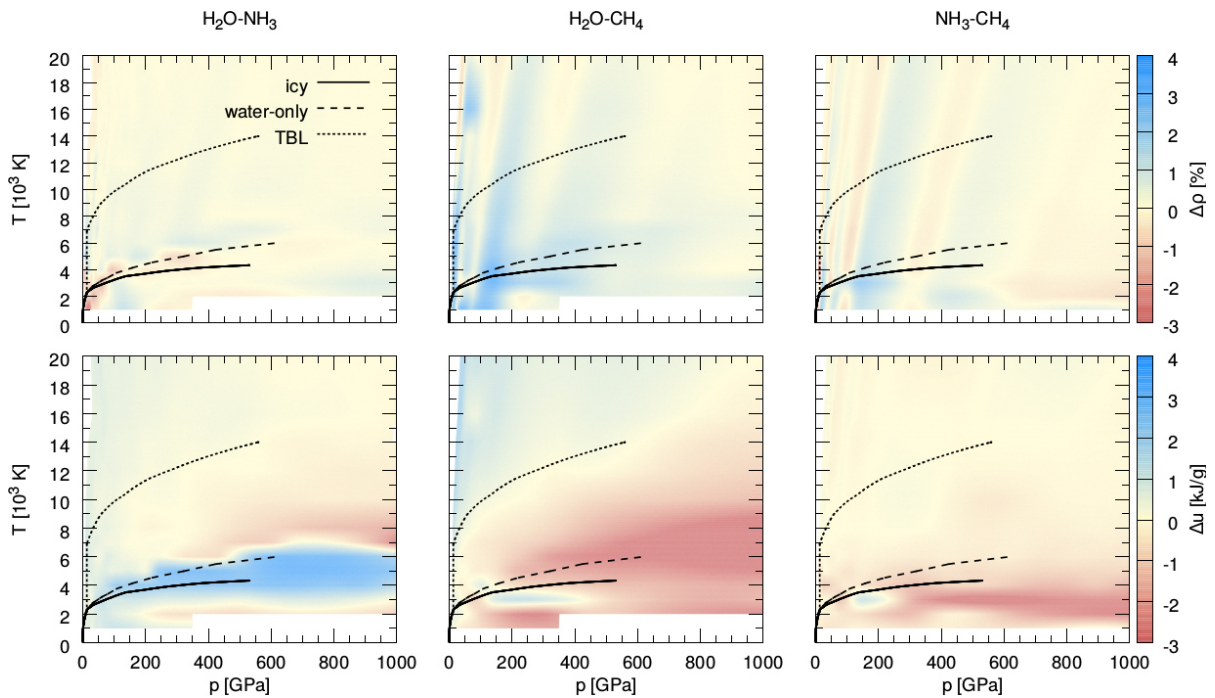


**Fig. 4.6.:** Deviations in density  $\Delta\rho$  (upper panels) and specific internal energy  $\Delta u$  (lower panels) of the real binary 1:1 mixtures from the linear mixing approximation [199]. Additionally, three prototypical profiles of Uranus, referred to as icy (solid line) [199], water-only (dashed line) [94], and thermal boundary layer (TBL, dotted line) [198], are shown in each plot. Details on the Uranus models are given in section 4.5.



## 4.4. Ternary mixtures

In this section we outline the results of the compositional effects for the ternary mixtures contained in paper III [184] as well as the verification of the linear mixing approximation for a chosen composition along three planetary profiles, contained in paper V. Prior to this work, only very sparse data existed on ternary mixtures composed of water, ammonia, and methane at high pressures. Most work on ternary mixtures at high pressures has been carried out for the so-called synthetic Uranus, which is characterized by a composition of 28:4:1:7 H-C-N-O. Thereby, isopropanol has been used as a replacement for methane [68; 177–179].

In order to identify general compositional trends in the EOS as well as the bonding behavior, we systematically studied six different ternary mixtures in collaboration with groups at the National Laboratories in Los Alamos and Livermore. The results are published in paper III [184] contained in section 5.3.

The compositions 1:1:1, 1:1:2, 1:1:3, 1:2:1, 1:3:1, 2:1:4 of methane-ammonia-water mixtures were chosen. Performing heating and cooling simulations, each mixture was started from arbitrary atomic positions at a representative density of  $3 \text{ g/cm}^3$ . Within the investigated temperature range between 2000 K and 10000 K, we find complex molecular structures, which are characterized by analyzing the bonding autocorrelation functions. At temperatures up to 4000 K we find amorphous structures composed of nitrogen and oxygen, while carbon forms short polymers. At the same time, the hydrogen ions form short-lived bonds and are very mobile compared to the heavy ions. Above 4000 K we find a dissociated fluid. This behavior does not depend on the composition of the mixture. However, we noticed that the oxygen content of the system has the most significant effect on the thermal EOS. As the oxygen content is increased, the pressure drops. The systematic variation of carbon and nitrogen at constant oxygen content influences the pressure only very little.

Among the considered concentrations the 2:1:4 methane-ammonia-water mixture reflects the solar abundances of C:N:O of 4:1:7 best, while being computationally feasible at the same time. Therefore this mixture was chosen for our further investigations along Uranus profiles, which are shown in Fig. 4.7. This work is part of paper V [199] in section 5.5. The considered three Uranus profiles are the same as in the previous section 4.3. For massive simulations containing 48 water, 24 methane, and 12 ammonia molecules, we calculated the EOS, structural properties and the diffusion coefficients along these pressure-temperature paths. In Fig. 4.7, we compare the linear mixing approximation and the considered real ternary mixture. We find a similar result as for the binary mixtures outlined in the previous section. The densities of the linear mixing approximation agree better than 3% with that of the real mixture, while we find stronger deviations for the specific internal energy of up to  $-3 \text{ kJ/g}$ . This internal energy deviation most likely results from the chemical bonding, which differs in the ternary mixture severely from the pure compounds. For example, we find strong CN bonds with lifetimes of roughly 120 fs at the conditions, which show the biggest deviations along the icy and water profiles. Additionally, we find the diffusion coefficients in the mixture to behave very similarly to those found in water [27], ammonia [172], and methane [199].

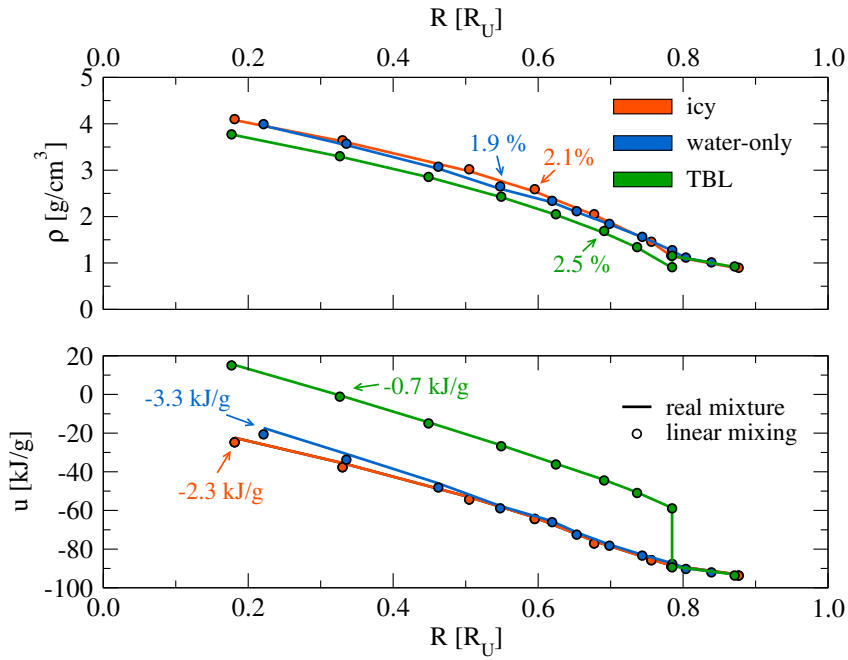


**Fig. 4.7.:** Density (a) and the specific internal energy (b) of the 2:1:4 methane-ammonia-water mixture for three possible radial Uranus interior profiles [94; 198; 199]. The real mixture (lines) is compared to the results obtained from the linear mixing approximation (filled circles) [199]. The presented numbers indicate the maximum deviation found for each planetary profile.

## 4.5. Implications for the interior structure of Uranus

Prior to this work, conventional interior structure models of Uranus contained water as the sole proxy for planetary ices [91; 94; 215], except for few conceptual studies [216; 217], which used simple analytic equations of state to include ammonia and methane. This work provides, for the first time, DFT-MD EOS for ammonia and methane, which cover the entire inner mantle region of Uranus for all state-of-the-art models. This allows the construction of interior models that are more realistic concerning the planet’s composition, which is assumed to agree with the solar abundances of the planetary ices. First models based on these new data sets have been calculated by Nettelmann and are contained in paper IV [198] and paper V [199], see section 5.4 and 5.5. Two exemplary models are shown in Fig 4.8. The icy interior structure model, contained in paper V, is the coldest published model with a core temperature of only 4300 K. It contains an inner mantle, which is almost entirely made of water, ammonia, and methane. Most of the water in this layer is present in the superionic phase [94], while the bulk of ammonia and methane are dissociated according to our findings outlined in sections 4.1 and 4.2. This model shows that it is indeed possible to find a solution, that allows for a very ice-rich interior. Nevertheless, this model is not able to reproduce the observed low present-day luminosity. On the other hand the model referred to as TBL, published in paper IV, is non-adiabatic and contains a thermal boundary layer resulting in a temperature jump from 2200 K to 6900 K between inner and outer mantle. This model is the hottest considered interior structure model and has a core temperature of



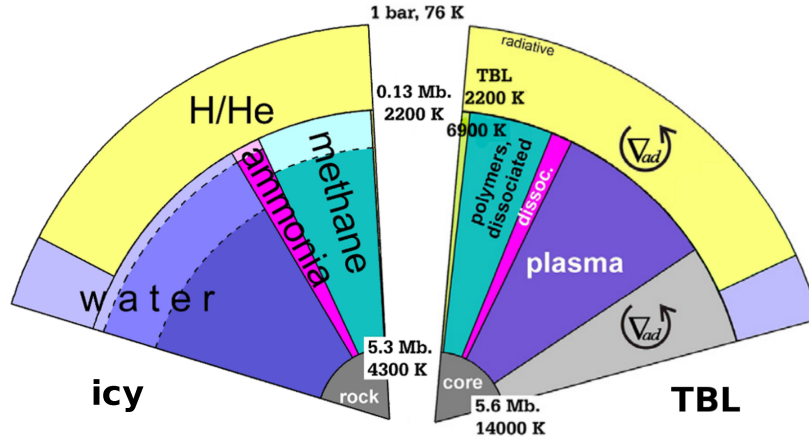


**Fig. 4.8.:** Uranus' interior structure models containing DFT-MD EOS for water, ammonia, and methane. The icy model, which is the coldest model investigated in this work, is shown on the left [199]. The hottest model, which contains a thermal boundary layer (TBL) is illustrated on the right [198]. The radial direction represents Uranus' internal radial distance from the center, while the angle scales with mass abundance of the individual components. Each color represents a different compound, whereas its variation in brightness reflects the underlying thermodynamic phase of the compound.

14000 K. Therefore, all planetary ices contained in the inner mantle are predicted to be present in the dissociated phase. Note, that the TBL is chosen such that the model matches the observed present-day luminosity. However, it contains a great amount of rocks inside the inner mantle in order to match the gravitational moments and the miscibility behavior of rocks with ice is unknown.

The consequent pressure-temperature profiles of the above interior structure models are shown alongside a widely-accepted Uranus adiabat without ammonia and methane [94] in Fig. 4.9. Note that the icy and the water isentrope rely on the same model assumptions except for the EOS. This illustrates directly the effect of the addition of ammonia and methane, which results in cooler planetary profiles for the ice-rich models. Such a model contains less hydrogen and helium in the inner mantle of Uranus compared to a water-only model. Since  $\text{H}_2\text{O}$ ,  $\text{NH}_3$ , and  $\text{CH}_4$  possess a higher heat capacity per mass than H and He, the entropy is increased, which has to be compensated by a lower temperature. Furthermore, Fig. 4.9 shows the superionic phases for water [47; 52] and ammonia [172] as well as the demixing region of methane discussed in section 4.2. According to our calculations there is no demixing of methane inside Uranus. Likewise, pure superionic ammonia is improbable to occur inside Uranus. However, our results for the mixtures indicate that there might exist superionic water-ammonia mixtures. There are also indications of carbon clustering in our simulations of water-methane and the ternary mixtures that might result from demixing of carbon in those mixtures, possibly at conditions relevant for Uranus' interior.

Moreover, the linear mixing approximation has been verified for the planetary ices based on the consistent DFT-MD EOS database as outlined in sections 4.3 and 4.4. Our findings suggest that the linear mixing approximation is sufficient for mixtures of ices under

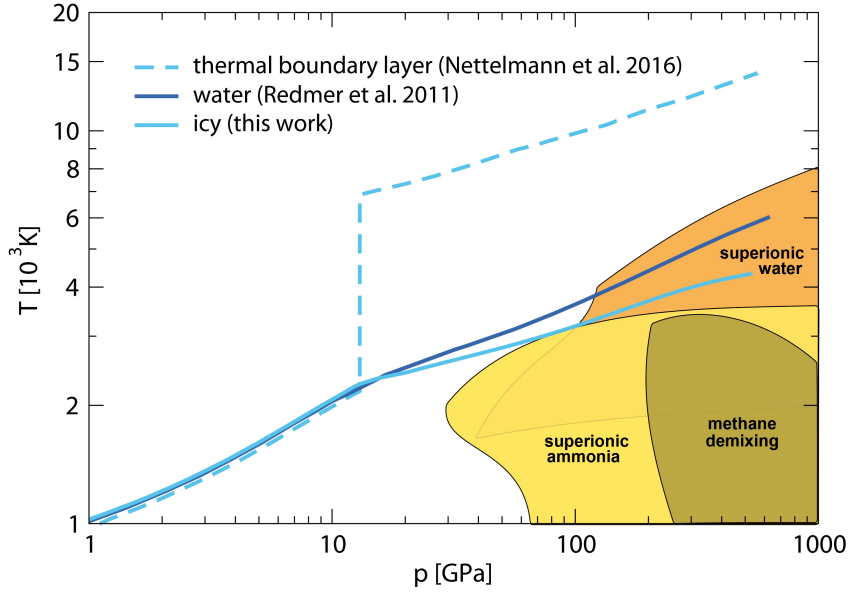


**Fig. 4.9.:** Uranus’ profiles of interior structure models for three limiting cases. The dark blue line indicates a typical adiabatic model containing water as single representative of molecular compounds [94]. The light blue lines show the most recent models including besides  $\text{H}_2\text{O}$  also  $\text{NH}_3$  and  $\text{CH}_4$ , which are illustrated in Fig. 4.8. Additionally, the demixing region of methane (green) as well as the superionic phases of water (orange) and ammonia (yellow) are presented in the graph.

planetary conditions, since the resulting EOS deviates only within the typically anticipated accuracy of the interior structure models. This complements the findings of other groups employing DFT-MD to verify the linear mixing approximation for hydrogen-helium mixtures [218] and the hydrogen-helium mixtures including heavier elements in the dilute limit [219].

Another promising result is our observed agreement of the self-diffusion coefficients in the real mixtures compared to the pure compounds as long as the underlying phases are not too different. Therefore, we conclude that the existing database on diffusion coefficients for water along with the calculated values for ammonia and methane in this work can be used as input for dynamo models.

## 4.6. Summary and outlook

In this work the thermodynamic, structural, and transport properties of complex H-C-N-O compounds at high pressures have been investigated using density functional theory molecular dynamics simulations. Thereby, pressures up to 1 TPa and temperatures up to 20000 K have been considered to cover the conditions predicted for the ice giant planets in the Solar System. Uranus and Neptune are prototypical for the supposedly large class of extrasolar ice-rich planets, since they are believed to contain vast amounts of water, ammonia, and methane. Hence, an accurate knowledge of the equations of state, phase diagrams, and transport properties of those materials as well as their mixtures is

required to understand the internal structure of ice giant planets. Here, the focus has been directed toward the EOS and phase diagrams of the pure compounds ammonia and methane, the properties of the binary and ternary mixtures and the verification of the linear mixing approximation.

Initially, we have investigated the characteristics of pure ammonia [172], proposing a new phase diagram, which includes a superionic phase. This phase is composed of an fcc lattice of nitrogen ions with highly mobile hydrogen ions. Moreover, for the first time an ammonia equation of state has been calculated in the warm dense matter regime including a quantum correction for the caloric EOS.

Additionally, a novel methane equation of state has been calculated, which agrees well with experimental Hugoniot data. Diffusion coefficients and radial distribution functions have been calculated to characterize the thermodynamic phases. Moreover, we propose a preliminary phase diagram including a demixing region, in collaboration with Hamel and Qi from the Lawrence Livermore National Laboratory.

On this foundation, we characterized the properties of the binary and ternary mixtures. Employing evolutionary crystal structure prediction, we propose a superionic phase in the 1:1 water-ammonia mixture [185]. Moreover, we investigated various concentrations for the ternary molecular mixture with special emphasis on the bonding and structural properties in collaboration with the National Laboratories in Los Alamos and Livermore. This investigation revealed that the EOS is strongly dependent on the oxygen content. Moreover, we could not identify a superionic phase in any ternary mixture, although we found an amorphous lattice with highly mobile hydrogen ions. It might be insightful to carry out further structure searching calculations for a selected set of water-ammonia-methane mixtures.

For the first time, DFT-MD equations of state for water, ammonia, and methane in the warm dense matter regime are available, enabling planetary models to go beyond the approximation of water as only representative of ices. Based on this new set of EOS, we investigated new possible interior structure models for Uranus [198; 199]. For several planetary profiles as well as for all three binary mixtures, the linear mixing approximation has been verified. Furthermore, the diffusion coefficients have been calculated for the binary and ternary mixtures and have been compared to those of the pure components. We conclude, that it should be possible to develop approximate rules for diffusion coefficients for arbitrary H-C-N-O mixtures.

Future work will be directed to an extensive investigation of transport and material properties. In particular, the isothermal compressibility, viscosity, and electronic transport properties, such as the electronic conductivity, should be computed. This would provide an extensive data set, which could be applied to interior structure models as well as dynamo simulations of ice giant planets [81; 92; 94]. A similar data set exists for the hydrogen-helium mixture [140], that is already successfully applied to simulations of Jupiter's dynamo [86; 220]. Additionally, a systematic study will hopefully enable us to develop mixing rules for transport properties in the warm dense matter region. The superionic phases should be treated with special caution regarding the viscosity.

Moreover, the demixing of methane and water-methane mixtures needs to be further investigated. In order to do so the entropy needs to be calculated, which can be done either by applying a two-phase model [221] or coupling constant integration [211], which

requires force matching [212; 213]. Details of computing the demixing region of planetary ices with DFT-MD are a matter of present investigation.

Finally, wide-range EOS for water, ammonia, and methane including the entropy need to be constructed to describe the entire evolution and present structure of ice giant planets in and beyond the Solar System. Similar EOS for hydrogen and helium for application to gas giant planets like Jupiter and Brown Dwarfs [103] already exist and have experienced broad interest in the community. Such improved wide-range data sets could provide the basis of more sophisticated planetary models, which would lead to a better understanding of the formation, interior structure, and evolution of giant planets.

## 5. Publications

This chapter comprises four peer-reviewed publications [172; 184; 185; 198] and one additional manuscript, which is in preparation for submission to *The Astrophysical Journal* [199]. The latter work is presented directly in this chapter, while the other four papers are available electronically at the journals' websites using the provided DOI information. Additionally, the contributions of the individual authors are listed for every manuscript.

## **5.1. Equation of state and phase diagram of ammonia at high pressures from ab initio simulations**

The Journal of Chemical Physics **138**, 234504 (2013).

DOI: 10.1063/1.4810883

### **M. Bethkenhagen**

Preparation of the manuscript, all calculations

### **M. French**

Preparation of the manuscript, initial idea for the quantum-correction of the EOS, provided tools to analyze the data

### **R. Redmer**

Supervision of the project, preparation of the manuscript

## 5.2. Superionic phases of the 1:1 water-ammonia mixture

The Journal of Physical Chemistry A **119**, 10582 (2015).

DOI: 10.1021/acs.jpca.5b07854

### **M. Bethkenhagen**

Preparation of the manuscript, crystal structure prediction at 0 K, phonon calculations (50%), heating calculations, and convergence tests

### **D. Cebulla**

Preparation of the manuscript, phonon calculations (50%), determination of the solid-solid phase transitions from the quasi-harmonic approximation

### **R. Redmer**

Preparation of the manuscript

### **S. Hamel**

Supervision of the project, initial idea to use crystal structure prediction, preparation of the manuscript

### **5.3. Bonding and structure in dense multi-component molecular mixtures**

The Journal of Chemical Physics **143**, 164513 (2015).

DOI: 10.1063/1.4934626

**E. R. Meyer**

Preparation of the manuscript, calculations including bonding analysis of the data, and fitting procedure (80%)

**C. Ticknor**

Preparation of the manuscript

**M. Bethkenhagen**

Preparation of the manuscript, initial test calculations, and computation of two additional isochors (20%)

**S. Hamel**

Preparation of the manuscript

**R. Redmer**

Preparation of the manuscript, initiated the collaboration

**J. D. Kress**

Preparation of the manuscript

**L. A. Collins**

Supervision of the project, preparation of the manuscript



## 5.4. Uranus evolution models with simple thermal boundary layers

Icarus **275**, 107 (2016).

DOI: 10.1016/j.icarus.2016.04.008

### **N. Nettelmann**

Preparation of the manuscript, implementation of the thermal boundary layer and most of the planetary calculations, extrapolation of equations of state

### **K. Wang**

Preparation of the manuscript, planetary models

### **J. J. Fortney**

Preparation of the manuscript

### **S. Hamel**

Preparation of the manuscript, calculation of methane equation of state

### **S. Yellamilli**

Preparation of the manuscript, planetary models

### **M. Bethkenhagen**

Calculation of ammonia data up to 10 Mbar and 10000 K on a rectangular grid, preparation of the manuscript

### **R. Redmer**

Supervision of the project, preparation of the manuscript

## **5.5. The linear mixing approximation for ices and its application to Uranus**

### **M. Bethkenhagen**

Preparation of the manuscript, recalculation and extension of methane EOS, extension of ammonia EOS up to 20000 K, computation of entire binary mixture data, calculations for ternary mixture along the isentrope (20%), calculation of diffusion coefficients

### **E. R. Meyer**

Preparation of the manuscript, calculations for ternary mixture along planetary profiles (80%)

### **S. Hamel**

Preparation of the manuscript, initial equation of state for methane up to 7000 K, and determination of methane demixing region

### **N. Nettelmann**

Preparation of the manuscript (especially the planetary part), computation of interior structure models

### **M. French**

Preparation of the manuscript, equation of state and diffusion coefficients of water

### **C. Ticknor**

Preparation of the manuscript

### **L. A. Collins**

Preparation of the manuscript

### **J. D. Kress**

Preparation of the manuscript

### **J. J. Fortney**

Preparation of the manuscript

### **R. Redmer**

Supervision of the project, preparation of the manuscript

DRAFT VERSION OCTOBER 27, 2016  
 Preprint typeset using L<sup>A</sup>T<sub>E</sub>X style emulatej v. 12/16/11

## THE LINEAR MIXING APPROXIMATION FOR ICES AND ITS APPLICATION TO URANUS

M. BETHKENHAGEN<sup>1</sup> AND E. R. MEYER<sup>2</sup> AND S. HAMEL<sup>3</sup> AND N. NETTELMANN<sup>1,4</sup> AND M. FRENCH<sup>1</sup> AND C. TICKNOR<sup>2</sup> AND L. A. COLLINS<sup>2</sup> AND J. D. KRESS<sup>2</sup> AND J. J. FORTNEY<sup>1</sup> AND R. REDMER<sup>1</sup>

*Draft version October 27, 2016*

### ABSTRACT

We investigate the validity of the widely used linear mixing (LM) approximation for the EOS of ices by computing 1:1 binary mixtures of methane, ammonia, and water, as well as their 2:1:4 ternary mixture at pressure-temperature conditions typical for the interior of the ice giant planets Uranus and Neptune. For that purpose we perform density functional theory molecular dynamics simulations using the VASP code. In particular, the LM approximation for equations of state is verified for the conditions present inside Uranus ranging up to 10 Mbar. We also calculate the diffusion coefficients for the ternary mixture along different Uranus interior profiles and compare them to the values of the pure compounds. We find that departures of the LM approximation from the real mixture are generally small; for the EOS they fall within about 4% uncertainty while for the diffusion coefficients within 20% uncertainty. In addition, we present a new ab initio EOS for methane. The ice EOS are applied to adiabatic models of Uranus. It turns out that a deep interior of almost pure ices is consistent with the gravity field data, in which case the planet becomes rather cold ( $T_{core} \sim 4500$  K).

*Subject headings:* Uranus; Neptune; Planetary Interiors; Planetary Evolution; Molecular Mixtures, Warm Dense Matter

### 1. INTRODUCTION

The interior of the giant planets Uranus and Neptune are believed to be rich in water, ammonia and methane. Many observable properties of this planet, such as luminosity, gravitational moments and magnetic field, are thought to be determined by the physical and chemical properties of their icy layer. Hence, the phase diagrams, equations of state and structural properties of these materials and their respective mixtures are of great interest. Over the last decades much effort has been put into the development of accurate equation of state data relevant for the interiors of the giant planets, foremost for hydrogen, helium, and water. Since the pioneering work of DeMarcus (DeMarcus 1958) and Peebles (Peebles 1964) models for giant planets employ the EOS data for different materials by mixing them linearly using the additive volume rule, i.e. by adding the volumina of the different materials at same pressure and temperature.

For hydrogen and helium, the validity of the linear mixing (LM) approximation has been tested in various studies. This was started by looking at analytic plasma models (Stevenson 1975) and later extended to DFT studies (Vorberger et al. 2007). (Wang et al. 2013) also investigated other mixing rules for the H-He mixture. Recently, (Soubiran & Militzer 2016) tested the LM approximation for the addition of heavy elements to a H-He mixture typical for Jupiter in the dilute limit.

There are two effects that might cause strong deviations of the linear mixing model from the behavior of the real mixture, demixing and phase transitions. For H-He for

instance, Vorberger et al. (2006) suggest that the LM approximation does not work well in the region of H-He phase separation. Methane and other hydrocarbons are thought to demix under the conditions present in Uranus (Hirai et al. 2009; Gao et al. 2010; Spanu et al. 2011; Lobanov et al. 2013). Water and ammonia are predicted to adopt different phases along the adiabats of Uranus and Neptune; in particular, water and ammonia possess a first-order transition to a superionic phase (Cavazzoni et al. 1999; Goncharov et al. 2005; Ninet et al. 2012) and even transitions within that phase (Wilson et al. 2013; French et al. 2016). One can thus suspect strong deviations between real and linear mixing behavior, at least in certain regions of the P-T space. However, for the ices the EOS data are sparse, and the validity of the LM approximation for molecular compounds has never been systematically checked. It is the purpose of this study to provide such a systematic study for the EOS as well as for the diffusion coefficients.

Using the method ab initio simulations, several real mixtures have already been investigated, such as the 1:1 water-ammonia mixture (Bethkenhagen et al. 2015), H/H<sub>2</sub>O (Soubiran & Militzer 2015), H-He with heavy element enrichment (Soubiran & Militzer 2016), and H-C-N-O mixture (Chau et al. 2011). There also exist a few experiments data for mixtures, most of them based on are shock compression experiments (EOS and electrical conductivity) (Radousky et al. 1990; Nellis et al. 1997) but their pressure range is limited to about 2 Mbar.

To select our  $P$ - $T$  range of interest we chose several different Uranus models: a typical water-rich Uranus model (Redmer et al. 2011) which is consistent with its observed gravity field but not with the low luminosity, and has a central temperature  $T_{core} \sim 6000$  K, then a rather warm ( $T_{core} \sim 14,000$  K) proposed Uranus model that was designed to fulfill both these constraints (Nettelmann et al. 2016); in addition, we construct a new

<sup>1</sup> Universität Rostock, Institut für Physik, D-18501 Rostock, Germany

<sup>2</sup> Theoretical Division, Los Alamos National Laboratory, Los Alamos, New Mexico 87545, USA

<sup>3</sup> Lawrence Livermore National Laboratory, Livermore, California 94550, USA

<sup>4</sup> Department of Astronomy and Astrophysics, University of California, Santa Cruz, CA 95064, USA

model, which is rather cold ( $T_{core} \sim 4500$  K), asking if the interior could be H-He free if made of a mixture of ices as found earlier (Podolak & Reynolds 1987).

This work is organized as follows. The computational method to calculate all the equations of state presented here is described in section 2. Section 3 presents our results for the linear mixing approximation for 3 binary mixtures and 1 ternary mixture, while section 4 deals with structural and ionic transport properties. In section 5 we will introduce a new ice-rich Uranus model, which serves as a lower bound in temperature compared to previous discussed models. Finally, our results are summarized in section 6.

## 2. EQUATIONS OF STATE (EOS) DATA

### 2.1. Density-Functional Theory Molecular Dynamics Simulations (DFT-MD)

The equation of state data were obtained from DFT-MD simulations performed with the Vienna Ab Initio Simulation Package (VASP) (Kresse & Hafner 1993a,b; Kresse & Furthmüller 1996; Hafner 2008). This approach is based on the Born-Oppenheimer approximation, which separates the electrons from the ions. The electrons are described via density functional theory (DFT) for finite temperatures (Hohenberg & Kohn 1964; Kohn & Sham 1965; Mermin 1965; Weinert & Davenport 1992; Wentz-covitch et al. 1992), while the ions are propagated as classical particles within the framework of molecular dynamics (MD). The ion temperature is controlled with a Nosé thermostat Nosé (1984). The interaction between electrons and ions is described by projector augmented wave (PAW) pseudopotentials (Blöchl 1994; Kresse & Joubert 1999). If not stated otherwise in the following section, a cutoff energy of 1000 eV, the hard pseudopotentials and a timestep of 0.25 fs was chosen. The simulation duration is typically 10 ps to 20 ps after the system was equilibrated. Furthermore, the Baldereschi Mean value point was used.

In the following we discuss the available EOS data in literature along with our calculations. The goal has been the calculation of EOS data on a grid covering temperatures up to 20000 K and pressures up to 1 TPa.

## 2.2. Pure ices: water, methane and ammonia

### 2.2.1. Water

The water data are based on the tabular EOS taken from (French et al. 2009), where the bulk of the simulations was carried out with 54 molecules, an energy cutoff of 900 eV and the Gamma point. For very small densities below  $1 \text{ g/cm}^3$  the particle number was reduced to 16 molecules. This data set was extended by adding some additional points from (French & Redmer 2015; French et al. 2016). These data contain the EOS of the ice phases VII and X as well as the superionic phases with a bcc and fcc lattice, respectively.

### 2.2.2. Ammonia

The ammonia data are taken from (Bethkenhagen et al. 2013) up to 10000 K and 330 GPa and have been extended up to 20000 K and 10 Mbar using 32 molecules. It is important to note that we switched the pseudopotential as the PAW radius is a lot smaller for the hard pseudopotentials. The data from (Bethkenhagen et al. 2013)

were not explicitly corrected for the new pseudopotential, since test calculations showed that both potentials agreed to better than 1% and 0.5 kJ/g up to 10000 K and 330 GPa. This uncertainty is considered to be within the anticipated errors of planetary interior structure models. Moreover, we reduced the timestep from 0.5 fs to 0.25 fs, since the dissociated fluid, which is formed at high temperature, is characterized by short-lived bonds. They are only be correctly described as the timestep is sufficiently small.

### 2.2.3. Methane

The methane EOS has been completely recalculated, since the previously published EOS by (Sherman et al. 2012) does not cover the entire region required for our investigation. We simulated 54 molecules in the simulation box, which were placed initially on a bcc lattice for every simulation run. The resulting thermal EOS is shown in Fig. 1 along with the data published by (Sherman et al. 2012). Our data typically agree within 2% in pressure and within 1 kJ/g in specific internal energy compared to the data by (Sherman et al. 2012). However, in the melting as well as the dissociation region, we find more significant deviations of up to 4%, which results from a hysteresis effect. Performing heating and cooling calculations in both region, we find different molecular forms. In particular, we find polymers in some region of the considered pressure-temperature conditions. These effects will be discussed separately by (Qi et al. 2015). That work will also present a novel phase diagram of methane including a prediction of the demixing region.

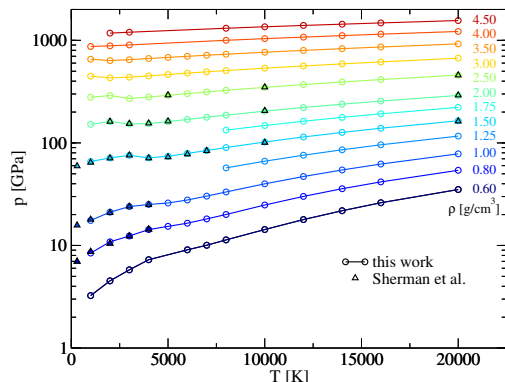


FIG. 1.— Pressure over temperature of methane along isochors (colored lines with circles) in comparison to the thermal EOS by (Sherman et al. 2012) (colored triangles).

## 2.3. Binary mixtures

The equations of state for the binary 1:1 mixtures, water-methane and ammonia-methane, have been entirely calculated in this work. However, the 1:1 water-ammonia data are based on (Bethkenhagen et al. 2015) and are extended toward higher temperatures as well as lower densities. That EOS has been calculated using 32 molecules and the Monkhorst-Pack  $2 \times 2 \times 2$  set, whereas the other two mixtures have been calculated with 54 molecules on an initial bcc lattice. The simulations for the binary mixtures have been carried out on the same temperature grid as already existed for the pure compounds

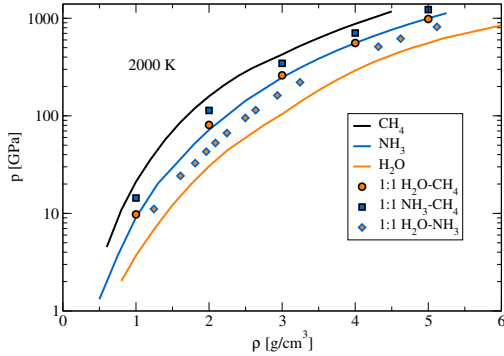


FIG. 2.— Pressure of the pure compounds (lines), water (orange), ammonia (blue), and methane (black), as well as of the binary 1:1 mixtures plotted over density at 2000 K.

(1000 K – 8000 K: 1000 K steps, 10000 K – 16000 K: 2000 K steps, 20000 K). Each isotherm contains at least five density points.

In Fig. 2, exemplary isotherms for each binary mixture as well as the pure compounds are shown at 2000 K. As expected the binary mixtures behave very systematic compared to water, ammonia, and methane. For the shown isotherms of ammonia and the 1:1 water-methane mixture, the pressure agrees to within 6%. This suggests, that one can possibly neglect one of those EOS.

#### 2.4. 2:1:4 methane-ammonia-water mixture

Prior to this work an extensive study has been performed on different concentrations for this mixtures in order to gain an insight on the properties of those mixtures (Meyer et al. 2015). We chose the 2:1:4 mixture for this study, since it provides a good compromise between computational effort and resemblance to the solar abundances 4:1:7 of water, methane and ammonia. We simulated mixture containing 48 water, 24 methane and 12 ammonia molecules along the three planetary profiles discussed in this work. For the small pressures up to 40 GPa the reciprocal space was sampled at the Baldereschi Mean value point, while for higher pressures the Monkhorst-Pack 2x2x2 set was used. Each simulation run was started from a density resembling that of the linear mixing approximation. After about 1000 timesteps the pressure was checked and the volume of the simulation box adapted until the desired pressure was matched up to a deviation of 2% from the planetary profile’s value. Since this procedure is very computationally expensive for the smallest desired pressures, we typically chose two different volumes and interpolated linearly between the resulting pressures.

### 3. LINEAR MIXING APPROXIMATION

The linear mixing approximation is very simple and reads as follows for density  $\varrho$  and internal energy  $u$  (DeMarcus 1958; Peebles 1964):

$$\frac{1}{\varrho(p, T)} = \sum_{i=1}^N \frac{X_i}{\varrho_i(p, T)}, \quad (1)$$

$$u(p, T) = \sum_{i=1}^N X_i u_i(p, T). \quad (2)$$

In the above equation,  $X_i$  represents the mass fraction, which is defined as mass of particle type  $i$  divided by the total mass.

The EOS described in the previous section are interpolated using Akima splines for the pressures and are linearly interpolated on a temperature grid. The deviations in density  $\Delta\varrho(p, T)$  and internal energy  $\Delta u(p, T)$  are defined as

$$\Delta\varrho(p, T) = \frac{\varrho_{LM}(p, T) - \varrho_{real}(p, T)}{\varrho_{real}(p, T)}, \quad (3)$$

$$\Delta u(p, T) = u_{LM}(p, T) - u_{real}(p, T). \quad (4)$$

#### 3.1. Binary Mixtures

For the comparison of the real binary mixtures to the linear mixing approximation, all data were interpolated onto a rectangular pressure-temperature grid. The results for the comparison of real mixture to the linear mixing approximation are shown in Fig. 3. The planetary profiles shown in this figure are chosen such to represent the range of currently available Uranus profiles. The details of the underlying models are explained in section 5. The pressure deviation amounts solely between -3% and 4%. The specific internal energy of the real mixtures deviates between -3 kJ/g and 4 kJ/g. Note, that the reference point of all binary mixtures was chosen at 1000 GPa 20000 K, where the internal energy was set to zero. Interestingly, the strongest internal energy deviations can be related to the pressure-temperature conditions at which superionic phases are predicted to occur. In case of the water-ammonia mixtures, we find a positive energy deviation for the conditions typical for superionic ammonia Bethkenhagen et al. (2013), while the deviation turns out to be slightly negative for superionic water French et al. (2009). In case of the other two binary mixture, the superionic phases of ammonia and water induce again the biggest deviation between the energies of the linear and the real mixture. A signal, which might be due to the demixing of methane can not be clearly identified, however, it might be masked by the effect of the superionic phases of water and ammonia. For the density deviations the picture is less clear. The maxima and minima in  $\Delta\rho$  can not be directly related to specific phases, on the contrary they might even result from our interpolation using Akima splines. These third order polynomials can lead to an oscillatory behavior, when the underlying data are sparse and/or possess significant statistical fluctuations. This is supported by the fact that our data basis for water-ammonia is significantly larger compared to the other two mixtures, which show the biggest oscillations. Therefore, we regard the discussed density deviation of up to 4% as upper limit and further interpolation and fitting procedures need to be investigated.

#### 3.2. Ternary Mixture

The results for the ternary 2:1:4 mixture along the three considered planetary profiles are shown in Fig. 4. We find a similar result as for the binary mixtures outlined in the previous section. The maximum deviations amount up to 2.5% along the TBL planetary profile and -3.3 kJ/g for the water isentrope. Note that the reference point of the ternary mixture was differently chosen

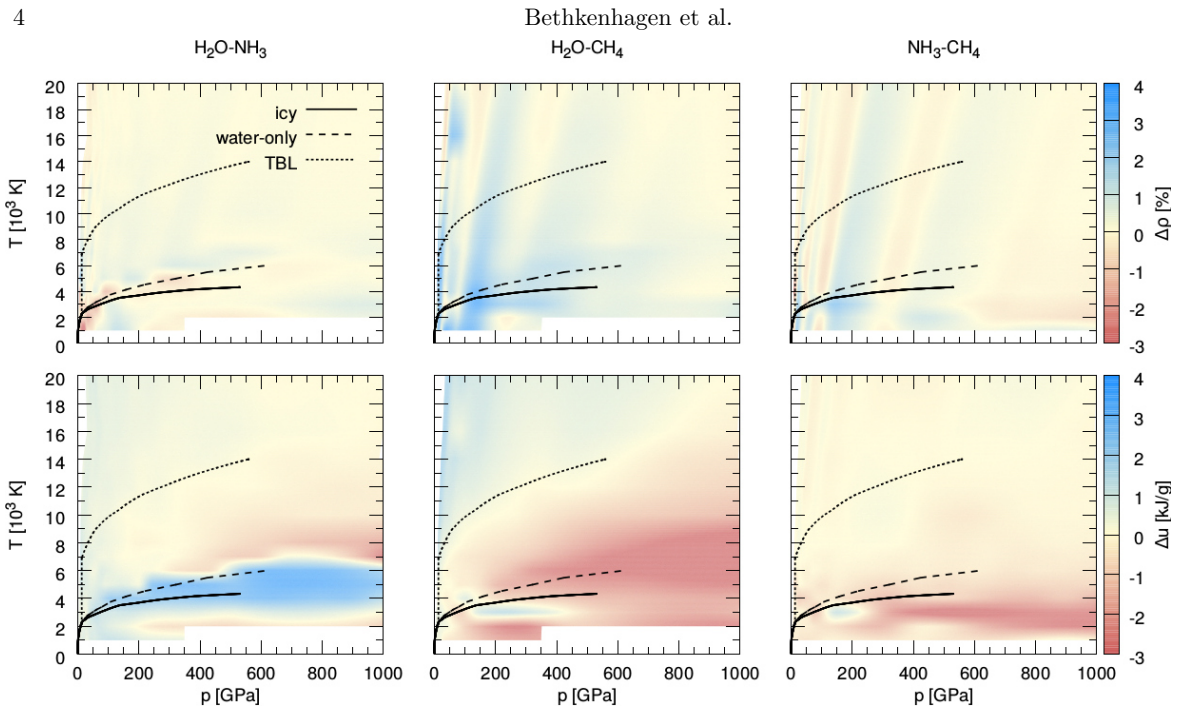


FIG. 3.— Deviation of densities (upper panels) and internal energies (lower panels) of the considered real binary 1:1 mixtures from the linear mixing approximation. The  $\text{H}_2\text{O}-\text{NH}_3$  (left),  $\text{H}_2\text{O}-\text{CH}_4$  (middle), and  $\text{NH}_3-\text{CH}_4$  (right). All values are within a magnitude of 5%. For reference, the isentrope assuming pure water (Nettelmann et al. 2013) as well as the one from this work are shown in orange.

to 14000 K and 560 GPa, the end point of the TBL planetary profile. The internal energy deviation most likely

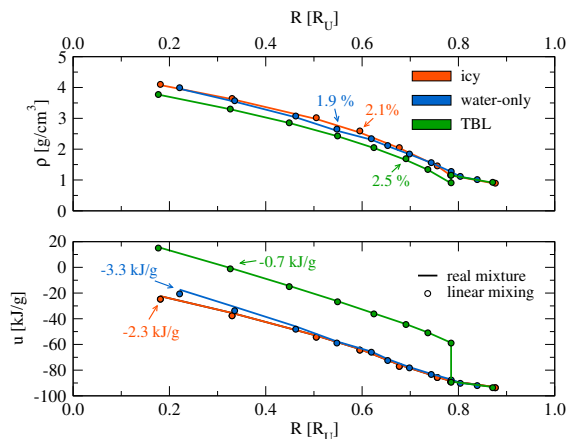


FIG. 4.— Deviations of density (upper panel) and specific internal energy (lower panel) between the real 2:1:4 methane-ammonia-water mixture (solid lines) and the linear mixing model (circles) along the three discussed planetary profiles of Uranus. the maximum deviations along each planetary profile are given as colored numbers.

results from the chemical bonding, which is subject to the next section.

#### 4. STRUCTURE AND DIFFUSION COEFFICIENTS

In this section we characterize the nature of bonding found in the binary and ternary mixtures. We consider only ionic properties, electronic properties are left out for future work.

##### 4.1. Pair distribution functions and chemical bonds

Given that the linear mixing approximation works within 4% in pressure and 4 kJ/g in specific internal energy, the system must not distinguish too much between the heavy atoms. However, if chemistry between, for example, C and N begins to occur in the simulation then we would start to see deviations from LM. The largest deviations in Fig. 4 occur around  $T = 4500$  K. To see if reactions occur, we plot in Fig. 5 the  $g(r)$ , the pair correlation function (PCF), for CN for a select few of the EOS points in Fig. 4. The deviation from the molecular LM model appears attributable to the interaction between C and N. The emergence of molecular bonding is rapid as the  $P$  and  $T$  are increased. While not as strong a peak as the hydrogen bonds, this indicates that CN complexes, whether diatomic or polyatomic in nature, are forming in the system.

To understand the strength of the CN bonding, we performed a bond autocorrelation function (BACF) analysis which predicts the likelihood that a bond which forms at  $t = 0$  exists a time  $t$  later. We followed the methodology outlined in (Meyer et al. 2015). Our  $r_{\text{cut}}$  was chosen from the  $g(r)$  where the value of the molecular peak was most distinguished from the first valley. For the  $T \leq 3125$  K, the CN complex does not form. Once the system is hot enough for H atoms to dislodge from their heavy partners, the C and N can find each other to form complexes with lifetimes around  $\tau^* \approx 120$  fs. Lifetimes were calculated in the same manner as in (Meyer et al. 2015).



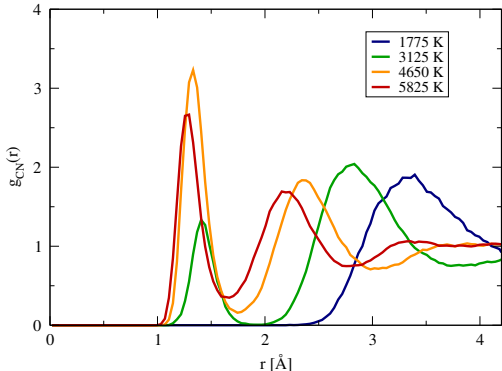


FIG. 5.— Pair correlation functions for CN. As temperature increases CN develops a molecular peak indicating interactions between C and N and that CN chemistry is occurring. This changes the density landscape of the linear mixing model.

#### 4.2. Diffusion Coefficients

The diffusion coefficient  $D_\alpha$  has been calculated for each species  $\alpha$  using the velocity autocorrelation function

$$D_\alpha = \lim_{t \rightarrow \infty} \frac{1}{3} \int_0^t \sum_i \langle v_{i,\alpha}(0) \cdot v_{i,\alpha}(\tau) \rangle d\tau. \quad (5)$$

We calculated the diffusion coefficients for methane and for the full 2:1:4 mixture along the planetary profiles. The value for water are taken from (French et al. 2010), while the values for ammonia are taken from (Bethkenhagen et al. 2013). The results are shown in Fig. 6. In general the diffusion coefficients in the ternary mixture agree very well compared to those in the pure compounds. Typically, we find them typically to agree within 20%, which is a satisfactory result, given that the uncertainty is usually 10%. The most significant deviations are found for the areas, which are characterized by phase transition, e.g., in the demixing region in methane and the superionic phase of water. For those phases, the diffusion coefficients of the heavy particles vanishes for the heavy ions within water and ammonia. At the same time, we obtain values typical for a fluid phase in the ternary mixture, where we do not find those phases.

### 5. PLANETARY MODELS

#### 5.1. Why we compute a new Uranus model

The bulk composition and the internal composition distribution of Uranus and Neptune are important topics of investigation. They bear crucial information on our understanding of giant planet formation and subsequent evolution, as well as of the conditions in the solar nebula from which they emerged.

An important hint on the bulk composition of Uranus comes from its mean density, which is close to that of liquid water. Indeed, the elements OCN are believed to be abundant in Uranus. In the hydrogen-rich troposphere, they chemically favor the supercritical fluid phases of water, methane, and ammonia, while under conditions at the time of formation the low-pressure ices phases of these molecules were likely to prevail in the protoplanet (Podolak & Reynolds 1984). Uranus' gravity field indicates a significantly denser deep interior than the outer envelope with a separation at about 10 GPa, while the

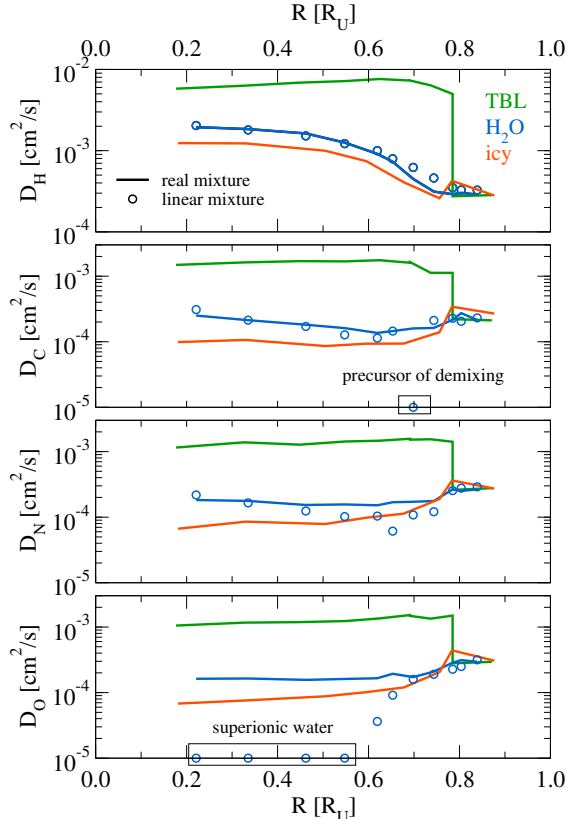


FIG. 6.— The self-diffusion coefficients of the constituents H, C, N, and O in the real mixture (solid lines) along the planetary profiles as a function of Uranus' radius. Diffusion coefficients marked by an orange box are artificial and just mark the demixing/polymerization region of methane and the superionic regime, where the respective diffusion coefficients vanish. The open circles indicate the diffusion coefficients in the pure compounds shown here exemplary for the water-only isentrope.

magnetic field can be explained by convective motions in a conducting deep-seated shell. No theory of giant planet formation, evolution, and planet structure exists that can consistently explain these observations. Therefore, it is important to explore a wide variety of planet structure and formation models in order to achieve a consistent view, that eventually enables to infer the properties of the early solar system.

Uranus and Neptune are often modeled under the assumption of few layers, in which rocks are confined to the core and heavy elements in the envelopes assumed to be mostly C-N-O-S (Podolak & Reynolds 1987; Podolak et al. 1991; Hubbard et al. 1995; Nettelmann et al. 2013). Furthermore, CNOS bearing molecules in giant planets have sometimes been represented by water EOSs (Helled et al. 2011; Nettelmann et al. 2013; see Redmer et al. 2011 for an illustration). Such state-of-the-art models typically predict an inner envelope ice mass fractions of  $\sim 0.9$  for Uranus, and high ice-to-rock ratios (I:R) of  $\sim 10 \times$  solar. It is noteworthy that entirely different suites of Uranus models which assume smooth density distribution throughout the interior (Helled et al. 2011) or are based on random interior structure search for acceptable density distributions (Podolak et al. 2000), yield

similar ice mass fractions. For Neptune, the situation is less clear due to the higher observational uncertainty in the gravitational moment  $J_4$  (Nettelmann et al. 2013).

Of particular interest to this work are the Uranus models by (Podolak & Reynolds 1987). These authors applied linearly mixed EOSs for the ices  $\text{H}_2\text{O}$ ,  $\text{CH}_4$ ,  $\text{NH}_3$  and  $\text{H}_2\text{S}$  based on Thomas-Fermi-Dirac theory for dense matter, and an interpolation to ideal gas region at the low pressures. In addition, they took into account the influence of condensation on the temperature profile in the outer envelope. As a result, it was found that the observed rotation rate and gravitational harmonics can only be reproduced by the models if the ice shell below the H-He rich outer envelope is so extended that the total I:R ratio amounts to high values of 16–36, i.e., about 6–14 $\times$  solar. However, supersolar I:R ratio have been deemed unrealistically, for rocks condense at higher temperatures and thus a larger fraction of rocks should be confined to planetesimals than in case of the ices (Podolak & Reynolds 1984; Hubbard & Marley 1989). On the other hand, the capture radius of the protoplanet may be larger for ice-rich than for rock-rich planetesimals, perhaps leading naturally to an ice-rich envelope above a rock-rich planet center (Podolak & Reynolds 1987).

Here we apply linearly mixed EOSs for  $\text{H}_2\text{O}$ ,  $\text{CH}_4$ , and  $\text{NH}_3$  in solar portions to represent ices in the deep interior of Uranus, and compute the first Uranus model based on ab initio EOSs for the light ices. As in standard few-layer models, we assume for simplicity an adiabatic interior and confine rocks to the core. Our models are a step forward from those of (Nettelmann et al. 2013), who considered only water as a representative of ices in the deep interior. Of course, the interior of Uranus may be far complexer than modeled here. In particular, non-adiabatic regions and significant amounts of rocks and of H-He in the deep interior can not be excluded. However, the mixing behavior of rocky materials ( $\text{MgO}$ ,  $\text{SiO}_2$ ,  $\text{FeS}$ ,  $\text{FeO}$ ) with ices and H-He is poorly understood yet. First results indicate demixing between  $\text{MgO}$  and hydrogen under Saturn core conditions (Wilson & Militzer 2013) suggesting segregation of rocks to the center in the even colder Uranus, as assumed here.

### 5.2. Results: Icy Uranus structure models

For our icy Uranus structure model we assume a simple three-layer structure with an isothermal core and two adiabatic, homogeneous envelopes that differ in their abundance of ices. The precise ice abundance ratios in the planet are not known. For the inner envelope (layer No. 2), we assume protosolar abundance ratios for O:C:N, which corresponds to mass fractions of  $Z_{\text{H}_2\text{O}}^{(2)} = 0.61$ ,  $Z_{\text{CH}_4}^{(2)} = 0.31$  and  $Z_{\text{NH}_3}^{(2)} = 0.08$ . In the outer envelope, ices are represented by the water EOS. The unknown ice mass fractions in the two envelopes,  $Z^{(1)}$  and  $Z^{(2)}$  are used to adjust the two measured gravitational moments  $J_2$  and  $J_4$ . At the assumed sharp transition between outer and inner envelope density and entropy change discontinuously while  $P$  and  $T$  change continuously. The transition pressure  $P_{1-2}$  is then a variable parameter, but we find acceptable icy Uranus models only for  $P_{1-2} \sim 13$  GPa. Details of our modeling procedure are described in (Redmer et al. 2011; Nettelmann et al. 2013).

Under conditions of  $T \gtrsim 3000$  K and  $\gtrsim 10$  GPa as in the deep interior of Uranus, experimentally compressed methane has been found to separate into hydrogen and diamond (Hirai et al. 2009). At present it is not clear whether diamond formation also occurs in mixtures of ices, and if it would sink to the center. To account for the uncertainty of possible diamond formation and sinking, we compute two different structure models. In our Uranus model *U15-1* we neglect possible diamond formation. Methane is then assumed to remain miscible in water and ammonia. In our Uranus model *U15-2* we account for possible diamond sedimentation by using a diamond EOS (Correa et al. 2008) for the core material. As size of the core is determined by total planet mass conservation (Redmer et al. 2011; Nettelmann et al. 2013), which typically yields small ( $\sim 1M_{\oplus}$ ) cores for Uranus, the resulting diamond core mass is lower than the total amount of available carbon. Therefore, the inner envelope composition must include some methane in order to conserve the solar O:C ratio. In addition, the inner envelope contains the excess hydrogen from the dissociated methane, in the amount corresponding to the central diamond core mass.

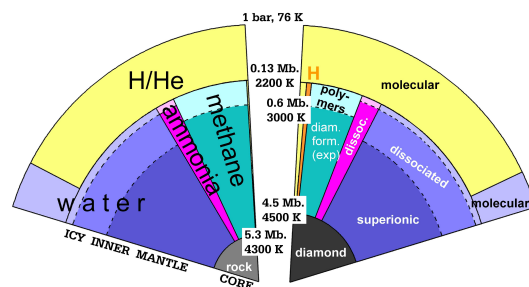


FIG. 7.— Two icy Uranus structure models with three homogeneous layers, separated by *solid* azimuthal lines. The radial direction scales linearly with planet internal radial distance from the center, while the angle scales with mass abundance of the single components. The *left* models shows our rock core model U15-1, while the *right* one the diamond core model U15-2. *Dashed* lines indicate phase boundaries of the single component EOS as labeled in the *right* panel, according to (Redmer et al. 2011) for water, (Bethkenhagen et al. 2013) for ammonia, and (Hirai et al. 2009) for methane. The slim *orange* stripe shows the hydrogen fraction that belongs to the sedimented diamond.

Figure 7 illustrates these two models. Both models have low outer envelope ice mass fractions of respectively 15% and 12%, consistent with the models of (Nettelmann et al. 2013). While in those earlier models the water EOS was also taken representative of all ices in the inner envelope, with the result of about 0.9 water and 0.1 H-He by mass there, the ice mass fraction in our present models increases to respectively 0.994 and 0.975. This is because the lower the mean atomic weight of the heavy elements, the larger their abundances in order to conserve the mean mass density. We therefore also obtain a larger and more massive core masses for our diamond core model compared to rock core models. On particular, the diamond core mass of  $1.2 M_{\oplus}$  implies 2% of excess



hydrogen in the inner envelope (orange colored in Fig. 7). Our icy Uranus models are pretty cold, with core temperatures of about 4500 K only. This is a result of the low H-He mass fraction.

We also note that the deep internal H-He mass fraction becomes very small. While its value is not strictly constrained by formation models, those predict the simultaneous accretion of gaseous H-He and planetesimals by the protoplanet before run-away gas accretion sets in (Pollack et al. 1996; Mordasini et al. 2012). Our resulting low deep internal H-He mass fraction might indicate escape of initially accreted H-He into the outer envelope.

As expected, the overall I:R ratio of our icy Uranus models turns out to be large, i.e. 19 for rocky core model U15-1 and infinite for the other one. Models with such high I:R ratios (Podolak & Reynolds 1987) have been judged no realistic representation of the internal structure of Uranus (Hubbard & Marley 1989). We agree with that possible conclusion regarding our models, albeit for a different reason. The predicted present-day luminosity of icy, adiabatic, quasi-homogeneous Uranus models has been repeatedly shown to exceed the observed one (Hubbard et al. 1995; Nettelmann et al. 2013). This faintness-problem of Uranus' provides evidence for a more complex internal structure than modeled here, in particular to a largely superadiabatic interior (Hubbard et al. 1995; Nettelmann et al. 2013). Our models show —an important result of this work— that in that case the deep interior *must* contain elements heavier than ices in order to conserve the mean density. Therefore, a superadiabatic interior will tend to decrease the I:R ratio compared to the values obtained here. Moreover, a superadiabatic interior for Uranus implies mixing of rocks with ices to some degree. Once rocks are allowed for in the deep interior, the maximum possible H-He mass fraction in the deep interior increases as well (Helled et al. 2011), which may be even more consistent with core planet formation models. Icy Uranus models with superadiabatic deep interior have been subject to separate work (Nettelmann et al. 2016).

## 6. CONCLUSIONS

Overall, we find the linear mixing approximation to perform very well for the molecular compounds, water, ammonia, and methane, inside the mantle of Uranus on the

basis of the EOS investigated here. For the binary 1:1 mixtures, which have been computed on a grid for pressures up to 10 Mbar and temperatures up to 20000 K, we find a maximum density deviation of 4%. At the same time, the density deviation of the ternary mixture along the three considered Uranus profiles is even smaller deviating at most 3%. Hence, it is not necessary to construct a broad variety of EOS, instead we suggest to construct wide-range EOS for the pure substances water, ammonia, and methane.

However, in terms of investigating the underlying phase diagrams it is very interesting to study the mixtures. For example, the existence of a superionic phase in the presence of methane is still unclear.

The diffusion coefficients for the individual compounds in the mixture agree with the pure values as long as the same phase is present. Apart from the diffusion coefficients, one should calculate the viscosity, which is a very insightful property. Furthermore, the electronic transport properties are of great interest as input for dynamo simulations. It would be desirable to have a complete set of transport and thermodynamic transport properties along the discussed planetary profiles like the data set available for the hydrogen-helium mixtures along the Jupiter adiabat (French et al. 2012).

## ACKNOWLEDGMENT

We thank R. Helled, M. Podolak, C. Kellermann and M. Schöttler for insightful discussions. Moreover, we especially thank A. Becker for providing valuable hints and a tabulated form of the diamond EOS.

MB, NN, MF and RR gratefully acknowledge support from the Deutsche Forschungsgemeinschaft SFB 652 and computational power provided by the ITMZ of the University of Rostock as well as the HLRN. ERM, CT, JDK, and LAC gratefully acknowledge support from the Advanced Simulation and Computing Program (ASC), science campaigns 1 and 4, and LANL which is operated by LANS, LLC for the NNSA of the U.S. DOE under Contract No. DE-AC52-06NA25396. SH acknowledges support by the U.S. Department of Energy at the Lawrence Livermore National Laboratory under Contract No. DE-AC52-07NA27344 and by the NASA Outer Planet Research program (grant no. NNH12AU44I).

## REFERENCES

- Bethkenhagen, M., Cebulla, D., Redmer, R., & Hamel, S. 2015, *Journal of Physical Chemistry A*, 119, 10582
- Bethkenhagen, M., French, M., & Redmer, R. 2013, *The Journal of Chemical Physics*, 138, 234504
- Blöchl, P. E. 1994, *Phys. Rev. B*, 50, 17953
- Cavazzoni, C., Chiarotti, G. L., Scandolo, S., Tosatti, E., Bernasconi, M., & Parrinello, M. 1999, *Science*, 283, 44
- Chau, R., Hamel, S., & Nellis, W. J. 2011, *Nature Communications*, 2, 203
- Correa, A. A., Benedict, L. X., Young, D. A., Schwegler, E., & Bonev, S. A. 2008, *Physical Review B*, 78, 024101
- DeMarcus, W. 1958, *The Astronomical Journal*, 63, 2
- French, M., Becker, A., Lorenzen, W., Nettelmann, N., Bethkenhagen, M., Wicht, J., & Redmer, R. 2012, *Astrophysical Journal Supplement Series*, 202, 5
- French, M., Desjarlais, M. P., & Redmer, R. 2016, *Physical Review E*, 93, 022140
- French, M., Mattsson, T. R., Nettelmann, N., & Redmer, R. 2009, *Physical Review B*, 79, 054107
- French, M., Mattsson, T. R., & Redmer, R. 2010, *Physical Review B*, 82, 174108
- French, M., & Redmer, R. 2015, *Physical Review B*, 91, 014308
- Gao, G. Y., Oganov, A. R., Ma, Y. M., Wang, H., Li, P. F., Li, Y. W., Iitaka, T., & Zou, G. T. 2010, *The Journal of Chemical Physics*, 133, 144508
- Goncharov, A. F., Goldman, N., Fried, L. E., Crowhurst, J. C., Kuo, I.-F. W., Mundy, C. J., & Zaug, J. M. 2005, *Physical Review Letters*, 94, 125508
- Hafner, J. 2008, *J. Comput. Chem.*, 29, 2044
- Helled, R., Anderson, J., Podolak, M., & Schubert, G. 2011, *Astrophys. J.*, 726, A15
- Hirai, H., Konagai, K., Kawamura, T., Yamamoto, Y., & Yagi, T. 2009, *Physics of the Earth and Planetary Interiors*, 174, 242
- Hohenberg, P., & Kohn, W. 1964, *Phys. Rev.*, 136, B864
- Hubbard, W. B., & Marley, M. S. 1989, *Icarus*, 78, 102
- Hubbard, W. B., Podolak, M., & Stevenson, D. J. 1995, in *Neptune and Triton*, ed. Cruikshank (University of Arizona, Tucson), 109–138
- Kohn, W., & Sham, L. J. 1965, *Phys. Rev.*, 140, A1133
- Kresse, G., & Furthmüller, J. 1996, *Phys. Rev. B*, 54, 11169
- Kresse, G., & Hafner, J. 1993a, *Physical Review B*, 47, 558
- . 1993b, *Physical Review B*, 48, 13115
- Kresse, G., & Joubert, D. 1999, *Physical Review B*, 59, 1758

- Lobanov, S. S., Chen, P.-N., Chen, X.-J., Zha, C.-S., Litasov, K. D., Mao, H.-K., & Goncharov, A. F. 2013, *Nature Communications*, 4, 2446
- Mermin, N. D. 1965, *Phys. Rev.*, 137, A1441
- Meyer, E. R., Ticknor, C., Bethkenhagen, M., Hamel, S., Redmer, R., Kress, J. D., & Collins, L. A. 2015, *Journal of Chemical Physics*, 143, 164513
- Mordasini, C., Alibert, Y., & Klahr, H. Henning, T. 2012, *A & A*, 547, A111
- Nellis, W. J., Holmes, N. C., Mitchell, A. C., Hamilton, D. C., & Nicol, M. 1997, *The Journal of Chemical Physics*, 107, 9096
- Nettelmann, N., Helled, R., Fortney, J., & Redmer, R. 2013, *Planetary and Space Science*, 77, 143
- Nettelmann, N., Wang, K., Fortney, J., Hamel, S., Yellamilli, S., Bethkenhagen, M., & Redmer, R. 2016, *Icarus*
- Ninet, S., Datchi, F., & Saitta, A. M. 2012, *Physical Review Letters*, 108, 165702
- Nosé, S. 1984, *J. Chem. Phys.*, 81, 511
- Peebles, P. 1964, *ApJ*, 140, 328
- Podolak, M., Hubbard, W., & Stevenson, D. 1991, in *Uranus*, ed. J. T. Bergstrahl, E. D. Miner, & M. S. Matthews (University of Arizona, Tucson), 29–61
- Podolak, M., Podolak, J. I., & Marley, M. S. 2000, *Planet. Space Sci.*, 48, 143
- Podolak, M., & Reynolds, R. 1984, *Icarus*, 57, 102
- . 1987, *Icarus*, 70, 31
- Pollack, J., Hubickyj, O., Bodenheimer, P., Lissauer, J., Podolak, M., & Greenzweig, Y. 1996, *Icarus*, 124, 62
- Qi, T., Bethkenhagen, M., & Hamel, S. 2015, *Phys. Rev. E.*, 0, 0
- Radousky, H. B., Mitchell, A. C., & Nellis, W. J. 1990, *The Journal of Chemical Physics*, 93, 8235
- Redmer, R., Mattsson, T. R., Nettelmann, N., & French, M. 2011, *Icarus*, 211, 798
- Sherman, B. L., Wilson, H. F., Weeraratne, D., & Militzer, B. 2012, *Physical Review B*, 86, 224113
- Soubiran, F., & Militzer, B. 2015, *Astrophysical Journal*, 806, 228
- . 2016, *The Astronomical Journal*
- Spanu, L., Donadio, D., Hohl, D., Schwegler, E., & Galli, G. 2011, *Proceedings of the National Academy of Sciences*, 108, 6843
- Stevenson, D. J. 1975, *Physical Review B*, 12, 3999
- Vorberger, J., Tamblyn, I., Militzer, B., & Bonev, S. A. 2007, *Phys. Rev. B*, 75, 024206
- Wang, C., He, X.-T., & Zhang, P. 2013, *Physical Review E*, 88, 033106
- Weinert, M., & Davenport, J. W. 1992, *Phys. Rev. B*, 45, 13709
- Wentzcovitch, R. M., Martins, J. L., & Allen, P. B. 1992, *Phys. Rev. B*, 45, 11372
- Wilson, H., & Militzer, B. 2013, *PRL*, 108, 111101
- Wilson, H. F., Wong, M. L., & Militzer, B. 2013, *Physical Review Letters*, 110, 151102

# A. Equations of state for binary mixtures

The equation of state for the 1:1 water-ammonia mixture has been calculated using an initial fcc lattice, and also by using the orthorhombic lattices which we found from evolutionary crystal structure prediction using the code XtalOpt [189]. The results are shown in Fig. A.1. Some isotherms of the latter EOS are characterized by prominent kinks. This feature indicates the phase transition from the dissociated fluid to the superionic phase.

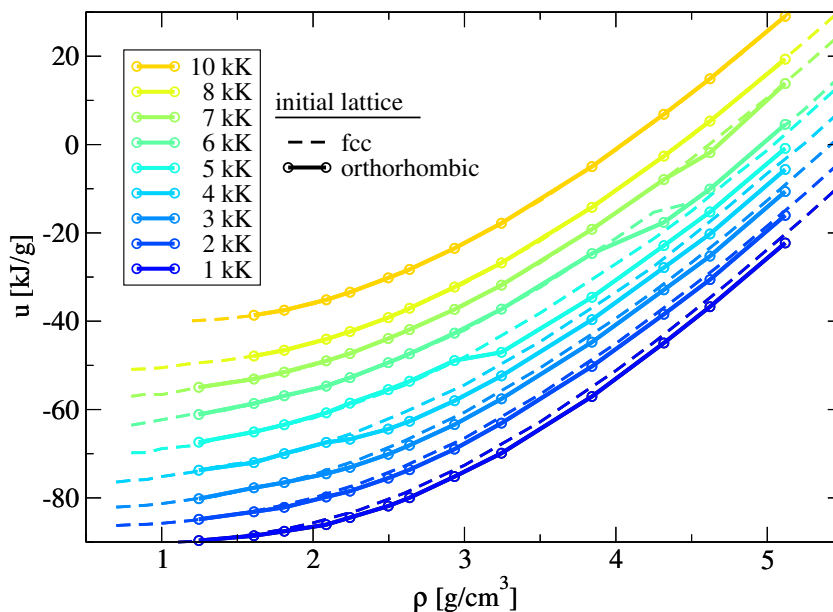
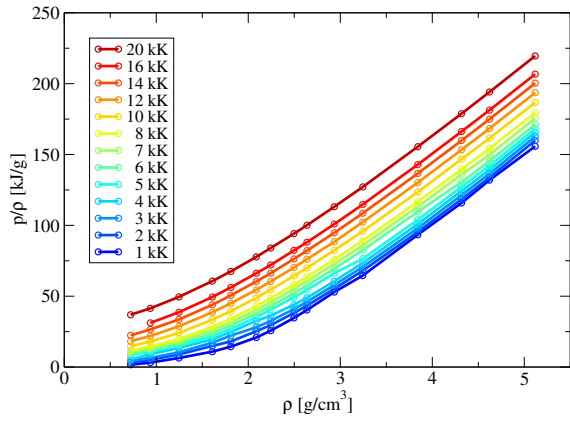


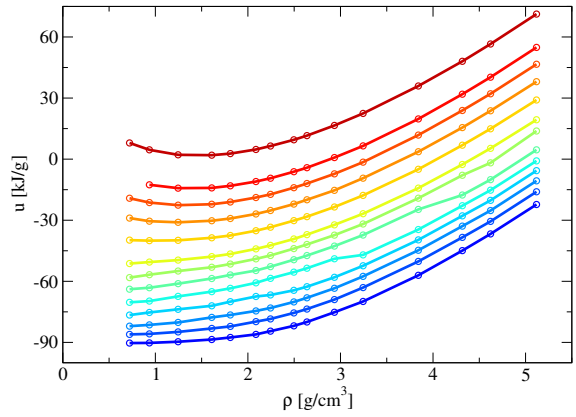
**Fig. A.1.:** Specific internal energy over density of the 1:1 water-ammonia mixture calculated with an initial fcc (dashed lines) and initial orthorhombic (solid lines with circles) lattices. The orthorhombic lattices were generated with evolutionary structure searches employing XtalOpt [189].

For the results from the simulations with an underlying fcc lattice, this behavior is absent except for the 6000 K curve, which has a kink at  $4.25 \text{ g/cm}^3$ . Analyzing the diffusive behavior and pair distribution functions, it is evident that the superionic phase does not form properly for those calculations. Therefore, we conclude that structure searching is a valuable tool to gain insight in unclear phase transitions.

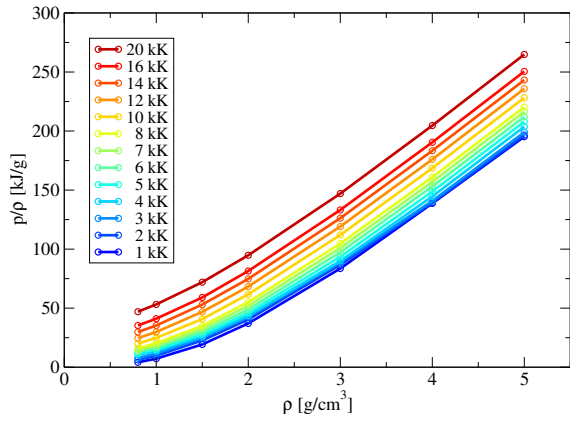
## A. Equations of state for binary mixtures



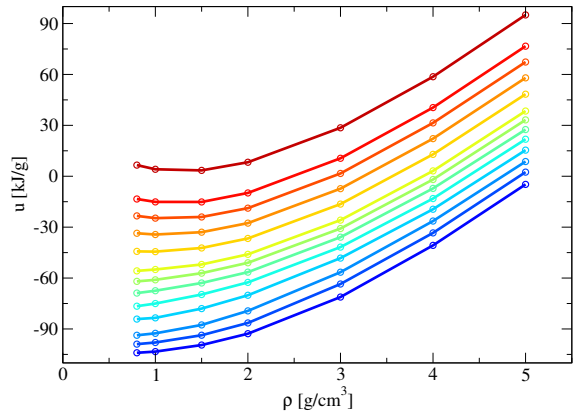
(a) thermal EOS of 1:1 H<sub>2</sub>O-NH<sub>3</sub> mixture



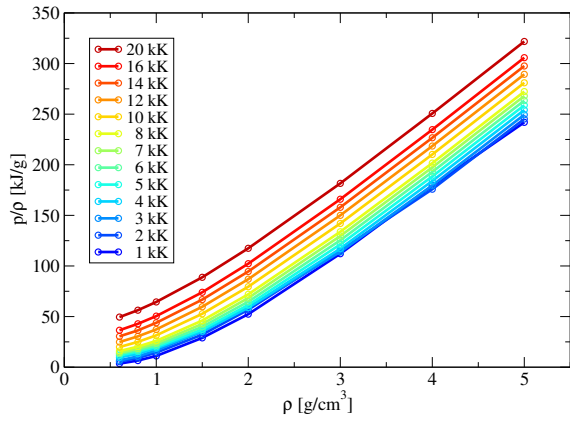
(b) caloric EOS of 1:1 H<sub>2</sub>O-NH<sub>3</sub> mixture



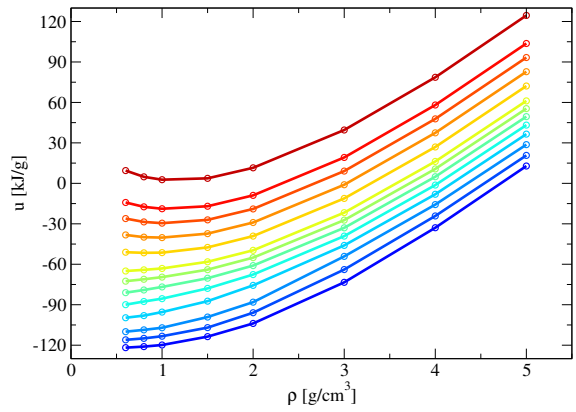
(c) thermal EOS of 1:1 H<sub>2</sub>O-CH<sub>4</sub> mixture



(d) caloric EOS of 1:1 H<sub>2</sub>O-CH<sub>4</sub> mixture



(e) thermal EOS of 1:1 NH<sub>3</sub>-CH<sub>4</sub> mixture



(f) caloric EOS of 1:1 NH<sub>3</sub>-CH<sub>4</sub> mixture

**Fig. A.2.:** Equations of state for the 1:1 water-ammonia mixture from orthorhombic lattices (a)-(b), 1:1 water-methane mixture (c)-(d), 1:1 ammonia-methane mixture started from a bcc lattice (e)-(f).

---

Furthermore, the EOS of the 1:1 water-methane and 1:1 ammonia-methane mixtures have been calculated. However, for neither of the cases we carried out structure searches, since we expect a much more complicated behavior compared to water-ammonia due to the non-polarity of methane and possible demixing effects. Therefore, both EOS were calculated from simulations starting with 54 molecules arranged on a bcc lattice. The thermal and caloric EOS for all 1:1 mixtures of water, ammonia, and methane are shown altogether in Fig. A.2.

For the 1:1 mixtures of water-methane and ammonia-methane shown in Fig. A.2, there are no strong kinks in the caloric EOS as has been found for the 1:1 water-ammonia mixture. However, the curves of the thermal EOS below 4000 K are crossing each other, which might indicate phase transitions. For the water-methane mixture, we find furthermore some indication of possible demixing as well as the formation of strong CO bonds, which needs to be further investigated. Additionally, strong CN bonds have been identified from our simulations of the ammonia-methane mixture. So far, the behavior of this system remains unclear as soon as the demixing region of methane or the superionic region of ammonia is reached.

Overall, the binary systems water-methane and ammonia-methane need to be further investigated in future work. This should be done by starting from better suited lattices, possibly such from structure searching or, in case of water-methane, by starting from methane clathrates [13].



# Bibliography

- [1] K. Altwegg, H. Balsiger, A. Bar-Nun, J.-J. Berthelier, A. Bieler, P. Bochslers, C. Briois, U. Calmonte, M. R. Combi, H. Cottin, J. De Keyser, F. Dhooghe, B. Fiethe, S. A. Fuselier, S. Gasc, T. I. Gombosi, K. C. Hansen, M. Haessig, A. Jäckel, E. Kopp, A. Korth, L. Le Roy, U. Mall, B. Marty, O. Mousis, T. Owen, H. Rème, M. Rubin, T. Sémon, C.-Y. Tzou, J. Hunter Waite, and P. Wurz, *Science Advances* **2**, 5 (2016).
- [2] J. D. Watson, T. A. Baker, S. P. Bell, A. A. F. Gann, M. Levine, and R. M. Losick, *Molecular biology of the gene* (Pearson, 2007).
- [3] K. Lodders, *The Astrophysical Journal* **591**, 1220 (2003).
- [4] International Astronomical Union, Website.
- [5] B. Schmitt, C. De Bergh, and M. Festou, eds., *Solar System Ices*, Vol. I (Springer Science + Business Media B. V., 1998).
- [6] J. J. Fortney and N. Nettelmann, *Space Science Review* **152**, 423 (2010).
- [7] D. A. Schoeller, *The American Journal of Clinical Nutrition* **50**, 1176 (1989).
- [8] M. A. K. Khalil, *Annual Review of Energy and the Environment* **24**, 645 (1999).
- [9] J. W. Erisman, M. A. Sutton, J. Galloway, Z. Klimont, and W. Winiwarter, *Nature Geoscience* **1**, 636 (2008).
- [10] E. Riedel and C. Janiak, *Anorganische Chemie*, 8th ed. (de Gruyter, Berlin, 2011).
- [11] D. Marx, *ChemPhysChem.* **7**, 1848 (2006).
- [12] J. S. Loveday, R. J. Nelmes, M. Guthrie, D. D. Klug, and J. S. Tse, *Physical Review Letters* **87**, 215501 (2001).
- [13] J. S. Loveday and R. J. Nelmes, *Physical Chemistry Chemical Physics* **10**, 913 (2008).
- [14] A. D. Fortes and M. Choukroun, *Space Science Review* **153**, 185 (2010).
- [15] R. J. Hemley, *Annual Review of Physical Chemistry* **51**, 763 (2000).
- [16] V. Schettino and R. Bini, *Physical Chemistry Chemical Physics* **5**, 1951 (2003).

- [17] W. Grochala, R. Hoffmann, J. Feng, and N. W. Ashcroft, *Angewandte Chemie, International Edition* **46**, 3620 (2007).
- [18] P. F. McMillan, *Nature Materials* **4**, 715 (2005).
- [19] P. W. Bridgman, *The Journal of Chemical Physics* **5**, 964 (1937).
- [20] A. Jayaraman, *Reviews of Modern Physics* **55**, 65 (1983).
- [21] N. Dubrovinskaia, L. Dubrovinsky, N. A. Solopova, A. Abakumov, S. Turner, M. Hanfland, E. Bykova, M. Bykov, C. Prescher, V. B. Prakapenka, S. Petitgirard, I. Chuvashova, B. Gasharova, Y.-L. Mathis, P. Ershov, I. Snigireva, and A. Snigirev, *Science Advances* **2**, e1600341 (2016).
- [22] E. Bali, A. Audéat, and H. Keppler, *Nature* **495**, 220 (2013).
- [23] S. Zhang, H. F. Wilson, K. P. Driver, and B. Militzer, *Physical Review B* **87**, 024112 (2013).
- [24] M. S. Somayazulu, L. W. Finger, R. J. Hemley, and H. K. Mao, *Science* **271**, 1400 (1996).
- [25] M. Song, H. Yamawaki, H. Fujihisa, M. Sakashita, and K. Aoki, *Physical Review B* **68**, 014106 (2003).
- [26] D. V. Antsyshkin, A. N. Dunaeva, and O. L. Kuskov, *Geochemistry International* **48**, 633 (2010).
- [27] M. French, *Thermodynamische und Transporteigenschaften von Wasser bei hohen Drücken und hohen Temperaturen*, Ph.D. thesis, University of Rostock (2010).
- [28] J. A. Beattie and C. K. Lawrence, *Journal of the American Chemical Society* **52**, 6 (1930).
- [29] C. S. Cragoe, C. H. Meyers, and C. S. Taylor, *Journal of the American Chemical Society* **42**, 206 (1920).
- [30] R. Overstreet and W. F. Giaque, *Journal of the American Chemical Society* **59**, 254 (1937).
- [31] T. Ichihara and M. Uematsu, *The Journal of Chemical Thermodynamics* **26**, 1129 (1994).
- [32] S. Ninet and F. Datchi, *The Journal of Chemical Physics* **128**, 154508 (2008).
- [33] S. Ninet, F. Datchi, and A. M. Saitta, *Physical Review Letters* **108**, 165702 (2012).
- [34] M. Zander and W. Thomas, *Journal of Chemical and Engineering Data* **24**, 1 (1979).
- [35] R. Bini and G. Pratesi, *Physical Review B* **55**, 14800 (1997).



- 
- [36] E. H. Abramson, *High Pressure Research* **31**, 549 (2011).
- [37] H. E. Maynard-Casely, L. F. Lundegaard, I. Loa, M. I. McMahon, E. Gregoryanz, R. J. Nelmes, and J. S. Loveday, *The Journal of Chemical Physics* **141**, 234313 (2014).
- [38] R. Ludwig, *Angewandte Chemie, International Edition* **40**, 1808 (2001).
- [39] T. Loerting, C. Salzmann, I. Kohl, E. Mayer, and A. Hallbrucker, *Physical Chemistry Chemical Physics* **3**, 5355 (2001).
- [40] C. J. Pickard and R. J. Needs, *The Journal of Chemical Physics* **127**, 244503 (2007).
- [41] J. M. McMahon, *Physical Review B* **84**, 220104 (2011).
- [42] A. Hermann, N. W. Ashcroft, and R. Hoffmann, *Proceedings of the National Academy of Science* **109**, 745 (2012).
- [43] C. J. Pickard, M. Martinez-Canales, and R. J. Needs, *Physical Review Letters* **110**, 245701 (2013).
- [44] T. Bartels-Rausch, V. Bergeron, J. H. E. Cartwright, R. Escibano, J. L. Finney, H. Grothe, P. J. Gutiérrez, J. Haapala, W. F. Kuhs, J. B. C. Pettersson, S. D. Price, C. I. Sainz-Díaz, D. J. Stokes, G. Strazzulla, E. S. Thomson, H. Trinks, and N. Uras-Aytemiz, *Reviews of Modern Physics* **84**, 885 (2012).
- [45] C. G. Salzmann, I. Kohl, T. Loerting, E. Mayer, and A. Hallbrucker, *Canadian Journal of Physics* **81**, 25 (2003).
- [46] C. Cavazzoni, G. L. Chiarotti, S. Scandolo, E. Tosatti, M. Bernasconi, and M. Parrinello, *Science* **283**, 44 (1999).
- [47] M. French, T. R. Mattsson, N. Nettelmann, and R. Redmer, *Physical Review B* **79**, 054107 (2009).
- [48] N. Goldman, E. J. Reed, and L. E. Fried, *The Journal of Chemical Physics* **131**, 204103 (2009).
- [49] A. F. Goncharov, N. Goldman, L. E. Fried, J. C. Crowhurst, I.-F. W. Kuo, C. J. Mundy, and J. M. Zaug, *Physical Review Letters* **94**, 125508 (2005).
- [50] H. F. Wilson, M. L. Wong, and B. Militzer, *Physical Review Letters* **110**, 151102 (2013).
- [51] J. Sun, B. K. Clark, S. Torquato, and R. Car, *Nature Communications* **6**, 8156 (2015).
- [52] M. French, M. P. Desjarlais, and R. Redmer, *Physical Review E* **93**, 022140 (2016).

- [53] J.-A. Hernandez and R. Caracas, *Physical Review Letters* **117**, 135503 (2016).
- [54] M. Guthrie, C. A. Tulk, J. Molaison, and A. M. dos Santos, *Physical Review B* **85**, 184205 (2012).
- [55] C. J. Pickard and R. J. Needs, *Nature Materials* **7**, 775 (2008).
- [56] G. I. G. Griffiths, R. J. Needs, and C. J. Pickard, *Physical Review B* **86**, 144102 (2012).
- [57] G.-R. Qian, H. Niu, C.-H. Hu, A. R. Oganov, Q. Zeng, and H.-Y. Zhou, *Scientific Reports* **6**, 25947 (2016).
- [58] T. Palasyuk, I. Troyan, M. Eremets, V. Drozd, S. Medvedev, P. Zaleski-Ejgierd, E. Magos-Palasyuk, H. B. Wang, S. A. Bonev, D. Dudenko, and P. Naumov, *Nature Communications* **5**, 3460 (2014).
- [59] A. F. Goncharov, N. Holtgrewe, G. Qian, C. Hu, A. R. Oganov, M. Somayazulu, E. Stavrou, C. J. Pickard, A. Berlie, F. Yen, M. Mahmood, S. S. Lobanov, Z. Konôpková, and V. B. Prakapenka, *The Journal of Chemical Physics* **142**, 214308 (2015).
- [60] L. Sun, W. Yi, L. Wang, J. Shu, S. Sinogeikin, Y. Meng, G. Shen, L. Bai, Y. Li, J. Liu, H.-K. Mao, and W. L. Mao, *Chemical Physics Letters* **473**, 72 (2009).
- [61] H. E. Maynard-Casely, C. L. Bull, M. Guthrie, I. Loa, M. I. McMahon, E. Gregoryanz, R. J. Nelmes, and J. S. Loveday, *The Journal of Chemical Physics* **133**, 064504 (2010).
- [62] H. Hirai, K. Konagai, T. Kawamura, Y. Yamamoto, and T. Yagi, *Chemical Physics Letters* **454**, 212 (2008).
- [63] X. Cao, Y. Huang, W. Li, Z. Zheng, X. Jiang, Y. Su, J. Zhao, and C. Liu, *Physical Chemistry Chemical Physics* **18**, 3272 (2016).
- [64] H. Hirai, H. Kadobayashi, N. Hirao, Y. Ohishi, M. Ohtake, Y. Yamamoto, and S. Nakano, *The Journal of Chemical Physics* **142**, 024707 (2015).
- [65] C. W. Wilson, C. L. Bull, G. Stinton, and J. S. Loveday, *The Journal of Chemical Physics* **136**, 094506 (2012).
- [66] G. I. G. Griffiths, A. D. Fortes, C. J. Pickard, and R. J. Needs, *The Journal of Chemical Physics* **136**, 174512 (2012).
- [67] G. I. G. Griffiths, A. J. Misquitta, A. D. Fortes, C. J. Pickard, and R. J. Needs, *The Journal of Chemical Physics* **137**, 064506 (2012).
- [68] R. Chau, S. Hamel, and W. J. Nellis, *Nature Communications* **2**, 203 (2011).

- 
- [69] N. L. Chabot, C. M. Ernst, B. W. Denevi, H. Nair, A. N. Deutsch, D. T. Blewett, S. L. Murchie, G. A. Neumann, E. Mazarico, D. A. Paige, J. K. Harmon, J. W. Head, and S. C. Solomon, *Geology* **42**, 10 (2014).
- [70] Y. N. Kulikov, H. Lammer, H. I. M. Lichtenegger, N. Terada, I. Ribas, C. Kolb, D. Langmayr, R. Lundin, E. F. Guinan, S. Barabash, and H. K. Biernat, *Planetary and Space Science* **54**, 1425 (2006).
- [71] J.-P. Bibring, Y. Langevin, F. Poulet, A. Gendrin, B. Gondet, M. Berthé, P. Drossart, M. Combes, G. Bellucci, V. Moroz, N. Mangold, B. Schmitt, and the OMEGA team, *Nature* **428**, 627 (2004).
- [72] M. Formisano, M. C. Sanctis, G. Magni, C. Federico, and M. T. Capria, *Monthly Notices of the Royal Astronomical Society* **455**, 1892 (2016).
- [73] B. C. Johnson, T. J. Bowling, A. J. Trowbridge, and A. M. Freed, *Geophysical Research Letters* **43**, 070694 (2016).
- [74] F. Sohl, A. Solomonidou, F. W. Wagner, A. Coustenis, H. Hussmann, and D. Schulze-Makuch, *Journal of Geophysical Research: Planets* **119**, 1013 (2014).
- [75] European Space Agency, *JUICE - Exploring the emergence of habitable worlds around gas giants (JUICE assessment study report (Yellow Book))* (2011).
- [76] K. Shin, R. Kumar, K. A. Udachin, S. Alavi, and J. A. Ripmeester, *Proceedings of the National Academy of Sciences* **109**, 14785 (2012).
- [77] L. Noack, D. Höning, A. Rivoldini, C. Heistracher, N. Zimov, B. Journaux, H. Lammer, T. Van Hoolst, and J. H. Bredehöft, *Icarus* **277**, 215 (2016).
- [78] C. Sotin, O. Grasset, and A. Mocquet, *Icarus* **191**, 337 (2007).
- [79] L. Zeng and D. Sasselov, *The Astrophysical Journal* **784**, 96 (2014).
- [80] S. W. Thomas and N. Madhusudhan, *Monthly Notices of the Royal Astronomical Society* **458**, 1330 (2016).
- [81] B. Y. Tian and S. Stanley, *Astrophysical Journal* **768**, 156 (2013).
- [82] D. J. Stevenson, *Annual Review of Earth and Planetary Sciences* **10**, 257 (1982).
- [83] T. Guillot, *Annual Review of Earth and Planetary Sciences* **33**, 493 (2005).
- [84] N. Nettelmann, *Matter under extreme conditions: modelling giant planets*, Ph.D. thesis, University of Rostock (2009).
- [85] N. Nettelmann, A. Becker, B. Holst, and R. Redmer, *The Astrophysical Journal* **750**, 52 (2012).
- [86] T. Gastine, J. Wicht, L. D. V. Duarte, M. Heimpel, and A. Becker, *Geophysical Research Letters* **41**, 5410 (2014).

- [87] W. Lorenzen, B. Holst, and R. Redmer, *Physical Review Letters* **102**, 115701 (2009).
- [88] N. Nettelmann, R. Püstow, and R. Redmer, *Icarus* **225**, 548 (2013).
- [89] R. Püstow, N. Nettelmann, W. Lorenzen, and R. Redmer, *Icarus* **267**, 323 (2016).
- [90] H. Cao, C. T. Russell, U. R. Christensen, M. K. Dougherty, and M. E. Burton, *Earth and Planetary Science Letters* **304**, 22 (2011).
- [91] N. Nettelmann, R. Helled, J. Fortney, and R. Redmer, *Planetary and Space Science* **77**, 143 (2013).
- [92] S. Stanley and J. Bloxham, *Icarus* **184**, 556 (2006).
- [93] K. M. Soderlund, M. H. Heimpel, E. M. King, and J. M. Aurnou, *Icarus* **224**, 97 (2013).
- [94] R. Redmer, T. R. Mattsson, N. Nettelmann, and M. French, *Icarus* **211**, 798 (2011).
- [95] H. Hirai, K. Konagai, T. Kawamura, Y. Yamamoto, and T. Yagi, *Physics of the Earth and Planetary Interiors* **174**, 242 (2009).
- [96] W. DeMarcus, *The Astronomical Journal* **63**, 2 (1958).
- [97] P. Peebles, *The Astrophysical Journal* **140**, 328 (1964).
- [98] W. Wagner and A. Pruß, *Journal of Chemical Reference Data* **31**, 387 (2002).
- [99] U. Setzmann and W. Wagner, *Journal of Physical and Chemical Reference Data* **20**, 1061 (1991).
- [100] L. Haar and J. S. Gallagher, *Journal of Physical and Chemical Reference Data* **7**, 635 (1978).
- [101] B. L. Sherman, H. F. Wilson, D. Weeraratne, and B. Militzer, *Physical Review B* **86**, 224113 (2012).
- [102] D. Saumon, G. Chabrier, and H. M. Van Horn, *The Astrophysical Journal Supplement Series* **99**, 713 (1995).
- [103] A. Becker, W. Lorenzen, J. J. Fortney, N. Nettelmann, M. Schöttler, and R. Redmer, *The Astrophysical Journal Supplement Series* **215**, 2 (2014).
- [104] A. Harlow, G. Wiegand, and E. U. Franck, *Berichte der Bunsen-Gesellschaft* **101**, 1461 (1997).
- [105] R. Span and W. Wagner, *International Journal of Thermophysics* **24**, 111 (2003).

- 
- [106] M. D. Knudson, M. P. Desjarlais, R. W. Lemke, T. R. Mattsson, M. French, N. Nettelmann, and R. Redmer, *Physical Review Letters* **108**, 091102 (2012).
- [107] F. R. Ree, *Equation of state of water (UCRL-52190)*, Los Alamos National Laboratory (1976).
- [108] S. P. Lyon and J. D. Johnson, *SESAME: The Los Alamos National Laboratory equation of state database (LA-UR-92-3407)*, Los Alamos National Laboratory (1995).
- [109] V. M. Shmonov, R. J. Sadus, and E. U. Franck, *The Journal of Physical Chemistry* **97**, 9054 (1993).
- [110] S. Mao, J. Deng, and M. Lü, *Fluid Phase Equilibria* **393**, 26 (2015).
- [111] R. Car and M. Parrinello, *Physical Review Letters* **55**, 2471 (1985).
- [112] M. Born and R. Oppenheimer, *Annalen der Physik* **84**, 457 (1927).
- [113] R. G. Parr, *Annual Review of Physical Chemistry* **34**, 631 (1983).
- [114] A. E. Mattsson, P. A. Schultz, M. P. Desjarlais, T. R. Mattsson, and K. Leung, *Modelling and Simulation in Materials Science and Engineering* **13**, R1 (2005).
- [115] A. D. Becke, *The Journal of Chemical Physics* **140**, 18A301 (2014).
- [116] E. S. Kryachko and E. V. Ludeña, *Physics Report* **544**, 123 (2014).
- [117] R. O. Jones, *Reviews of Modern Physics* **87**, 897 (2015).
- [118] J. Kohanoff, *Electronic structure calculations for solids and molecules: theory and computational methods*, Condensed matter physics, nanoscience and mesoscopic physics (Cambridge University Press, Cambridge, 2006).
- [119] R. M. Martin, *Electronic Structure: Basic Theory and Practical Methods*, Condensed matter physics, nanoscience and mesoscopic physics (Cambridge University Press, Cambridge, 2004).
- [120] D. Frenkel and B. Smit, *Understanding Molecular Simulation: From Algorithms to Applications*, 2nd ed. (Academic Press, Inc., Orlando, 2001).
- [121] D. Marx and J. Hutter, *Ab initio molecular dynamics: basic theory and advanced methods* (Cambridge University Press, Cambridge, 2009).
- [122] D. C. Rapaport, *The Art of Molecular Dynamics Simulation*, 2nd ed. (Cambridge University Press, New York, 2004).
- [123] M. E. Tuckerman, *Statistical Mechanics: Theory and Molecular Simulation*, Oxford graduate texts (Oxford University Press, Oxford, 2010).

- [124] A. Szabo and N. S. Ostlund, *Modern Quantum Chemistry: Introduction to Advanced Electronic Structure Theory*, Dover Books on Chemistry (Dover Publications, 1996).
- [125] L. H. Thomas, *Proceedings of the Cambridge Philosophical Society* **23**, 542 (1927).
- [126] E. Fermi, *Zeitschrift für Physik* **48**, 73 (1928).
- [127] P. A. M. Dirac, *Mathematical Proceedings of the Cambridge Philosophical Society* **26**, 361 (1930).
- [128] P. Hohenberg and W. Kohn, *Physical Review* **136**, B864 (1964).
- [129] N. D. Mermin, *Physical Review* **137**, A1441 (1965).
- [130] W. Kohn and L. J. Sham, *Physical Review* **140**, A1133 (1965).
- [131] S. Yip, “Handbook of materials modeling,” (Springer, 2005) Chap. An Introduction to Orbital Free Density Functional Theory, p. 137.
- [132] V. V. Karasiev, T. Sjöström, and S. B. Trickey, *Computer Physics Communications* **185**, 3240 (2014).
- [133] C. Ticknor, L. A. Collins, and J. D. Kress, *Physical Review E* **92**, 023101 (2015).
- [134] J. P. Perdew, A. Ruzsinszky, J. Tao, V. N. Staroverov, G. E. Scuseria, and G. I. Csonka, *The Journal of Chemical Physics* **123**, 062201 (2005).
- [135] A. Pribram-Jones, S. Pittalis, E. K. U. Gross, and K. Burke, “Frontiers and challenges in warm dense matter,” (Springer, 2014) Chap. Thermal Density Functional Theory in context, p. 25.
- [136] J. P. Perdew, K. Burke, and M. Ernzerhof, *Physical Review Letters* **77**, 3865 (1996).
- [137] P. Haas, F. Tran, and P. Blaha, *Physical Review B* **79**, 085104 (2009).
- [138] R. C. Clay III., M. Holzmann, D. M. Ceperley, and M. A. Morales, *Physical Review B* **93**, 035121 (2016).
- [139] J. Heyd, G. E. Scuseria, and M. Ernzerhof, *The Journal of Chemical Physics* **118**, 8207 (2003).
- [140] M. French, A. Becker, W. Lorenzen, N. Nettelmann, M. Bethkenhagen, J. Wicht, and R. Redmer, *The Astrophysical Journal Supplement Series* **202**, 5 (2012).
- [141] B. Santra, J. Klimeš, A. Tkatchenko, D. Alfè, B. Slater, A. Michaelides, R. Car, and M. Scheffler, *The Journal of Chemical Physics* **139**, 154702 (2013).
- [142] M. J. Gillan, D. Alfè, and A. Michaelides, *The Journal of Chemical Physics* **144**, 130901 (2016).

- 
- [143] M. French and T. R. Mattsson, *Journal of Applied Physics* **116**, 013510 (2014).
- [144] B. J. Alder and T. E. Wainwright, *The Journal of Chemical Physics* **27**, 1208 (1957).
- [145] B. J. Alder and T. E. Wainwright, *The Journal of Chemical Physics* **31**, 459 (1959).
- [146] G. Kresse and J. Hafner, *Physical Review B* **49**, 14251 (1994).
- [147] S. Nosé, *The Journal of Chemical Physics* **81**, 511 (1984).
- [148] H. Hellmann, *Zeitschrift für Physik* **85**, 180 (1933).
- [149] R. P. Feynman, *Physical Review* **56**, 340 (1939).
- [150] M. Weinert and J. W. Davenport, *Physical Review B* **45**, 13709 (1992).
- [151] R. M. Wentzcovitch, J. L. Martins, and P. B. Allen, *Physical Review B* **45**, 11372 (1992).
- [152] C. Niethammer, S. Becker, M. Bernreuther, M. Buchholz, W. Eckhardt, A. Heinicke, S. Werth, H.-J. Bungartz, C. W. Glass, H. Hesse, J. Vrabc, and M. Horsch, *Journal of Chemical Theory and Computation* **10**, 4455 (2014).
- [153] G. Kresse and J. Hafner, *Physical Review B* **47**, 558 (1993).
- [154] G. Kresse and J. Hafner, *Physical Review B* **48**, 13115 (1993).
- [155] G. Kresse and J. Furthmüller, *Physical Review B* **54**, 11169 (1996).
- [156] J. Hafner, *Journal of Computational Chemistry* **29**, 2044 (2008).
- [157] W. Lorenzen, *Phase Transitions in Hydrogen-Helium Mixtures*, Ph.D. thesis, University of Rostock (2012).
- [158] A. Kietzmann, *Quanten-Molekular-dynamik-Simulationen dichter Fluide*, Ph.D. thesis, University of Rostock (2008).
- [159] A. Baldereschi, *Physical Review B* **7**, 5212 (1973).
- [160] H. J. Monkhorst and J. D. Pack, *Physical Review B* **13**, 5188 (1976).
- [161] J. M. Soler, E. Artacho, J. D. Gale, A. García, J. Junquera, P. Ordejón, and D. Sánchez-Portal, *Journal of Physics: Condensed Matter* **14**, 2745 (2002).
- [162] V. Blum, R. Gehrke, F. Hanke, P. Havu, V. Havu, X. Ren, K. Reuter, and M. Scheffler, *Computer Physics Communications* **180**, 2175 (2009).

- [163] P. Giannozzi, S. Baroni, N. Bonini, M. Calandra, R. Car, C. Cavazzoni, D. Ceresoli, G. L. Chiarotti, M. Cococcioni, I. Dabo, A. Dal Corso, S. de Gironcoli, S. Fabris, G. Fratesi, R. Gebauer, U. Gerstmann, C. Gougoussis, A. Kokalj, M. Lazzeri, L. Martin-Samos, N. Marzari, F. Mauri, R. Mazzarello, S. Paolini, A. Pasquarello, L. Paulatto, C. Sbraccia, S. Scandolo, G. Schlauser, A. P. Seitsonen, A. Smogunov, P. Umari, and R. M. Wentzcovitch, *Journal of Physics: Condensed Matter* **21**, 395502 (2009).
- [164] X. Gonze, J.-M. Beuken, R. Caracas, F. Detraux, M. Fuchs, G.-M. Rignanese, L. Sindic, M. Verstraete, G. Zerah, F. Jollet, M. Torrent, A. Roy, M. Mikami, P. Ghosez, J.-Y. Raty, and D. C. Allan, *Computational Materials Science* **25**, 478 (2002).
- [165] M. D. Segall, P. J. D. Lindan, M. J. Probert, P. J. Pickard, C. J. and Hasnip, S. J. Clark, and M. C. Payne, *Journal of Physics: Condensed Matter* **14**, 2717 (2002).
- [166] P. E. Blöchl, *Physical Review B* **50**, 17953 (1994).
- [167] M. P. Allen and D. J. Tildesley, *Computer Simulation of Liquids* (Oxford University Press, 1989).
- [168] O. H. Nielsen and R. M. Martin, *Physical Review Letters* **50**, 697 (1983).
- [169] O. H. Nielsen and R. M. Martin, *Physical Review B* **32**, 3780 (1985).
- [170] P. H. Berens, D. H. J. Mackay, G. M. White, and K. R. Wilson, *The Journal of Chemical Physics* **79**, 2375 (1983).
- [171] M. French and R. Redmer, *Journal of Physics: Condensed Matter* **21**, 375101 (2009).
- [172] M. Bethkenhagen, M. French, and R. Redmer, *The Journal of Chemical Physics* **138**, 234504 (2013).
- [173] T. Qi and E. J. Reed, *Journal of Physical Chemistry A* **116**, 10451 (2012).
- [174] Y. B. Zel'dovich and Y. P. Raizer, *Physics of shock waves and high-temperature hydrodynamic phenomena* (Dover Publications, New York, 2002).
- [175] R. D. Dick, *The Journal of Chemical Physics* **74**, 4053 (1981).
- [176] A. C. Mitchell and W. J. Nellis, *The Journal of Chemical Physics* **76**, 6273 (1982).
- [177] W. J. Nellis, D. C. Hamilton, N. C. Holmes, H. B. Radousky, F. H. Ree, A. C. Mitchell, and M. Nicol, *Science* **240**, 779 (1988).
- [178] H. B. Radousky, A. C. Mitchell, and W. J. Nellis, *The Journal of Chemical Physics* **93**, 8235 (1990).



- 
- [179] W. J. Nellis, N. C. Holmes, A. C. Mitchell, D. C. Hamilton, and M. Nicol, *The Journal of Chemical Physics* **107**, 9096 (1997).
- [180] M. A. Podurets, G. V. Simakov, R. F. Trunin, L. W. Popov, and B. N. Moiseev, *Journal of Experimental and Theoretical Physics* **35**, 375 (1972).
- [181] L. P. Volkov, N. P. Voloshin, R. A. Mangasarov, V. A. Simonenko, and G. Sin'ko, *Journal of Experimental and Theoretical Physics* **31**, 513 (1980).
- [182] P. M. Celliers, G. W. Collins, D. G. Hicks, M. Koenig, E. Henry, A. Benuzzi-Mounaix, D. Batani, D. K. Bradley, L. B. Da Silva, R. J. Wallace, S. J. Moon, J. H. Eggert, K. K. M. Lee, L. R. Benedetti, R. Jeanloz, I. Masclet, N. Dague, B. Marchet, M. Rabec Le Glohec, C. Reverdin, J. Pasley, O. Willi, D. Neely, and C. Danson, *Physics of Plasmas* **11**, L41 (2004).
- [183] K. K. M. Lee, L. R. Benedetti, R. Jeanloz, P. M. Celliers, J. H. Eggert, D. G. Hicks, S. J. Moon, A. Mackinnon, L. B. Da Silva, D. K. Bradley, W. Unites, G. W. Collins, E. Henry, M. Koenig, A. Benuzzi-Mounaix, J. Pasley, and D. Neely, *The Journal of Chemical Physics* **125**, 014701 (2006).
- [184] E. R. Meyer, C. Ticknor, M. Bethkenhagen, S. Hamel, R. Redmer, J. D. Kress, and L. A. Collins, *The Journal of Chemical Physics* **143**, 164513 (2015).
- [185] M. Bethkenhagen, D. Cebulla, R. Redmer, and S. Hamel, *The Journal of Physical Chemistry A* **119**, 10582 (2015).
- [186] Y. Wang and Y. Ma, *The Journal of Chemical Physics* **140**, 040901 (2014).
- [187] E. Zurek and W. Grochala, *Physical Chemistry Chemical Physics* **17**, 2917 (2015).
- [188] R. J. Pickard, C. J. and Needs, *Journal of Physics: Condensed Matter* **23**, 053201 (2011).
- [189] D. C. Lonie and E. Zurek, *Computer Physics Communications* **182**, 372 (2011).
- [190] C. W. Glass, A. R. Oganov, and N. Hansen, *Computer Physics Communications* **175**, 713 (2006).
- [191] Y. Wang, J. Lv, L. Zhu, and Y. Ma, *Computer Physics Communications* **183**, 2063 (2012).
- [192] M. D. Hanwell, D. E. Curtis, D. C. Lonie, T. Vandermeersch, E. Zurek, and G. R. Hutchison, *Journal of Cheminformatics* **4**, 17 (2012).
- [193] D. C. Lonie and E. Zurek, *Computer Physics Communications* **183**, 690 (2012).
- [194] A. Togo, F. Oba, and I. Tanaka, *Physical Review B* **78**, 134106 (2008).
- [195] G. P. Srivastava, *The Physics of Phonons* (Taylor & Francis Group, New York, 1990).

- [196] G. Czycholl, *Theoretische Festkörperphysik*, 3rd ed. (Springer-Verlag Berlin, Heidelberg, 2008).
- [197] D. C. Wallace, *Statistical Physics of Crystals and Liquids - A Guide to Highly Accurate Equations of State* (World Scientific, Singapore, 2002).
- [198] N. Nettelmann, K. Wang, J. J. Fortney, S. Hamel, S. Yellamilli, M. Bethkenhagen, and R. Redmer, *Icarus* **275**, 107 (2016).
- [199] M. Bethkenhagen, E. R. Meyer, S. Hamel, N. Nettelmann, M. French, C. Ticknor, L. A. Collins, J. D. Kress, J. J. Fortney, and R. Redmer, (in preparation).
- [200] J. G. O. Ojwang, R. S. McWilliams, X. Ke, and A. F. Goncharov, *The Journal of Chemical Physics* **137**, 064507 (2012).
- [201] D. F. Li, P. Zhang, and J. Yan, *The Journal of Chemical Physics* **139**, 134505 (2013).
- [202] R. Helled, M. Podolak, and E. Vos, *The Astrophysical Journal Letters* **805**, L11 (2015).
- [203] M. Ross, *Nature* **292**, 435 (1981).
- [204] L. R. Benedetti, J. H. Nguyen, W. A. Caldwell, H. J. Liu, M. Kruger, and R. Jeanloz, *Science* **286**, 100 (1999).
- [205] A. Zerr, G. Serghiou, R. Boehler, and M. Ross, *High Pressure Research* **26**, 23 (2006).
- [206] S. S. Lobanov, P.-N. Chen, X.-J. Chen, C.-S. Zha, K. D. Litasov, H.-K. Mao, and A. F. Goncharov, *Nature Communications* **4**, 2446 (2013).
- [207] F. Ancilotto, G. L. Chiarotti, S. Scandolo, and E. Tosatti, *Science* **275**, 1288 (1997).
- [208] G. Y. Gao, A. R. Oganov, Y. M. Ma, H. Wang, P. F. Li, Y. W. Li, T. Iitaka, and G. T. Zou, *The Journal of Chemical Physics* **133**, 144508 (2010).
- [209] L. Spanu, D. Donadio, D. Hohl, E. Schwegler, and G. Galli, *Proceedings of the National Academy of Sciences* **108**, 6843 (2011).
- [210] J. Chen, X.-Z. Li, Q. Zhang, M. I. J. Probert, C. J. Pickard, R. J. Needs, A. Michaelides, and E. Wang, *Nature Communications* **4**, 2064 (2013).
- [211] S. Habershon and D. E. Manolopoulos, *The Journal of Chemical Physics* **135**, 224111 (2011).
- [212] F. Ercolessi and J. B. Adams, *Europhysics Letters* **26**, 583 (1994).
- [213] S. Izvekov, M. Parrinello, C. J. Burnham, and G. A. Voth, *The Journal of Chemical Physics* **120**, 10896 (2004).

- [214] W. J. Nellis, F. H. Ree, M. van Thiel, and A. C. Mitchell, *The Journal of Chemical Physics* **75**, 3055 (1981).
- [215] R. Helled, J. Anderson, M. Podolak, and G. Schubert, *The Astronomical Journal* **726**, A15 (2011).
- [216] M. Podolak and A. G. W. Cameron, *Icarus* **22**, 123 (1974).
- [217] M. Podolak and R. T. Reynolds, *Icarus* **70**, 31 (1987).
- [218] J. Vorberger, I. Tamblyn, B. Militzer, and S. A. Bonev, *Physical Review B* **75**, 024206 (2007).
- [219] F. Soubiran and B. Militzer, *The Astrophysical Journal* **829**, 14 (2016).
- [220] J. S. Cheng and J. M. Aurnou, *Earth and Planetary Science Letters* **436**, 121 (2016).
- [221] M. P. Desjarlais, *Physical Review E* **88**, 062145 (2013).



# Curriculum vitae

## EDUCATION

- 01/2012 – present: University of Rostock, Germany  
Ph.D. student (Statistical Physics Group)
- 10/2006 – 12/2011: University of Rostock, Germany  
diploma in physics  
diploma thesis (written in German) supervised by Ronald Redmer:  
*Ab initio simulations of ammonia at high pressures* (Statistical Physics Group)

## RESEARCH EXPERIENCE

- 01/2012 – present: University of Rostock, Germany  
research assistant at Statistical Physics Group
- 06/2014 – 08/2014: Lawrence Livermore National Laboratory, CA, USA  
internship at Quantum Simulations Group, supervisor: Sebastien Hamel
- 06/2013 – 08/2013: Lawrence Livermore National Laboratory, CA, USA  
Computational Chemistry and Materials Science Summer Institute  
supervisor: Sebastien Hamel
- 09/2009 – 05/2010: University of Rostock, Germany  
student assistant at Statistical Physics Group, supervisor: Martin French
- 02/2010 – 03/2010: University of Kiel, Germany  
internship at Star and Planet Formation Group, supervisor: Sebastian Wolf and Steve Ertel
- 08/2009 – 10/2009: Leibniz-Institute of Atmospheric Physics e.V., Germany  
student assistant at Optical Soundings Division, supervisor: Gerd Baumgarten

## TEACHING

- summer terms 2012 - 2015  
practical course on classical molecular dynamics simulations of real gases including  
the calculation of transport properties
- winter terms 2013/14 – 2014/15  
seminar on thermodynamics for undergraduate students
- co-advisor of undergraduate students

## LIST OF PUBLICATIONS

1. M. French, A. Becker, W. Lorenzen, N. Nettelmann, M. Bethkenhagen, J. Wicht, R. Redmer  
*Ab Initio Simulations for Material Properties Along the Jupiter Adiabatic*  
The Astrophysical Journal Supplement Series, **202**, 5 (2012).
2. M. Bethkenhagen, M. French, R. Redmer  
*Equation of State and Phase Diagram of Ammonia at High Pressures from Ab Initio Simulations*  
The Journal of Chemical Physics, **138**, 234504 (2013).
3. M. Bethkenhagen, D. Cebulla, R. Redmer, S. Hamel  
*Superionic Phases of the 1:1 Water-Ammonia Mixture*  
Journal of Physical Chemistry A, **119**, 10582 (2015).
4. E. R. Meyer, C. Ticknor, M. Bethkenhagen, S. Hamel, R. Redmer, J. D. Kress, L. A. Collins  
*Bonding and Structure in Dense Multi-Component Molecular Mixtures*  
The Journal of Chemical Physics, **143**, 164513 (2015).
5. N. Nettelmann, K. Wang, J. J. Fortney, S. Hamel, S. Yellamilli, M. Bethkenhagen, R. Redmer  
*Uranus evolution models with simple thermal boundary layers*  
Icarus, **275**, 107 (2016).
6. M. Bethkenhagen, E. R. Meyer, S. Hamel, M. French, N. Nettelmann, C. Ticknor, J. D. Kress, L. A. Collins, J. J. Fortney, R. Redmer  
*The Linear Mixing Approximation for Ices and Application to Uranus*  
in preparation.
7. T. Qi, M. Bethkenhagen, S. Hamel  
*First principles investigation of the demixing of methane at high pressure*  
in preparation.
8. A. Becker, M. Bethkenhagen, C. Kellermann, J. Wicht, R. Redmer  
*Material Properties for the Interiors of Massive Giant Planets and Brown Dwarfs*  
in preparation.

## CONFERENCE TALKS

- *Molecular mixtures at high pressure*  
Joint Workshop on High Pressure, Planetary, and Plasma Physics,  
Bayreuth, Germany (2015)
- *Molecular mixtures at high pressure* (invited)  
International Workshop on Warm Dense Matter,  
Kurashiki, Japan (2015)
- *Superionic water-ammonia mixtures*  
American Geophysical Union Fall Meeting,  
San Francisco, USA (2014)
- *Superionic water-ammonia mixtures*  
Joint Workshop on High Pressure, Planetary, and Plasma Physics,  
Rostock, Germany (2014)
- *Superionic water-ammonia mixtures* (Student Presentation Award)  
Strongly Coupled Coulomb Systems  
Santa Fe, USA (2014)
- *Water-ammonia mixtures at high pressures*  
Northern Astrophysical Colloquium,  
Hamburg, Germany (2014)
- *Water-ammonia mixtures at high pressures*  
4th PlanetMag Meeting, DFG-SPP project 1488 on planetary magnetism,  
Potsdam, Germany (2014)
- *Water-ammonia mixtures at high pressures*  
Joint Workshop on High Pressure, Planetary, and Plasma Physics,  
Berlin, Germany (2013)
- *The high-pressure phase diagram of water: Implications for the magnetic field of Uranus*  
Uranus beyond Voyager 2: From recent advances to future missions,  
Paris, France (2013)





## Danksagung

Zunächst möchte ich mich bei meinem Betreuer Ronald Redmer bedanken, der es mir ermöglicht hat, an diesem spannenden Thema zu arbeiten und immer offen für meine Ideen war. Dabei möchte ich ihm insbesondere für seine Geduld und sein Vertrauen danken. Fachlich danke ich außerdem Bastian Holst, Martin French und Winfried Lorenzen, die mir die Grundlagen sowie Feinheiten der Computersimulationen mit VASP nahe gebracht haben. Besonderer Dank gilt Nadine Nettelmann für astrophysikalische Einsichten, das Aufwerfen wichtiger Fragen und Motivation im Büroalltag in der letzten wichtigen Phase des Schreibens. Zuvor habe ich sehr gern das Admin-Keks-Horst-Büro und damit einhergehend viel Zeit auf Rechner sowie Terminalfenster starrend mit Andreas, Clemens, Manu und Winfried verbracht. Zu einem für mich angenehmen Arbeitsklima haben zudem viele weitere Kollegen und Freunde der (erweiterten) AG Statistische Physik beigetragen. Dabei sind vor allem Cebi und seine beiden Mädels Anja und Livi, Kai, Richard und seine Familie, Volker, Philipp, Waltraud, Wolf und Iro zu nennen.

Weiterhin möchte ich mich aufrichtig für die Unterstützung wichtiger Wegbegleiter bedanken, ohne die eine Anfertigung dieser Arbeit nicht denkbar gewesen wäre. Als erstes möchte ich hier meine Familie nennen, die mich in jeglicher Hinsicht unterstützt hat, allen voran meine großartige Schwester Dana, meine Eltern und Großeltern. Unter ihnen auch mein zu früh verstorbener Opa Hans, dem ich die Freude an Rechnern, meine ersten Programmierkenntnisse und das naturwissenschaftliche Interesse verdanke. Darüber hinaus möchte ich meinen über die Maße verständnisvollen Freunden danken, die mich zuletzt kaum gesehen haben. Dabei bin ich insbesondere Isi, Wiebke und ihren Jungs Mettie und Fips, Katja, Andreas, Tini, Boscheck und Krümel-Alex zu Dank verpflichtet, die mich besonders in der letzten Schreibphase sehr gestützt haben. Außerdem natürlich nicht zu vergessen meine lieben Freunde Anne, Phil, Sascha, Ari, Tim, Lars, Nicole, Keule, Anni, Juli, Justus, Siggie, Hassi, Genner, Carlo, Toppi, Elli, Matze, Jette, Fridde, Nora, Knollo, Richi, Stewen, Christopher, Boot, Steffi, Nhung, Julian, Vincent und Helen. Vielen Dank für all die lustigen Tage, die durchtanzten Nächte, die tollen Unterhaltungen und die schöne gemeinsame Zeit.

An dieser Stelle möchte ich auch noch unbedingt Heidi Redmer, Frau Peters, Helmut, Birgit und all meinen Vierbeinern für Hilfe im richtigen Moment und moralische Unterstützung danken. Abschließend bedanke ich mich auch bei allen fleißigen Korrekturlesern, meinen Kommilitonen und zugleich langjährigen Freunden Lydia und ihrer Familie, Carsten, Ljoscha und seiner Frau Nadja, Thomacz, Benni sowie allen Mitgliedern des Graduiertenkollegs für all die Jahre des Beistandes.

## Acknowledgement

First of all, I wish to thank my advisor at Lawrence Livermore National Laboratory (LLNL), Sebastien Hamel. He has always encouraged me to think beyond the possible and has helped me out with good advice several times. I am also unduly thankful to my collaborators Edmund R. Meyer, Christopher Ticknor, Lee A. Collins and Joel D. Kress at Los Alamos National Laboratory (LANL), who I have always enjoyed discussing with. This work greatly benefitted from the inspiring collaboration with both National Laboratories, enabling me to spend some time in the USA to pursue this project. Most of this time I got to spend in Livermore, where I very much enjoyed the professional, and yet pleasant, working environment. In particular, I am thankful for insightful discussions with Tingting Qi, Eric Schwegler, Marius Millot, Miguel Morales, and Damian Swift. Furthermore, I would like to thank the organizers of the CCMS summer school at LLNL, which contained a series of remarkable talks. This is also where I met my fellow students Lucile Dézerald, Konstantin Weber, and Valerio Rizzi, who I have become very good friends with.

Apart from work, I cannot thank Monica enough, who has opened her home and heart for me and has always been a wonderful friend. Additionally, I would like to thank my friends Mariya, Sarony, Tadashi, Mel, Chad, and my American granny Betty.

## Erklärung

Die Gelegenheit zum vorliegenden Promotionsvorhaben ist mir nicht kommerziell vermittelt worden. Insbesondere habe ich keine Organisation eingeschaltet, die gegen Entgelt Betreuerinnen/Betreuer für die Anfertigung von Dissertationen sucht oder die mir obliegenden Pflichten hinsichtlich der Prüfungsleistungen für mich ganz oder teilweise erledigt.

Ich versichere hiermit an Eides statt, dass ich die vorliegende Arbeit selbstständig angefertigt und ohne fremde Hilfe verfasst habe. Dazu habe ich keine außer den von mir angegebenen Hilfsmitteln und Quellen verwendet und die den benutzten Werken inhaltlich und wörtlich entnommenen Stellen habe ich als solche kenntlich gemacht.

Rostock, den 28.10.2016

Mandy Bethkenhagen